Control of Quadrotor Unmanned Aerial Vehicles with Saturation and Time Delay

by

Ning Cao

A thesis submitted in partial fulfillment of the requirements for the degree of

Doctor of Philosophy

in

Control Systems

Department of Electrical and Computer Engineering
University of Alberta

Abstract

Unmanned Aerial Vehicles (UAVs) are receiving increasing interest from industry and academia due to their wide application in search and rescue, infrastructure inspection, and surveillance. This thesis focuses on research in the area of nonlinear control for rotary wing UAVs. Throughout this thesis, we design the controllers based on the inner-outer loop structure. The outer loop stabilizes translational variables and generates a reference roll and pitch signal which is fed to the inner loop. The benefits of the cascade structure include simplicity of implementation and ease of tuning. Due to physical constraints of actuators, e.g. UAV rotor speed, we consider motion control with input and state constraints. This work considers bounds on thrust, roll, and pitch. Unlike most of the existing work we use a body-frame representation for the dynamics outer loop design. This allows us to specify independent bounds for roll and pitch. The global asymptotic stability of the nested saturation-based outer loop is proven, and the stability of the inner-outer closed-loop is analyzed.

Time delay has practical significance given it can negatively affect the stability of the system. For example, latency in the UAV communication can cause delay. We analyze the robustness of the nested saturation controller with respect to time delay using the emulation approach. A sufficient condition for stability in terms of the upper bound of time delay is derived. Since there is no compensation for delay in the controller design, this method is suitable for smaller delays. We also deal with time delay using prediction method. In this case, we design a predictor-based control for both motion control and visual servoing problems. Parameter uncertainty is also considered. Sufficient conditions for stability are given in terms of linear matrix

inequalities (LMIs) for both problems. The abovementioned control designs and theory is experimentally validated on the Applied Nonlinear Control Lab (ANCL) indoor quadrotor platform.

Preface

- Part of Section 3.3.1 and 3.4 have been published as [N. Cao and A. F. Lynch, "Inner-outer loop control with constraints for rotary-wing UAVs," in 2015 International Conference on Unmanned Aircraft Systems, June 2015, pp. 294–302]. I was responsible for theoretical derivation, simulation and manuscript composition. Dr. Lynch was the supervisory author and was involved with the concept formation and manuscript composition.

- Section 3.3 and 3.5 have been published as [N. Cao and A. F. Lynch, "Inner-Outer loop control for quadrotor UAVs with input and state constraints," IEEE Transactions on Control Systems Technology, vol. 24, no. 5, pp. 1797–1804, September 2016]. I was responsible for theoretical derivation, experimental implementation and manuscript composition. Dr. Lynch was the supervisory author and was involved with the concept formation and manuscript composition.

- Part of Section 4.3 have been published as [N. Cao and A. F. Lynch, "Predictor-based controllers for UAVs with input delay," in 2017 IEEE International Conference on Advanced Intelligent Mechatronics (AIM), July 2017, pp. 803–808]. I was responsible for theoretical derivation, simulation and manuscript composition. Dr. Lynch was the supervisory author and was involved with the concept formation and manuscript composition.

- Section 4.3.1, 4.3.2 and 4.4-4.6 have been submitted as [N. Cao and A. F. Lynch, "Predictor-based control design for UAVs: robust stability analysis and experiments," 28 pages, Submitted to International Journal of Control, Jul. 2018]. I was responsible for theoretical derivation, simulation, experimental implementation and manuscript composition. Dr. Lynch was the supervisory author and was involved with the concept formation and manuscript composition.

- Chapter 5 has been submitted as [N. Cao and A. F. Lynch, "Time-delay robustness analysis of a nested saturation control for UAVs," Submitted to IEEE Transactions on Aerospace and Electronic Systems, Jul. 2018]. I was responsible for theoretical derivation, experimental implementation and manuscript composition. Dr. Lynch was the supervisory author and was involved with the concept formation and manuscript composition.

Table of Contents

List of Tables

List of Figures

Chapter 1

Introduction

1.1 Background

Unmanned Aerial Vehicles (UAVs) are receiving increasing interest from industry and academia. This attention stems from a number of reasons including their use in remote sensing, surveillance, domestic policing, oil, gas and mineral exploration and production, search and rescue, forest fire detection, parcel delivery, and scientific research.

The most common UAVs have a fixed-wing or rotary-wing configuration. Rotary-wing UAVs have unique characteristics which include maneuverability, vertical take-off and landing (VTOL), and hover. This makes them ideal for detailed inspection work or surveying hard-to-reach areas such as pipelines, and power lines. The quadrotor is a popular choice of rotary-wing UAV due to its simplicity of construction and actuation. The first reported quadrotor UAV is HoverBot, invented by Dr. Johann Borenstein in 1992 [1]. The HoverBot is built by tying four helicopters at their tails. Currently, many universities and companies have developed their own quadrotors [2]: X4-flyer (Australian National University [3]), OS4 (EPFL [4]), STARMAC (Standford University [5]), Intel Aero (Intel), ARDrone (Parrot), Spark and Mavic (DJI), etc. The open-source autopilots include Arducopter, Pixhawk [6], Openpilot, Paparazzi, etc [2].

As for scientific research, some research groups have developed their own indoor test bed, such as Real-time indoor Autonomous Vehicle test ENvironment(RAVEN, MIT [7]), General Robotics, Automation, Sensing, and Perception (GRASP) multiple MAV test bed (UPenn [8]), and Flying Machine Arena (FMA, ETH Zurich [9]). Recent research at the University of Alberta's Applied Nonlinear Control Lab (ANCL) has focused on the control of rotary wing UAVs [10–15]. The ANCL indoor UAV platform was developed. Their VTOL maneuverability makes them a good choice for inspection tasks, and the ANCL is currently investigating their application in improving the inspection of transmission lines and other linear struc-
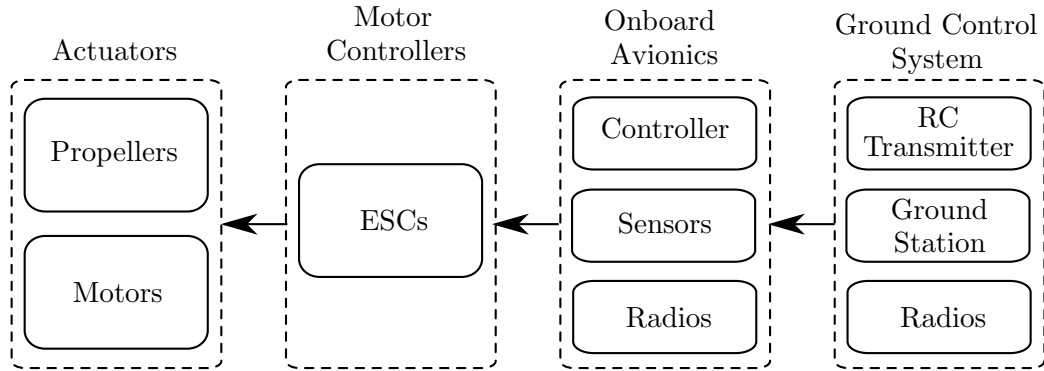
Figure 1.1: Configuration of a typical UAV system.

tures. The aim is to use computer vision to control the relative pose of the vehicle to the line. Having a consistent view of the conductors improves the efficiency and quality of the inspection.

The configuration of a typical quadrotor UAV includes actuators, motor controllers, onboard avionics, sensors, radio transmitters, receivers, and communication systems, as shown in Figure 1.1. The actuators includes the propellers and motors, which are used to generate thrust to control the vehicle. Normally brushless DC (BLDC) are used and are controlled by electronic speed controllers (ESCs) which include an DC/AC inverted circuit. Onboard avionics consists of a processor with input/output (I/O) ports. The outputs connect to the ESCs and telemetry radio. Inputs connect to a radio-control (RC) receiver, and sensors such as a gyroscope, accelerometer, magnetometer, barometer, and global positioning system (GPS). A gyroscope measures changes in orientation or changes in rotational velocity, an accelerometer measures linear accelerations, and a magnetometer determines absolute orientation by measuring magnetic fields. Sensor fusion is performed to improve the accuracy of state estimation. GPS is only valid for outdoor flight because for indoor environment GPS is not available in general. RC transmitters and receivers can be used for manual control. The communication with the ground station, RC transmitters, and other position sensors are implemented by communication modules, e.g. XBee. The tasks include sending and receiving commands, ground monitoring, and receiving external sensor data (e.g. Vicon).

UAVs are usually underactuated. They have four inputs with the capability of motion in 6 degrees of freedom (DOF). This feature makes the motion control of UAVs a challenging task. Work in [16] investigated the input output feedback linearization method. Work in [17, 18] proposed nonlinear controllers based on the backstepping technique. However, practically it is hard to implement the controllers, because derivatives of the thrust are involved in the inputs. The thrust is a function of motor's speed, thus, the dynamics of motor have to be considered as well, which

complicates the problem. Most field tested autopilots use an inner-outer loop or cascade control structure [2, 19]. The idea of separating the control into two (or more) cascaded loops is seen in many applications such as electric motor drives and static synchronous compensators (STATCOMs) for power quality control [20]. The benefits of a two (or more) loop structure include simplicity of implementation, ease of tuning, and satisfaction on input or state constraints. For UAVs, the outer loop stabilizes translational variables, i.e., position and linear velocity, and generates a reference signal fed to the inner loop. Separating the control into simpler translational and rotational designs is important for reliable practical implementation [21–24]. The indoor and outdoor ANCL UAVs have been experimentally tested using an inner-outer loop control structure [13, 14, 25, 26]. Therefore, throughout this thesis, the cascade control structure is applied. It should be noted that the analysis of the entire inner-outer closed-loop stability is performed.

In addition to motion control problem, the problem of visual servoing is considered. Visual servoing involves the use of images from a video camera to achieve a motion control objective. Traditionally, many UAV applications rely on an accurate estimate of the vehicle's position or linear velocity which is fed back to achieve motion control. A UAV's position and velocity is usually estimated by an onboard navigation system which fuses various sensors including accelerometers, gyroscopes, ultrasonic sensors, and GPS [11, 12]. For outdoor applications GPS is commonly used for maintaining a stable position or velocity estimate. However, often GPS is unavailable indoors, or motion control is desired relative to a visual target whose GPS coordinates are uncertain. For example, commercial rotary wing UAV autopilots (e.g. ARDrone 2.0) can hover indoors thanks to a downwards facing video camera which regulates the linear velocity relative to the ground. Given the clear practical benefits of using computer vision in UAV motion control, there is an increasing amount of research on new visual servoing algorithms [27]. For example, model-based visual servo control has been used to land a vehicle whose GPS coordinates are not accurately known [28]. It is important to note that only recently have relatively inexpensive powerful computer vision systems become available to make experimental work on on-board visual servoing for UAVs possible [6].

Input saturation

Due to physical constraints of actuators, e.g. UAV rotor speed, many researchers study motion control with input saturation [29]. In addition, constraints on states should also be considered for practical reasons [30]. For example, it is necessary to constrain attitude to a safe range to avoid undesirable UAV configurations (e.g. an inverted aircraft). Constraints on attitude are also useful for visual servoing applications where an on-board camera is used to provide feedback for motion control

[31, 32]. Here attitude must be limited to ensure the visual target remains in the camera's field of view. The inner-outer loop control structure is useful for limiting attitude since the inner loop references can be saturated [19].

In [33], a nested saturation controller for multiple integrators was proposed. One advantage of this method is that it is induction-based, which allows it to be extended to systems of arbitrary order. However, since there are no control parameters introduced, the closed-loop performance might be degraded especially for bigger initial conditions [34]. With work in [33] as a foundation, many results [35] have been proposed to improve the performance of saturated controllers, e.g. work in [36] added some free parameters so that transient response can be designed. Work in [37] extended this result to the case with bounded external disturbances. Work in [38, 39] generalized the result to controllable linear systems.

The nested saturation controller and its variations have also been applied to UAVs. Lateral and longitudinal controllers for a helicopter was designed in a cascade control structure in [40]. Work in [41] considered mass uncertainty and thrust saturation at the same time. Work in [17] applied the nested saturation control to an approximately linearized model to account for thrust and torque limits. Work in [42] considers a visual servoing application and incorporates orientation limits using nested saturation and the angle between the z-axes of the navigation and body frames. A cascade framework using the rotation matrix is in [24] which includes bounds on thrust.

Model predictive control (MPC) or receding horizon control (RHC) is another useful method for constrained control [43] and has been applied on UAVs [44]. MPC solves an online finite horizon open-loop optimal control problem with constraints involving states and inputs. However, online computational burden of MPC might degrade its performance. In general, global stability is hard to achieve with MPC.

Time delay

The ANCL UAV indoor platform includes a Vicon motion capture system which provides the vehicle's position, linear velocity, and attitude. In many cases the position and linear velocity are sent to the vehicle via a wireless link. In some cases the yaw is also sent to avoid problems with magnetic interference introducing errors in the on-board estimation of yaw. The wireless transmission introduces a time delay to the Vicon data when it received on-board. For UAVs with GPS as the sensor, a delay is introduced for the same reason. Futhermore, for visual servoing applications, the image processing time also causes a delay. Therefore, it is necessary to consider the time delay while designing a controller. Since the time delay from the Vicon system only influences the outer loop, we categorize it as input or measurement delay.

Time-delay systems are infinite-dimensional, thus instead of Lyapunov functions, Lyapunov-Krasovskii Functionals (LKF) are used for stability analysis. The LKF depends on past values of the state variable which can complicate analysis. This difficulty led to the Razumikhin stability theorem, which does not necessarily require the derivative of a Lyapunov function to be negative for all time [45, 46]. In [47] it is pointed out that results using LKF are generally less conservative. Another method for stability analysis uses the frequency domain and the location of the system's characteristic roots [47, 48]. This approach can only be applied to linear systems.

There are two main categories for the control of systems with input delays [49, 50]. The first one is called model reduction or prediction, which compensates delays by augmenting the system with a new state. Predictor-based control methods for input delays are commonly used, especially for problems with large delay. Examples of this approach are the well-known Smith Predictor, Finite Spectrum Assignment, and the reduction approach [51, 52]. More recently, work in [49] developed a backstepping design procedure using a partial differential equation (PDE) framework which provided a stability proof based on LKF for linear systems with constant delays. Using an adaptive control method, this result was extended in [53] to the unknown delay case and the unknown constant input disturbances case [54]. Work in [55] dealt with unknown time-varying disturbances. Work in [56] developed a predictor-based control for multi-input nonlinear systems with distinct input delays in each input channel. By introducing a new method for constructing LKFs, work in [57] considered linear systems with distributed input delay. In [58] a predictor-based control using chaotic synchronization is designed. Here, an extra correction term in the predictor dynamics is introduced to improve robustness. This method has been applied for remote control of a wheeled mobile robot in [59].

The second way in dealing with input delay is called the emulation approach. This method designs a stabilizing controller for a nominal system without delay, and analyzes the effect of delays on the closed-loop stability. This method is generally suitable for small delays and is easy to implement because no extra design is needed. Constraints on the size of the delay are given to ensure stability. For linear systems, we can design linear controllers and analyze their robustness to the time delay based on LKF, Razumikhin theorem or frequency domain method. Analysis of linear time delay systems can be found in [48]. For some cases, nonlinear controllers are investigated for linear systems, e.g. the saturation control. Work in [60] solved the problem of the global uniform asymptotic stabilization by bounded feedback of a chain of integrators with a delay in the input. A review for nonlinear time delay systems using emulation approach can be found in [50].

The background described above motivates this thesis. The research focuses on model-based motion and visual servoing control for quadrotor UAVs with constraints

and time delay disturbance. A nested saturation controller is proposed such that the thrust, roll and pitch are constrained. Both prediction and emulation methods are considered for the control of UAVs with time delay. Outline of this thesis is summarized in the following section.

1.2　Thesis outline

The outline of this thesis is given in this section. Thesis contributions are summarized in Section 1.3.

A model of the UAV considered in this thesis is given in Chapter 2. We start with the translational dynamics in both navigation and body frames, and rotational dynamics in Section 2.1. We introduce the image kinematics for visual servoing including the virtual camera model. In Section 2.2 we present the ANCL quadrotor platform which is the experimental test bed used in the following chapters.

Chapter 3 focuses on the position control of quadrotor UAVs with state and input constraints using an inner-outer loop control structure. We review Teel's nested saturation method [33] for a chain of integrators in Section 3.2. In Section 3.3 we propose a nested saturation control for the translational dynamics of a UAV in body frame. Using body frame allows for independent bounds on roll and pitch.Based on this controller, the outer loop generates a saturated thrust, and the reference roll and pitch angles, while the inner loop is designed to follow these reference angles using a traditional PID controller. A commonly-used PID structure based on Euler angles is relatively easy to implement and tune. The proof of global asymptotic stability of the outer loop is provided. The closed-loop stability is also analyzed in this section. Simulation and experimental results to validate the controller are in Section 3.4 and 3.5.

Chapter 4 studies the input-delay control for UAVs. We start the chapter with an introduction of time delay systems which includes the functional-differential-equation description and definitions of stability. We overview three methods for stability analysis: frequency domain, LKF-based, and Razumikhin theorem-based. An overview of the control problem of time delay systems is given in Section 4.2. In Section 4.3 we propose synchronization-based predictors for a class of systems based on the work in [58, 59]. We consider the robustness to uncertainty in model parameter and unknown time delay. To improve its robustness we modify the method in [58, 59] by adding an extra term in the predictor dynamics. Assuming the unknown parameter and time delay are bounded with known bounds, global asymptotic stability is proven. In Section 4.4 the results are applied to two input delayed control problems for UAVs: motion control and visual servoing. Section 4.5 and 4.6 provide simulation and experimental results.

In the presence of time delay the nested saturation control cannot be extended using the predictor designed in Chapter 4. This is because the stability analysis of nested saturation controllers is based on induction. A different Lyapunov function is designed for each step to guarantee its convergence to an invariant set, thus there is no unified Lyapunov function. Therefore, in Chapter 5, we analyze the robustness of the nested saturation controller proposed in Chapter 3 to time delay using the emulation approach. This work is inspired by [60] which analyzed the robustness of the nested saturation controller for chains of integrators. This method is suitable for small delays and is easy to implement because no extra design is needed. The controller design is described in Section 5.2. Compared to Chapter 3, the analysis has been simplified. Instead of considering the dynamics in the body frame, a new frame is proposed. In addition, instead of treating each component of a saturated vector separately as in Chapter 3, here we analyze the stability based on a vector norm. This simplifies the proof which is given in Section 5.3. Based on the analysis, sufficient conditions of stability on time delay and control parameters are given. We provide simulation and experimental results in Section 5.4.

In Chapter 6, we conclude the work done in this thesis and discuss possible future research directions.

1.3   Contribution

The contributions of this thesis are summarized as follows:

- Motion control with saturation [15, 61]. A saturated controller for the translational dynamics in body frame is proposed. This is a vector form of Teel's nested saturation method for a chain of integrators in [33]. The difficulty is duo to the fact that variables in the dynamics are 3-dimensional vectors and are coupled. The contribution of this work is the stability analysis of nested saturation control for systems of this form.

- Predictor-based controller with the presence of time delay [62, 63]. We improve the robustness of the synchronization-based prediction controller originally proposed in [58] and [59] by adding an extra term in the predictor dynamics. Uncertainties considered include unknown model parameters and time delay mismatch. Sufficient conditions for stability are given in terms of linear matrix inequalities (LMIs).

- Robustness analysis of the nested saturation control with respect to time delay [64]. Using a new reference frame, we modify the nested saturation control proposed in [15, 61]. Also, for simplicity, the norm of a saturation vector

is used in the stability analysis. The analysis yields sufficient conditions for stability in terms of time delay and control parameters.

- Experimental validation of controllers [15, 63, 64]. The controllers proposed in [15, 63, 64] are implemented on the ANCL indoor quadrotor platform to validate the theoretical results. The implementation is based on open-source Pixhawk hardware and PX4 firmware and the code is available at Gitlab[1].

---

[1]http://gitlab.nonlin.local/px4.git

Chapter 2

Model and Platform

In this chapter, we will introduce the quadrotor model that will be used in this thesis. We start with the translational dynamics in different frames, and rotational dynamics. We also introduce image kinematics for visual servoing problems. In the end, we present the indoor ANCL quadrotor platform. Controllers designed in the following several chapters will be experimentally validated on this platform.

2.1   Modelling

In this section, the rigid body dynamics of a quadrotor UAV is presented. Similar material can be found in existing literature, e.g. [65–68]. Unlike traditional helicopters which rely on complex linkage mechanisms to implement a variable pitch rotor, the quadrotor uses fixed pitch propellers with direct drive variable speed brushless DC motors to control the external force and torque on the vehicle. As shown in Figure 2.1, we label the four rotors 1 to 4 and denote their speeds $\Omega_i, i = 1, 2, 3, 4$ which can be considered the system's physical inputs. The direction of rotation for Rotors 1 and 2 is opposite to Rotors 3 and 4. This ensures no reaction torque when rotor speeds are equal.

The modelling is based on two reference frames. A navigation frame is stationary with respect to the earth and denoted $\mathcal{N} = \{n_1, n_2, n_3\}$, where n_1, n_2, n_3 are basis vectors with n_3 pointing down. The body fixed frame is fixed to UAV's centre of mass (CoM) and denoted $\mathcal{B} = \{b_1, b_2, b_3\}$, where b_1, b_2, b_3 are basis vectors. The two frames of reference are shown in Figure 2.1. We chose b_3 to point down and b_1 to points in direction midway between the arms of Rotor 1 and 3. We remark that other choices for b_1 are common and define the so-called "x" and "+" configurations [32]. The rotation matrix $R \in \mathbb{R}^{3 \times 3}$ transforms vectors between $\mathcal{N}$ and $\mathcal{B}$. We
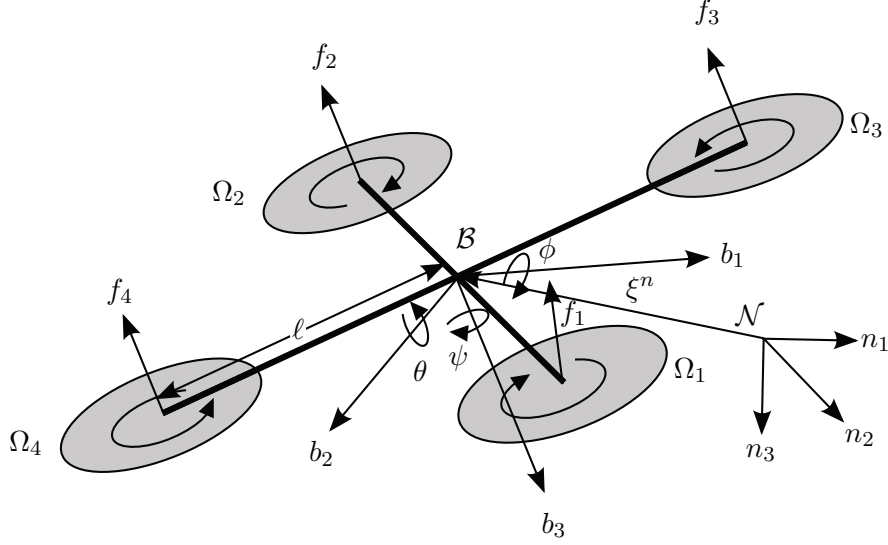
Figure 2.1: Frame definition of a quadrotor UAV.

parametrize R using the "ZYX" Euler angles $\eta = [\phi, \theta, \psi]^T$ as

$$
R(\eta) = \begin{bmatrix}
c_\psi c_\theta & -s_\psi c_\phi + c_\psi s_\theta s_\phi & s_\phi s_\psi + c_\phi s_\theta c_\psi \\
s_\psi c_\theta & c_\psi c_\phi + s_\psi s_\theta s_\phi & -s_\phi c_\psi + c_\phi s_\theta s_\psi \\
-s_\theta & c_\theta s_\phi & c_\theta c_\phi
\end{bmatrix}
$$

where ϕ is roll, θ is pitch, and ψ is yaw, $s_\phi = \sin\phi$, and $c_\phi = \cos\phi$. As shown in Figure 2.2, the coordinates of a point P in the body fixed frame P^b can be related to its coordinates in the navigation frame P^n by

$$
P^b = R^T(P^n - p^n) \tag{2.1}
$$

where p^n is the translation from the origin of $\mathcal{N}$ to the origin of $\mathcal{B}$ expressed in $\mathcal{N}$.

2.1.1   Quadrotor translational dynamics

From Newton's law we obtain the translational dynamics using the position of the UAV in $\mathcal{N}$

$$
\dot{p}^n = v^n \tag{2.2a}
$$

$$
m\dot{v}^n = mgn_3 + RF^b \tag{2.2b}
$$

where m is mass, $p^n \in \mathbb{R}^3$, $v^n \in \mathbb{R}^3$ is velocity expressed in $\mathcal{N}$, and the term mgn_3 is the gravitational force. $F^b \in \mathbb{R}^3$ is the external force acting on the vehicle expressed in $\mathcal{B}$.

For each rotor, the steady-state thrust generated by a hovering rotor in free air
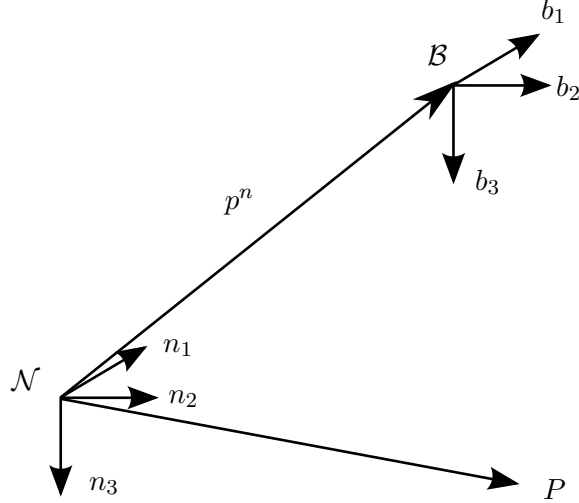
Figure 2.2: Relation between the navigation frame and the body fixed frame.

can be modelled as

$$f_i = C_f \rho A_{r_i} r_i^2 \Omega_i^2 := c_{f_i} \Omega_i^2$$

where C_f is the thrust coefficient related to rotor geometry and profile, e.g., angle of attack. ρ is the density of air. $A_{r_i} = \pi r_i^2$ is the area of rotor disk, r_i is the radius.

Rotors of a quadrotor are not rigid and aerodynamic forces acting on the rotors can cause the rotor to flex. This mechanism will protect motors mounting or the airframe while causing the blade-flapping effect. It is concluded that the flapping dynamics converge to steady state after one cycle, thus only the steady state is studied. The longitudinal and lateral flapping angles can be modelled as [69]

$$u_{1_s i} = \frac{1}{1 - \frac{\mu_i^2}{2}} \mu_i (4\vartheta_t - 2\lambda_i^2)$$

$$v_{1_s i} = \frac{1}{1 + \frac{\mu_i^2}{2}} \left(\frac{C_f}{\sigma} \frac{8}{9} \frac{\mu_i \gamma}{a} + \frac{C_f}{2\mu_i} \right)$$

where $\mu_i = \frac{\|v_{1,2}^b\|}{\Omega_i r_i}$ is the rotor's ratio, $v^b = R^T v^n$. ϑ_t is blade tip angle. $\lambda_i = \sqrt{\frac{C_f}{2}}$ is the non-dimensionalised near-hover inflow of the ith rotor. σ is the solidity of the rotor, i.e., the ratio of the surface area of the blades and the rotor disc area. a is the airfoil polar lift slope. γ is the Lock Number [70]. Then, the flapping angles in the body frame can be calculated as [69]

$$a_{1_s i} = c_{\psi_i} u_{1_s i} - s_{\psi_i} v_{1_s i}$$

$$b_{1_s i} = s_{\psi_i} u_{1_s i} + c_{\psi_i} v_{1_s i}$$

where $\psi_i = \arctan(\frac{v_2^b}{v_1^b})$ is the azimuthal direction of motion.

Besides, drag force on the body is also considered in some references [67, 71]. The drag force is proportional to the body-frame velocity v^b, i.e.,

$$F^b_{drag} = - \begin{bmatrix} \kappa v^b_1 \\ \kappa v^b_2 \\ 0 \end{bmatrix}$$

where κ is the drag coefficient which can be modelled as $\kappa = \lambda_i \sum_{i=1}^4 \Omega_i$. κ can be treated as constant because in nominal flight conditions for a quadrotor, the sum of rotors' angular speeds can be seen as a constant [71].

The total external force will be

$$F^b = \sum_{i=1}^4 f_i \begin{bmatrix} -\sin a_{1_s i} \\ \cos a_{1_s i} \sin b_{1_s i} \\ -\cos a_{1_s i} \cos b_{1_s i} \end{bmatrix} - \begin{bmatrix} \kappa v^b_1 \\ \kappa v^b_2 \\ 0 \end{bmatrix}$$

Throughout this thesis, we simplify the external force by neglecting the blade flapping and drag force. Thus, the external force F^b has the form

$$F^b = \begin{bmatrix} 0 \\ 0 \\ -T \end{bmatrix} \tag{2.3}$$

where $T = \Sigma_{i=1}^4 f_i$. In the following chapters, we will treat T as the control input.

The dynamics can also be expressed in $\mathcal{B}$. We assume the point P is at the origin of $\mathcal{N}$ in Figure 2.2. Then, $P^n = [0, 0, 0]^T$ and $p^b = -P^b$.

Based on (2.1), we have $p^b = -P^b = -R^T(-p^n) = R^T p^n$, where p^b denotes position expressed in $\mathcal{B}$. In order to obtain the translational dynamics in terms of p^b and v^b, we require the rotational kinematics. Since R is orthogonal, i.e., $RR^T = R^T R = I$, by taking the derivatives on both sides, we get $\dot{R}R^T = -R\dot{R}^T = -(\dot{R}R^T)^T$, thus $\dot{R}R^T$ is a skew-symmetric matrix and is parameterized using $\mathrm{sk}(\omega^n)$ [72], where $\omega^n \in \mathbb{R}^3$ is the UAV's angular velocity expressed in $\mathcal{N}$ and the operator $\mathrm{sk}(\cdot)$ is defined as

$$\mathrm{sk}\left(\begin{bmatrix} a_1 \\ a_2 \\ a_3 \end{bmatrix} \right) = \begin{bmatrix} 0 & -a_3 & a_2 \\ a_3 & 0 & -a_1 \\ -a_2 & a_1 & 0 \end{bmatrix}$$

Therefore, we have

$$\dot{R} = \mathrm{sk}(\omega^n)R = R\,\mathrm{sk}(\omega^b) \tag{2.4}$$

where $\omega^b = R^T \omega^n$ is the angular velocity expressed in $\mathcal{B}$.

Then, taking the derivatives of p^b and using (2.2), (2.3) and (2.4) leads to

$$\dot{p}^b = -\mathrm{sk}(\omega^b)p^b + v^b \tag{2.5a}$$

$$\dot{v}^b = -\mathrm{sk}(\omega^b)v^b + gR^T n_3 - \frac{T}{m}b_3 \tag{2.5b}$$

where $v^b = R^T v^n$ is velocity in $\mathcal{B}$.

Remark 2.1. Robustness analysis to unmodelled dynamics and external disturbances, e.g. wind gust disturbance, is out of scope of this thesis. However, in the following chapters, we will add these disturbances in the simulation to show the effectiveness of the proposed controllers. The detailed description of the simulation can be found in Chapter 3. The robustness of proposed controllers in this thesis is also shown in experiments. We remark that study on the robustness of UAV controllers to disturbances and uncertainties has attracted massive attention in academia [73]. Work in [74] considers external forces and torque disturbances and the unknown position of CoM. Work in [75] investigates an approximate adaptive controller for model uncertainties, e.g. payloads, and disturbances.

2.1.2 Quadrotor rotational dynamics

The rotational dynamics are given by Euler's equation [72]:

$$J\dot{\omega}^b = -\omega^b \times J\omega^b + \tau^b \tag{2.6}$$

where $J \in \mathbb{R}^{3\times3}$ denotes the inertia tensor of the UAV and $\tau^b \in \mathbb{R}^3$ is the applied torque in the body frame, which can be modelled as follows. The first term comes from aerodynamic forces, i.e., the thrust imbalance and drag force acting on the rotors. The drag is acting on the blades not on the hub, thus it results in drag torque, the magnitude of which can be modelled as

$$\tau_i = C_\tau \rho A_{r_i} r_i^3 \Omega_i^2 := c_{\tau_i} \Omega_i^2$$

The sign depends on its direction of rotation. It is positive for rotor rotating counterclockwise. Here we assume the thrust from each rotor is in b_3 direction. Therefore, the torque is modelled as

$$\tau_f^b = \begin{bmatrix} (f_2 + f_3 - f_1 - f_4)\frac{l}{\sqrt{2}} \\ (f_1 + f_3 - f_2 - f_4)\frac{l}{\sqrt{2}} \\ \sum_{i=1}^4 \delta_i \tau_i \end{bmatrix}$$

where l is the distance from the motor to the CoM of the vehicle. δ_i denotes the sign of the drag torque for the ith rotor. Besides, the rotating rotor can be seen as

13

a gyroscope, thus changes in the attitude will cause the gyroscopic torque, which can be given as

$$\tau_g^b = \sum_{i=1}^{4} \delta_i \begin{bmatrix} 0 & -\dot{\psi} & \dot{\theta} \\ \dot{\psi} & 0 & -\dot{\phi} \\ -\dot{\theta} & \dot{\phi} & 0 \end{bmatrix} \times \begin{bmatrix} 0 \\ 0 \\ J_r \Omega_i \end{bmatrix} = \sum_{i=1}^{4} \delta_i \begin{bmatrix} J_r \Omega_i \dot{\theta} \\ -J_r \Omega_i \dot{\phi} \\ 0 \end{bmatrix}$$

where J_r is the rotor inertia.

In addition, there is a reaction torque due to the rate change of the rotors' speeds. This torque is only in b_3 direction, i.e.,

$$\tau_r^b = \sum_{i=1}^{4} \delta_i J_r \dot{\Omega}_i b_3$$

Therefore, the total torque can be modelled as

$$\tau^b = \tau_f^b + \tau_g^b + \tau_r^b$$

However, in most references [66, 76, 77], the model of τ^b used for control are approximated by taking the main components, i.e., $\tau^b = \tau_f^b$. Then, the torque τ^b is can be expressed in terms of rotor thrust as

$$\tau^b = \begin{bmatrix} (f_2 + f_3 - f_1 - f_4)l/\sqrt{2} \\ (f_1 + f_3 - f_2 - f_4)l/\sqrt{2} \\ \alpha_3 f_3 + \alpha_4 f_4 - \alpha_1 f_1 - \alpha_2 f_2 \end{bmatrix} \tag{2.7}$$

where $\alpha_i = \frac{c_{\tau_i}}{c_{f_i}}$. We remark that there is a known one-to-one relation between (F^b, τ^b) and rotor speed $\Omega_i, i = 1, 2, 3, 4$. Hence, for simplicity, in the rest of this thesis, T and τ^b are taken as control inputs.

The moment of inertia J of a rigid object can be identified using the trifilar pendulum method. To develop this method, the rigid body is suspended from a platform using three flexible wires and the period of torsional oscillation around the vertical axis is measured. We built a thin cardboard as a platform with 6 marks attached for Vicon detection.

We run 5 experiments with the following setup:

- cardboard

- cardboard + stand

- cardboard + stand + quadrotor in x-axis

- cardboard + stand + quadrotor in y-axis
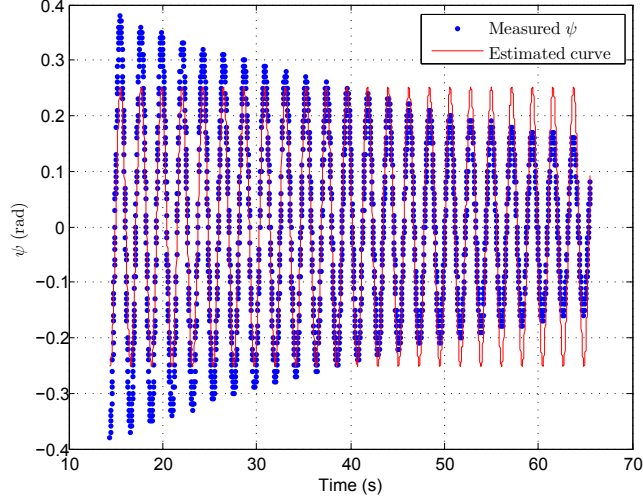
Figure 2.3: Measured yaw and its estimate.

- cardboard + quadrotor in z-axis

For each experiment, we

- Record the yaw angle of the object with the help of Vicon motion capture system;

- Use function *createFit* in Matlab to find the best fitting curve. One example is given in Figure 2.3. Note that only the oscillation frequency is needed for the measurement. Therefore, the mismatch between magnitudes is acceptable.

- Run the experiments with the same setup 10 times and calculate the average of oscillation period.

The moments of inertia of the quadrotor are

$$J_{xx} = (2.99 \pm 0.09) \times 10^{-2} \ \text{kg} \cdot \text{m}^2$$
$$J_{yy} = (2.76 \pm 0.09) \times 10^{-2} \ \text{kg} \cdot \text{m}^2$$
$$J_{zz} = (4.81 \pm 0.06) \times 10^{-2} \ \text{kg} \cdot \text{m}^2$$

In addition, (2.4) can be expressed alternatively using Euler angles. From the previous subsection we recall $\text{sk}(\omega^b) = -\dot{R}^T R$, where R and $\dot{R}$ can be expressed using Euler angles η and their derivatives $\dot{\eta}$. Thus, solving for $\dot{\eta}$ we obtain

$$\dot{\eta} = W\omega^b \tag{2.8}$$

15

where

$$W = \begin{bmatrix} 1 & s_\phi t_\theta & c_\phi t_\theta \\ 0 & c_\phi & -s_\phi \\ 0 & s_\phi/c_\theta & c_\phi/c_\theta \end{bmatrix}$$

where $t_\theta = \tan\theta$.

The rotation matrix using Euler angles is not a global representation. The singularities occur when $\theta = (2k+1)\frac{\pi}{2}, k \in \mathbb{Z}$ [78]. For example, when $\theta = \frac{\pi}{2}$,

$$R(\phi, \frac{\pi}{2}, \psi) = \begin{bmatrix} 0 & s_{\phi-\psi} & c_{\phi-\psi} \\ 0 & c_{\phi-\psi} & -s_{\phi-\psi} \\ 1 & 0 & 0 \end{bmatrix}$$

This implies for $\theta = \frac{\pi}{2}$, the rotation matrix is the same as long as $\phi - \psi$ is constant. This can be seen as the mathematical explanation of the well-known gimbal lock phenomenon. Moreover, the determinant of W in (2.8) is $\frac{1}{c_\theta}$. This implies when $\theta = \frac{\pi}{2}$, infinite angle rates are needed to generate a finite angular velocity [78].

The singularities can be avoided with quaternions. The unit quaternion contains a scalar q_0 and 3 dimensional vector $q = [q_1, q_2, q_3]^T$ satisfying

$$q_0 + \|q\|^2 = 1$$

Accordingly, the rotation matrix using quaternions is given as

$$R = \begin{bmatrix} 1 - 2q_2^2 - 2q_3^2 & 2q_1q_2 - 2q_0q_3 & 2q_1q_3 + 2q_0q_2 \\ 2q_1q_2 + 2q_0q_3 & 1 - 2q_1^2 - 2q_3^2 & 2q_2q_3 - 2q_0q_1 \\ 2q_1q_3 - 2q_0q_2 & 2q_2q_3 + 2q_0q_1 & 1 - 2q_1^2 - 2q_2^2 \end{bmatrix}$$

The quaternion evolves as

$$\begin{bmatrix} \dot{q}_0 \\ \dot{q}_1 \\ \dot{q}_2 \\ \dot{q}_3 \end{bmatrix} = \frac{1}{2} \begin{bmatrix} q_0 & -q_1 & -q_2 & -q_3 \\ q_1 & q_0 & -q_3 & q_2 \\ q_2 & q_3 & q_0 & -q_1 \\ q_3 & -q_2 & q_1 & q_0 \end{bmatrix} \begin{bmatrix} 0 \\ \omega_1^b \\ \omega_2^b \\ \omega_3^b \end{bmatrix}$$

Controllers based on quaternions can be found in [79, 80]. However, despite of its disadvantage, the roll-pitch-yaw representation is still very popular. In some cases when singularities won't happen, it is not necessary to introduce one redundant variable. For this reason, in this thesis, we will use the Euler angle representation.

2.1.3 Image kinematics

This thesis will consider visual servoing problems of UAVs, i.e., control the motion of UAVs based on the computer vision data. There are two main visual servoing methods: position-based and image-based visual servoing (PBVS and IBVS) [27]. In PBVS, the relative 3D pose between camera and target is used as a control input. This pose is estimated using visual features extracted from the image and model of the target. Estimating 3D pose can be useful to ensure global convergence. However, PBVS is highly sensitive to calibration errors and image noise. In contrast, IBVS measures the error signal based on the image and maps it directly to a feedback command. Since it works with error in the image plane, it avoids reconstruction of the cameras relative pose. This makes it suitable for unstructured environments and robust to calibration errors. In this thesis, we only consider IBVS method.

In this subsection, we will derive the image kinematics based on point features and image moment features of a virtual camera. We assume a perspective camera is mounted on the UAV facing downward.

Point features

Let p_o^n be the coordinates of a fixed object represented in the navigation frame, then its coordinates in the body frame will be

$$p_o^b = R^T (p_o^n - p^n)$$

then the dynamics of p_o^b will be

$$\dot{p}_o^b = -\mathrm{sk}(\omega^b) p_o^b - v^b \tag{2.9}$$

which is the same as (2.5a).

Denote p_b^c as the displacement vector from the body frame to the camera frame $\mathcal{C} = \{c_1, c_2, c_3\}$ expressed in the body frame, R_b^c the rotation matrix from the body frame to camera frame as shown in Figure 2.4. Then, the object coordinates in the camera frame $p_o^c = [p_{o1}^c, p_{o2}^c, p_{o3}^c]^T$ can be obtained

$$p_o^c = R_b^c \left(p_o^b - p_b^c \right)$$

For simplicity, we can assume $p_b^c = [0, 0, 0]^T$ and R_b^c is the identity matrix. Then, the frames $\mathcal{C}$ and $\mathcal{B}$ are the same and we can interchange the superscripts b and c.

Projecting p_o^c onto the image plane, we obtain an expression for the normalized
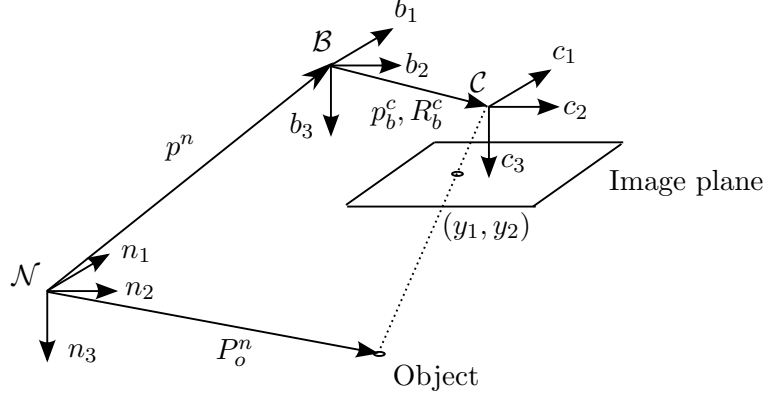
Figure 2.4: Relation between three frames.

image coordinates $[y_1, y_2]^T$:

$$y_1 = f\frac{p^c_{o1}}{p^c_{o3}} = (u - c_u)/\alpha \tag{2.10a}$$

$$y_2 = f\frac{p^c_{o2}}{p^c_{o3}} = (v - c_v) \tag{2.10b}$$

where $[u, v]^T$ are the coordinates of the image point in pixels, $[c_u, c_v]^T$ are the coordinates of the principal point in pixels, f is the focal length in pixels and α is the ratio of pixel dimensions.

Combining (2.9) and (2.10), we obtain

$$\begin{bmatrix} \dot{y}_1 \\ \dot{y}_2 \end{bmatrix} = L \begin{bmatrix} v^b \\ \omega^b \end{bmatrix} \tag{2.11}$$

where

$$L = \begin{bmatrix} -\frac{f}{p^c_{o3}} & 0 & \frac{y_1}{p^c_{o3}} & y_1 y_2 & -(1 + y_1^2) & y_2 \\ 0 & -\frac{f}{p^c_{o3}} & \frac{y_2}{p^c_{o3}} & (1 + y_2^2) & -y_1 y_2 & -y_1 \end{bmatrix}$$

is the interaction matrix.

We notice the depth of the object relative to the camera frame p^c_{o3}, which is always unknown, is needed in (2.11). Therefore, an estimate of the value of p^c_{o3} is necessary in order to use the interaction matrix. [27] compared different choices of approximating the interaction matrix.

Note that to control a 6-DOF UAV, at least 3 noncollinear points are needed. In that case, the total interaction matrix can be obtained by stacking each individual interaction matrix.
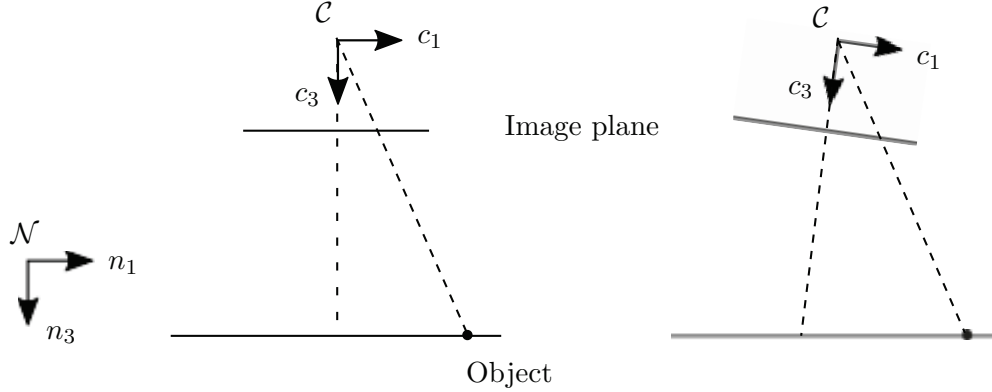
Figure 2.5: Effect of image errors using proportional feedback for angle.

Image moments features using virtual camera model

Visual servoing of UAVs designs a control based on (2.11), (2.5b), (2.4) and (2.6). Unlike traditional motion control problem, the image kinematics (2.11) for point features involves both translational and rotational motions. Note that (2.5b) also includes rotational states, but the term $\mathrm{sk}(\omega^b)$ has a "passivity-like" property. Figure 2.5 demonstrates the difficulty of visual servoing for UAVs when the feedback law for angle is linear in feature error. In order to move the projection of the object to the origin of the image plane, the UAV has to orient away from horizontal in order to generate a thrust in the horizontal direction. This horizontal motion increases the image feature error. As a result, the UAV needs a larger angle to generate a bigger force, and this in turn destabilizes the system.

Recently, a number of approaches have been proposed for visual servoing of UAVs.

1) Backstepping with spherical projection

   As analyzed above, the image kinematics (2.11) for a projective camera is not suitable for cascade controller design. In [31, 81], the passivity-like property is recovered using a spherical camera model. The spherical coordinates of a point can be calculated by $p_{sp} = \frac{1}{\|P_o^b\|} P_o^b$. Then, the image kinematics using spherical projection is derived as

   $$\dot{p}_{sp} = -\mathrm{sk}(\omega^b)p_{sp} - \Pi v^b$$

   where $\Pi = \frac{I - P_o^{bT} P_o^b}{\|P_o^b\|}$ and is unknown. Then, a backstepping technique is used to design the controller. Global exponential stability is obtained for a desired visual feature fixed in the navigation frame [31] and local exponential stability for a fixed target in the camera frame [81]. However, due to the high complexity of the controller, it hasn't been verified by experimental implementation.

2) Virtual spring approach

As shown in Figure 2.5, linear feedback of error leads to instability. In [82], a virtual spring is introduced to prevent from turning the UAV over. The image kinematics are derived using image moments. The controller consists of four terms, which is proved to asymptotically stabilize the system. The analysis is based on the assumption that the image plane is always parallel to the object plane.

3) Virtual image plane approach

This method defines a virtual image plane, which is always parallel to n_1-n_2 plane of navigation frame [83–85]. The coordinates in the virtual image plane are reconstructed using the actual perspective image coordinates and the roll and pitch of the UAV. The biggest advantage of the virtual image plane is that, the coordinates of the object only depends on the UAV's position in the navigation frame regardless of the UAV's roll-pitch motion, i.e., the translational and rotational motions are decoupled. Using the virtual camera frame many traditional control schemes can be applied.

In the following, we will derive the image kinematics of UAVs using image moments features based on a virtual camera model. We first define a virtual camera frame $\mathcal{C}^v = \{c_1^v, c_2^v, c_3^v\}$, whose origin is located at the origin of the camera frame $\mathcal{C}$, as shown in Figure 2.6. Its c_3^v axis is aligned with n_3 of $\mathcal{N}$ and the direction of c_1^v with respect to n_1 is defined by the yaw angle. The orientation of $\mathcal{C}^v$ can also be obtained from $\mathcal{C}$ by rotating around c_1 and c_2 by ϕ and θ. We define a virtual image plane with the same focal length f. Then, the coordinates of the object p_o^n in $\mathcal{C}^v$ is $p_o^v = R_\psi^T(p_o^n - p^n)$. Its dynamics will be

$$\dot{p}_o^v = -\text{sk}(\dot{\psi}b_3)p_o^v - v^v \tag{2.12}$$

where v^v is the UAV's velocity vector in the virtual camera frame.

Its projection on the virtual image plane $[y_1^v, y_2^v]^T$ can be obtained by

$$y_1^v = f\frac{p_{o1}^v}{p_{o3}^v}$$
$$y_2^v = f\frac{p_{o2}^v}{p_{o3}^v}$$

therefore, we can calculate the derivatives based on (2.12)

$$\begin{bmatrix} \dot{y}_1^v \\ \dot{y}_2^v \end{bmatrix} = \begin{bmatrix} -\frac{f}{p_{o3}^v} & 0 & \frac{y_1^v}{p_{o3}^v} \\ 0 & -\frac{f}{p_{o3}^v} & \frac{y_2^v}{p_{o3}^v} \end{bmatrix} v^v + \begin{bmatrix} y_2^v \\ -y_1^v \end{bmatrix} \dot{\psi} \tag{2.13}$$
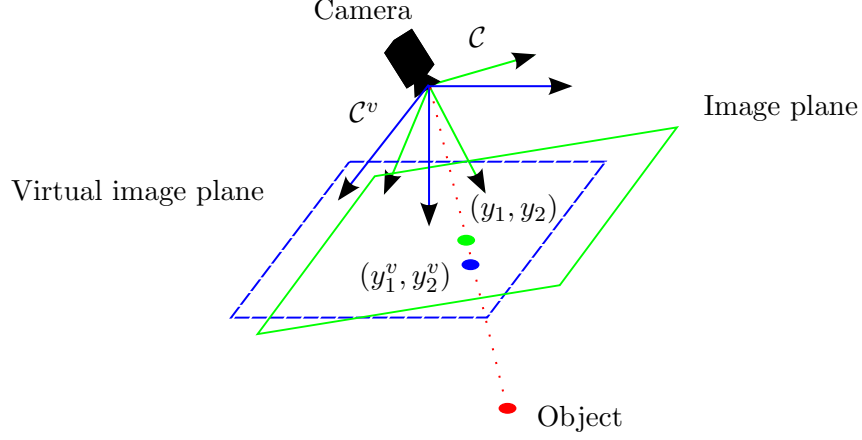
Figure 2.6: Camera frame $\mathcal{C}$ (green) and virtual camera frame $\mathcal{C}^v$ (blue).

The virtual camera coordinates can be obtained from actual image coordinates $[y_1, y_2]^T$, i.e.,

$$
\begin{bmatrix} y_1^v \\ y_2^v \end{bmatrix} = \beta R_\phi R_\theta \begin{bmatrix} y_1 \\ y_2 \end{bmatrix}
\tag{2.14}
$$

where

$$
\beta = f / \left(\begin{bmatrix} 0 & 0 & 1 \end{bmatrix} R_\phi R_\theta \begin{bmatrix} y_1 \\ y_2 \\ f \end{bmatrix} \right).
$$

(2.14) can be seen as the reprojection of image points from $\mathcal{C}$ to $\mathcal{C}^v$.

We assume the target to be planar. Then, the image moments m_{ij} of the object with N_p image points are defined as

$$
m_{ij} = \sum_{k=1}^{N_p} (y_{1k}^v - y_{1g}^v)^i (y_{2k}^v - y_{2g}^v)^j
$$

where $[y_{1k}^v, y_{2k}^v]^T$ is virtual camera coordinates of the kth visible feature point, $k = 1, \ldots, N_p$, and

$$
y_{1g}^v = \frac{1}{N_p} \sum_{k=1}^{N_p} y_{1k}^v, \; y_{2g}^v = \frac{1}{N_p} \sum_{k=1}^{N_p} y_{2k}^v
$$

We know that

$$
\begin{bmatrix} \dot{y}_{1g}^v \\ \dot{y}_{2g}^v \end{bmatrix} = \begin{bmatrix} -\frac{f}{z} & 0 & \frac{y_{1g}^v}{z} \\ 0 & -\frac{f}{z} & \frac{y_{2g}^v}{z} \end{bmatrix} v^v + \begin{bmatrix} y_{2g}^v \\ -y_{1g}^v \end{bmatrix} \dot{\psi}
\tag{2.15}
$$

We assumed the target is planar, hence for all points p_{o3}^v are the same, we use z instead for simplicity. Then, we have

$$\begin{bmatrix} \dot{y}_{1k}^v - \dot{y}_{1g}^v \\ \dot{y}_{2k}^v - \dot{y}_{2g}^v \end{bmatrix} = \begin{bmatrix} 0 & 0 & \frac{y_{1k}^v - y_{1g}^v}{z} \\ 0 & 0 & \frac{y_{2k}^v - y_{2g}^v}{z} \end{bmatrix} v^v + \begin{bmatrix} y_{2k}^v - y_{2g}^v \\ y_{1g}^v - y_{1k}^v \end{bmatrix} \dot{\psi}$$

Therefore,

$$\begin{aligned} \dot{m}_{ij} &= \sum_{k=1}^{N_p} i(y_{1k}^v - y_{1g}^v)^{i-1}(y_{2k}^v - y_{2g}^v)^j (\dot{y}_{1k}^v - \dot{y}_{1g}^v) \\ &\quad + \sum_{k=1}^{N_p} j(y_{1k}^v - y_{1g}^v)^i (y_{2k}^v - y_{2g}^v)^{j-1}(\dot{y}_{2k}^v - \dot{y}_{2g}^v) \\ &= \begin{bmatrix} 0 & 0 & \frac{i+j}{z} m_{ij} \end{bmatrix} v^v + (i m_{i-1,j+1} - j m_{i+1,j-1})\dot{\psi} \end{aligned} \tag{2.16}$$

We define the image moments feature $q = [q_1, q_2, q_3]^T$ as

$$q_1 = q_3 \frac{y_{1g}^v}{f} \tag{2.17a}$$

$$q_2 = q_3 \frac{y_{2g}^v}{f} \tag{2.17b}$$

$$q_3 = \sqrt{\frac{m_{20}^* + m_{02}^*}{m_{20} + m_{02}}} \tag{2.17c}$$

where m_{ij}^* is the desired value of m_{ij}. Then, from (2.17c) and (2.16), we have

$$\dot{q}_3 = -\frac{1}{2} q_3 (m_{20} + m_{02})^{-1}(\dot{m}_{20} + \dot{m}_{02}) = \begin{bmatrix} 0 & 0 & -\frac{q_3}{z} \end{bmatrix} v^v$$

knowing that

$$z\sqrt{m_{20} + m_{02}} = z^* \sqrt{m_{20}^* + m_{02}^*}$$

where z^* is the desired value of z, i.e., the desired normal distance between the camera and the object, we can obtain the dynamics of q_3 as

$$\dot{q}_3 = \begin{bmatrix} 0 & 0 & -\frac{1}{z^*} \end{bmatrix} v^v \tag{2.18}$$

Furthermore, we have

$$\begin{aligned} \dot{q}_1 &= q_3 \frac{\dot{y}_{1g}^v}{f} + \dot{q}_3 \frac{y_{1g}^v}{f} = \begin{bmatrix} -\frac{q_3}{z} & 0 & \frac{q_3 y_{1g}^v}{zf} \end{bmatrix} v^v + q_3 \frac{y_{2g}^v}{f} \dot{\psi} + \begin{bmatrix} 0 & 0 & -\frac{y_{1g}^v}{z^* f} \end{bmatrix} v^v \\ &= \begin{bmatrix} -\frac{1}{z^*} & 0 & 0 \end{bmatrix} v^v + q_2 \dot{\psi} \end{aligned}$$

22

Similarly, we can derive the dynamics of q_2, i.e.,

$$\dot{q}_2 = \begin{bmatrix} 0 & -\frac{1}{z^*} & 0 \end{bmatrix} v^v - q_1 \dot{\psi}$$

Hence, image feature dynamics can be expressed as

$$\dot{q} = -\operatorname{sk}(\dot{\psi} b_3) q - \frac{1}{z^*} v^v \qquad (2.19)$$

The yaw of the UAV can also be controlled by image features. We define the object orientation α as

$$\alpha = \frac{1}{2} \arctan \frac{2m_{11}}{m_{20} - m_{02}}$$

Then the dynamics of α will be

$$\dot{\alpha} = -\dot{\psi}$$

which can be controlled in the inner loop.

2.2 Indoor quadrotor platform

Experimental validation of proposed control laws is essential for demonstrating their practical use. Experiments verify the robustness of performance to various assumptions made at the design stage. For example, experiments can investigate the effect of unavoidable error in state measurements from a motion capture system or on-board navigation system. In this section we introduce the ANCL indoor quadrotor platform which includes a hardware and software component.

2.2.1 Hardware

The ANCL quadrotor platform consists of

- The quadrotor frame (as shown in Figure 2.7). The main hardware components are

  - PX4FMU (Pixhawk autopilot Flight Management Unit) and PX4IO (Pixhawk Input/Output Module). PX4FMU is the main autopilot system and uses an ARM-based 168 MHz microcontroller unit (MCU) with 192KB static RAM MCU with a hardware floating point unit. It also has a 3D accelerometer, a 3D gyroscope, a 3D magnometer, and a pressure sensor. PX4IO provides hardware interfaces, for example UART, and a stable 5V power supply for PX4FMU. Later on, they are repacked into a single board called Pixhawk 1.

Figure 2.7: ANCL quadrotor version 1 (ANCLQ 1.0).

– Radios. The quadrotors have 3DRobotics 915 MHz radio and a LairdTech 2.4 GHz radio to communicate with QGroundControl ground station and Vicon motion capture system, respectively.

– Electronic Speed Controllers (ESCs), motors and propellers. The quadrotors are equipped with 4 Afro 30 A ESCs, 4 Turnigy 1100 KV Brushless Outrunner Motors and 4 APC 12" multi-rotor propellers.

– Battery. Power is supplied by two 3 cell 2600 mAh Lipo batteries.

– Computer vision system.

  ∗ Raspberry Pi (RPi). This is a 700MHz ARM-processor with a camera module with a 5M Pixel sensor. The RPi provides a computer vision system which tracks features and sends image feature coordinates to the PX4FMU via a UART port. Due to its poor performance of image processing, RPi is replaced by Pixy for better performance.

  ∗ Pixy. It can detects hundreds of point objects or blobs in each frame at up to 50 frames per seconds with a resolution of 640×480 pixels. However, Pixy can only detect salient feature points due to its limited computation power. Its application can be found in [86].

In the past several years, two more quadrotors have been built at ANCL as shown in Figure 2.8 and 2.9. The hardware differences between three quadrotors are listed in Table 2.1. Note that ANCLQ 1.0 is used for experiments in Chapter 3 and ANCLQ 2.0 is used for experiments in Chapter 4 and 5.

• Vicon system. Vicon system includes eight Bonita motion capture cameras, as shown in Figure 2.10. The configuration can be done using the Vicon Tracker software. Vicon can accurately estimate the pose of the quadrotor by detecting the position of a number of passive markers mounted on the UAV. This data

Figure 2.8: ANCL quadrotor version 2 (ANCLQ 2.0).

Figure 2.9: ANCL quadrotor version 3 (ANCLQ 3.0).

Table 2.1: Hardware differences between three quadrotors.

Components	ANCLQ 1.0	ANCLQ 2.0	ANCLQ 3.0
Autopilot	PX4FMU PXIO	Pixhawk 1	Pixhawk 1
Radios	3DRobotics LairdTech	Wifly LairdTech	Wifly LairdTech
Propellers	12"	11"	11"
Power	3 cell 2600 mAh LiPo ×2	2 cell 5000 mAh LiPo	2 cell 5000 mAh LiPo
Vision	Rpi / Pixy	Jetson TX1	NA*

* The computer vision module on ANCLQ 3.0 is still under development. Jetson TX2 will be considered.

can be sent to the UAV via the LairdTech radio using a custom Micro Air Vehicle Link (MAVLink) packet. The pose estimates can be generated at a
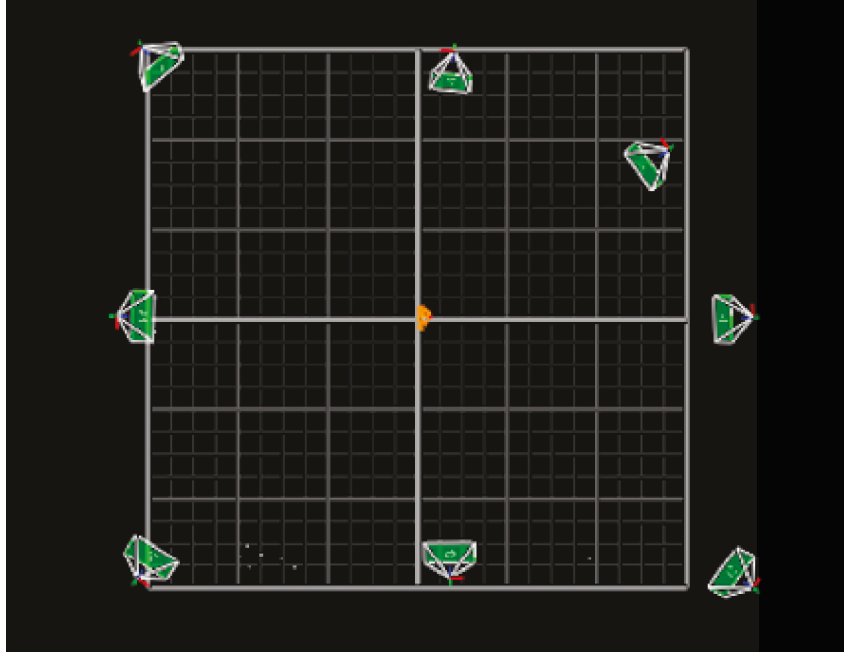
Figure 2.10: Vicon sytem (view from Vicon Tracker).

Figure 2.11: The spektrum DX8 radio transmitter.

frequency of up to $200Hz$.

- QGroundControl ground station. The PX4FMU communicates to the ground control station using the MAVLink protocol. QGroundControl is used as

26

Table 2.2: Control modes description.

Main mode	Secondary mode	Description
1	1	Manual control: the quadrotor is controller by DX8. It is open loop in this mode.
3	1	ANCL Manual control: User control
3	2	ANCL Vicon position control: the quadrotor will hover at $[0, 0, -1]$ m with a PID controller
3	3	ANCL user-defined control: User can design new controllers and test in this mode
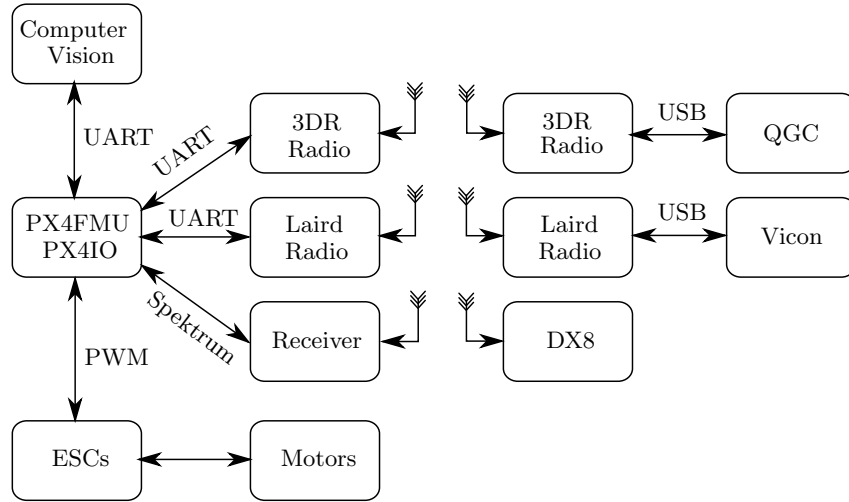
Figure 2.12: Block diagram of the ANCLQ 1.0 quadrotor platform.

ground control software. The ground station can be used for flashing the PX4, calibration of the PX4 navigation system, controller tuning, status monitoring, setting vehicle parameters, and waypoints.

- DX8. The quadrotors are equipped with 8 channel Spektrum satellite receiver paired with a Spektrum DX8 radio transmitter, as shown in Figure 2.11. DX8 will be used for manual control and switching between different control modes. Details are shown in Table 2.2.

The block diagram of the ANCLQ 1.0 autopilot system is shown in Figure 2.12. A typical flight includes the following procedures.

1) Power on the PX4. The system starts all of its sensor's and does a pre ight check.

2) Turn the safety off and engage the motors using DX8.

3) Switch into ANCL manual mode and control the quadrotor to hover in the air using the left stick of DX8.

4) Switch into ANCL position control mode. The quadrotor should hover at $[0, 0, -1]$ m.

5) Switch into ANCL user-defined control mode for further test of new controllers.

6) Switch into ANCL manual mode and control the quadrotor to land.

7) Power off the PX4.

2.2.2 Software

The software for the PX4 autopilot modules runs on top of the very efficient small real-time operating system NuttX, which provides implementations of most standard POSIX OS interfaces to support a rich, multi-threaded development environment for embedded processors. Compared to the original open source PX4 autopilot[1], we add or modify several modules, including Vicon, computer vision and controllers modules. The data flow of the ANCL quadrotor platform is shown in Figure 2.13. Data obtained from internal (e.g. gyroscope and accelerometer) and external (e.g. Vicon) sensors will be transmitted to PX4. After the PX4 has received all of the sensor data, the estimator modules will estimate the vehicle's states. The attitude estimator module (`src/modules/attitude_estimator_q`) mixes roll, pitch and heading estimates from accelerometer and Vicon, and gyroscope measurements. The local position estimator module (`src/modules/local_position_estimator`) uses position and velocity estimates from Vicon as well as the accelerometer data. The inter-process communication is managed by the micro-object request broker (uORB, `src/modules/uORB`). Communication between applications (e.g. read the Vicon data) is implemented based on the publish/subscribe mechanism. The publishers don't send the messages directly to specific subscribers, instead they send messages on a bus and the subscribers receive messages whenever there are updates. This design pattern prevents locking issues and is very common in robotics. The state machine will be maintained by the commander module (`src/modules/commander`), which can control different modes presented in Table 2.2.

The most important group of modules are the controllers. The PX4 autopilot is based on the inner-outer-loop control structure.

- Attitude controller (`src/modules/mc_att_control`)

  The module subscribes the setpoints topic `vehicle_attitude_setpoint` which is calculated and published in `mc_pos_control`, and the actual attitude of the vehicle.

- Position controller (`src/modules/mc_pos_control`)

_____

[1]https://github.com/PX4/Firmware.git
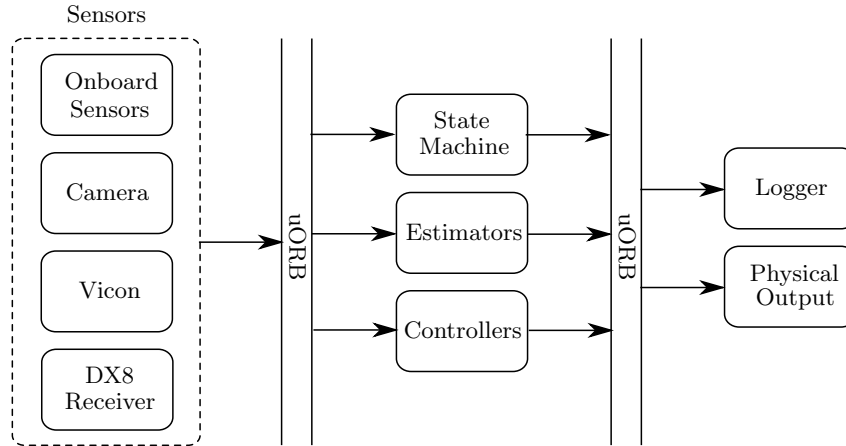
Figure 2.13: PX4 data flow diagram.

This module needs the Vicon system to provide the vehicle's position and velocity. Reference attitude for the inner loop will be calculated. With this controller, the vehicle will be hovering at $[0, 0, -1]^T$ m. This module is corresponding to the ANCL Vicon control mode described in Table 2.2.

- Position nested saturation controller (`src/modules/mc_nsat`)

  This module is corresponding to the controller designed in Chapter 3 and 5. It implements both hovering and line-segment tracking applications and allows for tracking of user-defined trajectory. This controller is set to be triggered when the mode is switched to secondary mode 3 (defined in Table 2.2) and when the parameter `NSAT_ON` is 1. Results with this controller will be shown later.

- Position predictor-based controller (`src/modules/mc_delay`)

  This module implemented the predictor-based controller when time delay appear in the Vicon measurement channel. It is corresponding to the controller designed in Chapter 4. The parameter `DLY_PRED_ON` makes the comparison between the performance with and without the predictor very convenient. When `DLY_PRED_ON` is 1, the vehicle will be controlled by the predictor-based controller. This module is set to be triggered when the mode is switched to secondary mode 3 and when the parameter `NSAT_ON` is 0. Results with this controller will be shown in Chapter 4.

The ESCs will be controlled via Pulse Width Modulation (PWM) signals (`src/drives/px4io`). The logger module (`src/modules/commander`) will record flight data for monitoring and debugging.

Chapter 3

Nonlinear Control with Input Saturation

3.1 Introduction

In this chapter we consider the constrained control of UAVs. The control is inner-outer loop based. We design an inner loop using a conventional PID controller based on a rotational model involving Euler angles. This control tracks reference roll and pitch calculated in the outer loop and a given yaw trajectory. A commonly-used PID structure based on Euler angles is relatively easy to implement and tune on-board, and robust to disturbances. Other parameterizations of the rotation matrix have been used to design the inner loop. For example, rotation matrices [87] or quaternions [88] avoid Euler angle singularities and provide almost global stabilization results. However, we use Euler angles in this section given their improved track record for performance and ease of use. The proposed outer loop generates a saturated thrust and bounded reference for roll and pitch which globally asymptotically stabilize the translational dynamics. We also analyze the performance of the entire inner outer closed-loop and conclude asymptotic stability. The performance of the proposed method is validated experimentally on the ANCL quadrotor test stand.

Unlike many existing approaches, we use the body frame representation of the translational dynamics. This provides two advantages. First, it allows for independent bounds for roll and pitch. In the navigation frame the velocity dynamics leads to roll and pitch references which depend on yaw explicitly. This makes it impossible to individually bound roll and pitch. Secondly, an advantage of using the body frame is that it is similar to the camera frame used in IBVS [31]. Since both frames are rigidly attached to the UAV, the resulting dynamics have similar structure and the proposed method could be applied to this application. In a visual servoing application it is important to individually control roll and pitch since the

image plane is not square.

This chapter is organized as follows. Before starting the controller design, we describe the famous nested saturation method for a chain of integrators in Section 3.2, based on the work in [33]. In Section 3.3, the inner- and outer-loop controllers are proposed and the global asymptotic stability of the outer loop is proven with perfect inner-loop tracking. Then analysis of non-ideal inner loop performance on closed-loop stability is provided. Simulation and experimental results are given in Section 3.4 and 3.5.

3.2   Teel's nested saturation method revisit

In [33], a nested saturation controller for the linear system consisting of multiple integrators was proposed. Here, we summarize the method by taking a second-order linear system for example, i.e.,

$$\dot{x}_1 = x_2$$
$$\dot{x}_2 = u$$

where $x_1, x_2, u \in \mathbb{R}$. Applying the linear coordinate transformation

$$y_1 = x_1 + x_2$$
$$y_2 = x_2$$

we get

$$\dot{y}_1 = y_2 + u \tag{3.1a}$$
$$\dot{y}_2 = u \tag{3.1b}$$

Then, a nested saturation controller was designed, i.e.,

$$u = -\sigma_2(y_2 + \sigma_1(y_1)) \tag{3.2}$$

where σ_i, $i = 1, 2$ are linear saturations, i.e., for $\sigma_i : \mathbb{R} \to \mathbb{R}$, there exist two positive constants L_i, M_i with $L_i \leq M_i$ such that

1). $s\sigma_i(s) > 0$ for all $s \neq 0$;

2). $\sigma_i(s) = s$ when $|s| \leq L_i$;

3). $|\sigma_i(s)| \leq M_i$ for all $s \in \mathbb{R}$.

It was shown in [33] that if

$$M_1 < \frac{1}{2}L_2$$

31

the saturated controller (3.2) will globally stabilize (3.1). The sketched proof is given below.

Consider the Lyapunov function $V_2 = \frac{1}{2}y_2^2$. The derivative of V_2 is given by

$$\dot{V}_2 = -y_2\sigma_2(y_2 + \sigma_1(y_1))$$

Based on property 1) and 3) of σ_2 and the fact that $M_1 < \frac{1}{2}L_2$, we see that $\dot{V}_2 < 0$ for all $y_2 \notin Q_2 = \{y_2||y_2| \le \frac{1}{2}L_2\}$. Therefore, y_2 will enter the set Q_2 in finite time and remains in Q_2 thereafter. Meanwhile, y_1 will remain bounded for any finite time because the right-hand side of (3.1) is globally Lipschitz.

After y_2 enters Q_2, the argument of σ_2 is bounded as

$$|y_2 + \sigma_1(y_1)| \le \frac{1}{2}L_2 + M_1 < L_2$$

i.e., σ_2 operates in its linear region from its property 2). Therefore, (3.1a) becomes

$$\dot{y}_1 = -\sigma_1(y_1)$$

Similarly, for Lyapunov function $V_1 = \frac{1}{2}y_1^2$, we can calculate its derivative as

$$\dot{V}_1 = -y_1\sigma_1(y_1)$$

which is always negative based on the property 1) of σ_1. Hence, in finite time y_1 will enter a set $Q_1 = \{y_1||y_1| \le L_1\}$ and stay within. Inside Q_1, σ_1 will operates in linear region. After this finite time, the closed loop dynamics will be

$$\dot{y}_1 = -y_1$$
$$\dot{y}_2 = -y_1 - y_2$$

which is exponentially stable.

3.3 Controller design

In this section, we will extend the nested saturation method to UAVs. We consider UAVs' dynamics in the body frame as introduced in Section 2.1

$$\dot{p}^b = -\mathrm{sk}(\omega^b)p^b + v^b \tag{3.3a}$$

$$\dot{v}^b = -\mathrm{sk}(\omega^b)v^b + gR^T n_3 - \frac{T}{m}b_3 \tag{3.3b}$$

$$\dot{\eta} = W\omega^b \tag{3.3c}$$

$$J\dot{\omega}^b = -\omega^b \times J\omega^b + \tau^b \tag{3.3d}$$

which is the same as (2.5), (2.8), (2.6). The reason for expressing the translational dynamics in $\mathcal{B}$ is that it prevents ψ from explicitly appearing in (3.3), and this allows us to bound ϕ and θ independently. Specifically, we consider the velocity dynamics in $\mathcal{N}$ with

$$\ddot{p}^n = u^n$$

where

$$u^n = gn_3 - \begin{bmatrix} s_\phi s_\psi + c_\phi s_\theta c_\psi \\ -s_\phi c_\psi + c_\phi s_\theta s_\psi \\ c_\theta c_\phi \end{bmatrix} \frac{T}{m}$$

Solving this equation for T, ϕ, θ gives

$$T = m\|u^n - gn_3\|$$

$$\phi = \arcsin \frac{c_\psi u_2^n - s_\psi u_1^n}{T/m}$$

$$\theta = \arctan \frac{c_\psi u_1^n + s_\psi u_2^n}{u_3^n - g}$$

However, we cannot set individual bound for T, ϕ and θ for any bounds on u_j^n, $j = 1, 2, 3$. This is due to the dependence on ψ.

For the given bounds $u_{m,j}^n$ on u_j^n, the bound on T can be calculated as

$$T_m = m\sqrt{(u_{m,1}^n)^2 + (u_{m,2}^n)^2 + (u_{m,3}^n + g)^2}$$

then, we have

$$\phi_m = \arcsin \frac{\sqrt{(u_{m,1}^n)^2 + (u_{m,2}^n)^2}}{\sqrt{(u_{m,1}^n)^2 + (u_{m,2}^n)^2 + (u_{m,3}^n - g)^2}}$$

$$\psi_m = \arctan \frac{\sqrt{(u_{m,1}^n)^2 + (u_{m,2}^n)^2}}{|u_{m,3}^n - g|}$$

The bounds T_m, ϕ_m, ψ_m are coupled, so they cannot be set arbitrarily.

If we work in $\mathcal{B}$, the velocity dynamics do not have explicitly ψ dependence

$$\theta = -\arcsin \frac{u_1^b}{g}$$

$$\phi = \arcsin \frac{u_2^b}{gc_\theta}$$

$$T = m\left(gc_\theta c_\phi - u_3^b\right)$$

where $u^b = gR^T n_3 - \frac{T}{m} b_3$. This allows us to bound T, ϕ and θ separately, i.e.,

$$\phi_m = \arcsin \frac{u^b_{m,1}}{g}$$

$$\psi_m = \arcsin \frac{u^b_{m,2}}{g}$$

$$T_m = mg + u^b_{m,3}$$

In addition, the work in this section can be used to solve image-based visual servoing problems when a camera is fixed to the UAV [81]. In this case the image kinematics involve both translational and rotational variables which makes stabilization of the nonlinear dynamics a challenge. However, existing nonlinear approaches use state transformations such as spherical coordinates [31, 81] or a virtual camera [89] to put the system into the same form as considered in this chapter.

Initially the control objective is to asymptotically regulate a desired constant position p^n_d in $\mathcal{N}$ for any initial position state. The stabilization is performed accounting for bounds on thrust, roll, and pitch. The desired position in $\mathcal{B}$ is

$$p^b_d = R^T p^n_d$$

and it evolves according to

$$\dot{p}^b_d = -\mathrm{sk}(\omega^b) p^b_d$$

Defining $\delta_1 = p^b - p^b_d$ we obtain

$$\dot{\delta}_1 = -\mathrm{sk}(\omega^b)\delta_1 + v^b \tag{3.4}$$

To achieve our control objective we consider the inner-outer loop control structure shown in Fig. 3.1 to stabilize the dynamics (3.4), (3.3b), (3.3c), (3.3d). This structure is chosen since the rotational dynamics (3.3c) and (3.3d) are independent of translational variables. The inner loop tracks a reference roll ϕ_d and pitch θ_d which are calculated by the outer loop. A reference yaw ψ_d is provided to the inner loop. The outer loop generates a saturated thrust and bounded references ϕ_d and θ_d which globally stabilize the translational dynamics.

3.3.1 Outer-loop control

One of the advantages of using translational dynamics in $\mathcal{B}$ is that ψ does not appear explicitly. On the other hand, as shown in (3.4) and (3.3b), the inner loop variable ω^b appears. Thus, many saturation methods developed, e.g. [90] and [91], cannot be applied directly. Fortunately the term involving ω^b depends on $\mathrm{sk}(\omega^b)$ which is
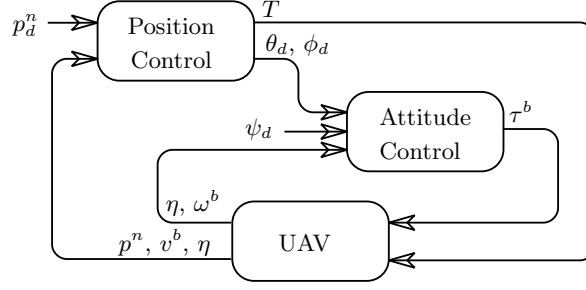
Figure 3.1: Inner-outer loop controller structure.

skew-symmetric, i.e.,

$$x^T \mathrm{sk}(\omega^b) x = 0, \quad \forall x \in \mathbb{R}^3$$

Therefore, it is possible to eliminate ω^b dependence in the derivative of a quadratic Lyapunov-function used for stability analysis. We extend the nested saturation approach for the chain of integrators developed in [33] to our case. The approach can be seen as a vector form of the nested saturation method because all variables are 3-dimensional vectors. In [76] and [92] the nested saturation method has been used for vector variables. The situation is different here because from (3.4) or (3.3b) the three components of the vector δ_1 or v^b are coupled due to the term involving $\mathrm{sk}(\omega^b)$. Thus they cannot be treated separately as three decoupled second order systems as in [76]. Work in [92] considers a fully actuated airship UAV which uses a norm to transform the state vector into a scalar. However, the method leads to a non-smooth input which complicates tracking in the inner-loop if derivatives of the reference angle are required.

We start with the state and input transformations

$$y_1 = k_2 \delta_1 + v^b$$
$$y_2 = v^b$$
$$u = g R^T n_3 - \frac{T}{m} b_3$$

where $k_2 > 0$ is a control gain. In the following, $y_{i,j}$ is denoted as the j-th components of y_i, where $i = 1, 2$ and $j = 1, 2, 3$. Hence, (3.4) and (3.3b) become

$$\dot{y}_1 = -\mathrm{sk}(\omega^b) y_1 + k_2 y_2 + u \tag{3.5a}$$
$$\dot{y}_2 = -\mathrm{sk}(\omega^b) y_2 + u \tag{3.5b}$$

Based on the nested saturation method [33] we choose the outer-loop control

$$u = [u_1, u_2, u_3]^T = -\Sigma_2(k_2 y_2 + \Sigma_1(k_1 y_1)) \tag{3.6}$$

where $k_1 > 0$ is a control gain, $\Sigma_i([s_1, s_2, s_3]^T) = [\sigma_{i,1}(s_1), \sigma_{i,2}(s_2), \sigma_{i,3}(s_3)]^T$, and $\sigma_{i,j}$ is a saturation function with the following properties:

1) $\sigma_{i,j}$ is continuous and nondecreasing;

2) $s_j \sigma_{i,j}(s_j) > 0$ for all $s_j \neq 0$;

3) $\sigma_{i,j}(s_j) = s_j$ for all $|s_j| \leq L_{i,j}$;

4) $|\sigma_{i,j}(s_j)| \leq M_{i,j}$ for all $s_j \in \mathbb{R}$;

5) $M_{1,j} = bL_{2,j}$, where $0 < b < 1$.

The following theorem states the stability result for the outer loop.

Theorem 3.1. *There exist $b, k_1, k_2, L_{2,j}, 1 \leq j \leq 3$ such that outer loop (3.5), (3.6) is globally asymptotically stable with bounded control.*

Proof. First, consider the Lyapunov function

$$V_2 = \frac{1}{2} y_2^T y_2$$

and its derivative will be

$$\dot{V}_2 = -y_2^T \Sigma_2(k_2 y_2 + \Sigma_1(k_1 y_1)) = -\sum_{j=1}^{3} y_{2,j} \sigma_{2,j}(k_2 y_{2,j} + \sigma_{1,j}(k_1 y_{1,j}))$$

Define a set

$$Q_2 = \{y_2 \in \mathbb{R}^3 : k_2 |y_{2,j}| \leq M_{1,j} + aL_{2,j}, j = 1, 2, 3\}$$

where $a > 0$ is to be determined. Now we prove that $\dot{V}_2 < 0$ for all $y_2 \notin Q_2$. Since $k_2 y_2$ has three components we break the proof into three cases.

Case 1: the magnitudes of all three elements of $k_2 y_2$ are larger than $M_{1,j} + aL_{2,j}$, i.e.,

$$|k_2 y_{2,j}| > M_{1,j} + aL_{2,j}$$

where $j = 1, 2, 3$. Then,

$$|k_2 y_{2,j} + \sigma_{1,j}(k_1 y_{1,j})| \geq |k_2 y_{2,j}| - |\sigma_{1,j}(k_1 y_{1,j})|$$
$$> M_{1,j} + aL_{2,j} - M_{1,j} = aL_{2,j}$$

and the sign of $k_2 y_{2,j} + \sigma_{1,j}(k_1 y_{1,j})$ is always determined by $y_{2,j}$, thus

$$-y_{2,j} \sigma_{2,j}(k_2 y_{2,j} + \sigma_{1,j}(k_1 y_{1,j})) < 0$$

36

Therefore,

$$\dot{V}_2 < -aL_{2,1}|y_{2,1}| - aL_{2,2}|y_{2,2}| - aL_{2,3}|y_{2,3}| < 0$$

Case 2: the magnitude of one element of $k_2 y_2$ is less than or equal to $M_{1,j} + aL_{2,j}$. Here, the element $k_2 y_{2,1}$ is considered, i.e.,

$$|k_2 y_{2,1}| \le M_{1,1} + aL_{2,1}$$
$$|k_2 y_{2,j}| > M_{1,j} + aL_{2,j}$$

for $j = 2, 3$. Then,

$$
\begin{aligned}
|k_2 y_{2,1} + \sigma_{1,1}(k_1 y_{1,1})| &\le |k_2 y_{2,1}| + |\sigma_{1,1}(k_1 y_{1,1})| \\
&= 2M_{1,1} + aL_{2,1} = (2b + a)L_{2,1} \\
&\le L_{2,1}
\end{aligned}
$$

if

$$2b + a \le 1 \tag{3.7}$$

then $\sigma_{2,1}$ is evaluated in its linear region, thus

$$
\begin{aligned}
\dot{V}_2 &= -y_{2,1}(k_2 y_{2,1} + \sigma_{1,1}(k_1 y_{1,1})) - \sum_{j=2}^{3} y_{2,j} \sigma_{2,j}(k_2 y_{2,j} + \sigma_{1,j}(k_1 y_{1,j})) \\
&< -k_2 y_{2,1}^2 + M_{1,1}|y_{2,1}| - aL_{2,2}|y_{2,2}| - aL_{2,3}|y_{2,3}| \\
&< -k_2 y_{2,1}^2 + \frac{1}{k_2} M_{1,1}(M_{1,1} + aL_{2,1}) - \frac{1}{k_2} aL_{2,2}(M_{1,2} + aL_{2,2}) - aL_{2,3}|y_{2,3}| \\
&= -k_2 y_{2,1}^2 + \frac{1}{k_2} \left[(1 + \frac{a}{b})M_{1,1}^2 - a(a + b)L_{2,2}^2 \right] - aL_{2,3}|y_{2,3}| \\
&< 0
\end{aligned}
$$

if $(1 + \frac{a}{b})M_{1,1}^2 - a(a + b)L_{2,2}^2 < 0$, i.e.,

$$M_{1,1} < \sqrt{ab}L_{2,2}$$

Since $y_{2,1}$ was chosen arbitrarily above, the general condition is

$$\max_j M_{1,j} < \sqrt{ab} \min_j L_{2,j}$$

Case 3: the magnitudes of two elements of $k_2 y_2$ are no greater than $M_{1,j} + aL_{2,j}$. Suppose they are the first two elements, i.e.,

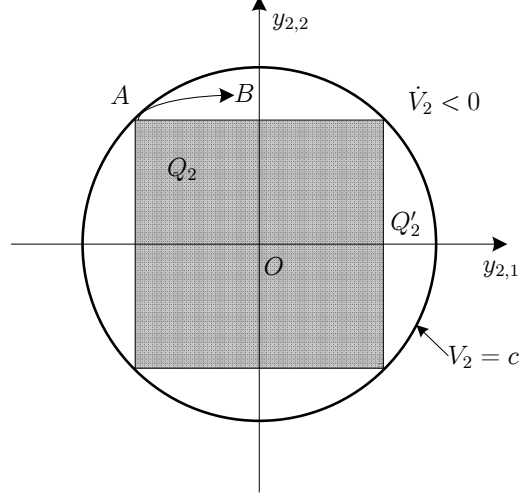$$|k_2 y_{2,j}| \le M_{1,j} + aL_{2,j}$$

Figure 3.2: Relation between Q_2 and Q_2'.

for $j = 1, 2$ and $|k_2 y_{2,3}| > M_{1,3} + aL_{2,3}$. Similarly,

$$
\begin{aligned}
\dot{V}_2 &= -\sum_{j=1}^{2} y_{2,j}(k_2 y_{2,j} + \sigma_{1,j}(k_1 y_{1,j})) - y_{2,3}\sigma_{2,3}(k_2 y_{2,3} + \sigma_{1,3}(k_1 y_{1,3})) \\
&< -k_2 y_{2,1}^2 + M_{1,1}|y_{2,1}| - k_2 y_{2,2}^2 + M_{1,2}|y_{2,2}| - aL_{2,3}|y_{2,3}| \\
&< -k_2 y_{2,1}^2 + \frac{1}{k_2}M_{1,1}(M_{1,1} + aL_{2,1}) - k_2 y_{2,2}^2 \\
&\quad + \frac{1}{k_2}M_{1,2}(M_{1,2} + aL_{2,2}) - \frac{1}{k_2}aL_{2,3}(M_{1,3} + aL_{2,3}) \\
&= -k_2 y_{2,1}^2 - k_2 y_{2,2}^2 + \frac{1}{k_2}\left[(1 + \frac{a}{b})(M_{1,1}^2 + M_{1,2}^2) - a(a+b)L_{2,3}^2\right] \\
&< 0
\end{aligned}
$$

if

$$
\max_j M_{1,j} < \sqrt{\frac{ab}{2}} \min_j L_{2,j} \tag{3.8}
$$

However, Q_2 itself is not an invariant set. As shown in Fig 3.2, where for simplification only the $y_{2,1}$ and $y_{2,2}$-components are shown, the trajectory of y_2 may go from point A to B because $V_2(A) > V_2(B)$. Evidently, $B \notin Q_2$. The smallest invariant set that contains Q_2 is defined as

$$
Q_2' = \{y_2' : V_2(y_2') \le c, c = \max_{y_2 \in Q_2} V_2(y_2)\}
$$

Therefore, based on the analysis above, we conclude that y_2 will enter Q_2' in finite time and remains there. Now we need to ensure Q_2' is enclosed in the region where $\sigma_{2,j}$ is linear.

Within Q_2' the maximum norm of y_2 is

$$\sqrt{\Sigma_{j=1}^3 \left(\frac{M_{1,j} + aL_{2,j}}{k_2}\right)^2} = \frac{a+b}{k_2}\sqrt{\Sigma_{j=1}^3 L_{2,j}^2}$$

If

$$(a+b)\sqrt{\Sigma_{j=1}^3 L_{2,j}^2} \le \min_j L_{2,j} - b\max_j L_{2,j} \qquad (3.9)$$

then

$$|k_2 y_{2,j} + \sigma_{1,j}(k_1 y_{1,j})| \le (a+b)\sqrt{\Sigma_{j=1}^3 L_{2,j}^2} + M_{1,j}$$
$$\le \min_j L_{2,j} - b\max_j L_{2,j} + \max_j M_{1,j}$$
$$\le L_{2,j}$$

Therefore, $\sigma_{2,j}(\cdot) = k_2 y_{2,j} + \sigma_{1,j}(k_1 y_{1,j}), j = 1, 2, 3$ within Q_2'.

For (3.5a) we consider the Lyapunov function

$$V_1 = \frac{1}{2}y_1^T y_1$$

then

$$\dot{V}_1 = y_1^T (k_2 y_2 + \Sigma_2(k_2 y_2 + \Sigma_1(k_1 y_1)))$$

From the discussion above, we know y_2 will eventually converge to the invariant set Q_2' and the trajectory of y_2 is bounded. Thus, in the region where $\|y_1\| \ge \|k_2 y_2 + \Sigma_2(k_2 y_2 + \Sigma_1(k_1 y_1))\|$, we have

$$\dot{V}_1 \le \|y_1\|\|k_2 y_2 + \Sigma_2(k_2 y_2 + \Sigma_1(k_1 y_1))\|$$
$$\le \|y_1\|^2 = 2V_1$$

From Gronwall-Bellman inequality,

$$V_1(t) \le V_1(t_0)e^{2(t-t_0)}$$

where t_0 is the time when $\|y_1\| \ge \|y_2 + \Sigma_2(k_2 y_2 + \Sigma_1(k_1 y_1))\|$ for $t > t_0$. Therefore, in finite time V_1 is bounded which implies the boundedness of y_1.

After y_2 enters Q_2', (3.6) becomes

$$u = -k_2 y_2 - \Sigma_1(k_1 y_1)$$

thus the dynamics of y_1 becomes

$$\dot{y}_1 = -\text{sk}(\omega^b)y_1 - \Sigma_1(k_1 y_1)$$

The derivative of Lyapunov function V_1 along the trajectory of y_1 is always negative because

$$\dot{V}_1 = -y_{1,1}\sigma_{1,1}(k_1 y_{1,1}) - y_{1,2}\sigma_{1,2}(k_1 y_{1,2}) - y_{1,3}\sigma_{1,3}(k_1 y_{1,3}) \leq 0$$

and $\dot{V}_1 < 0$, for all $y_1 \neq 0$. Thus, $y_{1,j}$ will enter the linear region of $\sigma_{1,j}$.

When $\sigma_{1,j}$ and $\sigma_{2,j}$ are linear, then (3.5) becomes

$$\dot{y}_1 = -\text{sk}(\omega^b)y_1 - k_1 y_1$$
$$\dot{y}_2 = -\text{sk}(\omega^b)y_2 - k_1 y_1 - k_2 y_2$$

For the Lyapunov function $V_3 = V_1 + V_2$, we have

$$\dot{V}_3 = -k_1 y_1^T y_1 - k_1 y_1^T y_2 - k_2 y_2^T y_2$$
$$= -k_1 (y_1 + \frac{1}{2}y_2)^T (y_1 + \frac{1}{2}y_2) - (k_2 - \frac{1}{4}k_1)y_2^T y_2$$

$\dot{V}_3 < 0$ if the gains satisfy

$$k_2 > \frac{1}{4}k_1$$

then the equilibrium point of (3.5), (3.6) is globally asymptotically stable.

If $L_{2,1} = L_{2,2} = L_{2,3}$, the values of a and b can be given explicitly. Conditions (3.7), (3.8), (3.9) can be simplified to

$$2b + a \leq 1$$
$$2b < a$$
$$(\sqrt{3} + 1)b + \sqrt{3}a \leq 1$$

This yields

$$b < \frac{1}{1 + 3\sqrt{3}}$$
$$2b < a \leq \frac{1}{\sqrt{3}} - (1 + \frac{1}{\sqrt{3}})b$$

We can guarantee the existence of $M_{i,j}, L_{i,j}$ since for all $M_{2,j}$ we can always choose

$$L_{2,1} = L_{2,2} = L_{2,3} = \min_j M_{2,j} - \varepsilon$$

where ε is taken sufficiently small. $\qquad \square$

Based on the outer-loop controller, the reference angles to the inner loop and

thrust T can be calculated as

$$\theta_d = -\arcsin \frac{u_1}{g} \tag{3.10a}$$

$$\phi_d = \arcsin \frac{u_2}{gc_{\theta_d}} \tag{3.10b}$$

$$T = m \left(gc_{\theta_d}c_{\phi_d} - u_3 \right) \tag{3.10c}$$

Remark 3.2. In the design process we typically begin with bounds on roll ϕ_m, pitch θ_m, and thrust T_m. Next, we calculate the bound $u_m = [u_{m,1}, u_{m,2}, u_{m,3}]^T$ of u according to

$$u_{m,1} = gs_{\theta_m}$$

$$u_{m,2} = gc_{\theta_m}s_{\phi_m}$$

$$u_{m,3} = \frac{T_m}{m} - g$$

then we choose $L_{2,j}, M_{2,j}$ satisfying $L_{2,j} < M_{2,j} \le u_{m,j}$ and b based on conditions (3.7), (3.8), and (3.9).

Remark 3.3. To remove steady error which arises in practice (e.g. due to attitude estimate error) the control can be augmented with an integrator state ξ satisfying $\dot{\xi} = -\operatorname{sk}(\omega^b)\xi + \delta_1$. By redefining

$$y_1 = k_2 k_3 \xi + (k_2 + k_3)\delta_1 + v^b$$

$$y_2 = k_3 \delta_1 + v^b$$

$$y_3 = v^b$$

we obtain the augmented error system

$$\dot{y}_1 = -\operatorname{sk}(\omega^b)y_1 + k_2 y_2 + k_3 y_3 + u$$

$$\dot{y}_2 = -\operatorname{sk}(\omega^b)y_2 + k_3 y_3 + u$$

$$\dot{y}_3 = -\operatorname{sk}(\omega^b)y_3 + u$$

Then the controller

$$u = -\Sigma_3(k_3 y_3 + \Sigma_2(k_2 y_2 + \Sigma_1(k_1 y_1))) \tag{3.11}$$

will globally asymptotically stabilize the outer loop provided

$$\begin{bmatrix} k_1 & \frac{k_1}{2} & \frac{k_1}{2} \\ \frac{k_1}{2} & k_2 & \frac{k_2}{2} \\ \frac{k_1}{2} & \frac{k_2}{2} & k_3 \end{bmatrix} > 0 \tag{3.12}$$

41

This condition is satisfied with

$$k_1 > 0$$

$$k_2 > \frac{1}{4}k_1$$

$$k_3 > \frac{k_2^2}{4k_2 - k_1}$$

Remark 3.4. For simplicity, we use scalar gains k_i in (3.11). However, it is possible to generalize to matrix gains $K_i = \text{diag}(k_{i,1}, k_{i,2}, k_{i,3}), i = 1, 2, 3$. In this case we have three conditions on the gain matrices which are similar to (3.12) with k_i replaced by $k_{i,j}, j = 1, 2, 3$.

The proposed control can be extended to constrained output tracking problems where p_d^n is a time-varying function in $\mathcal{N}$.

Corollary 3.5. *Suppose the desired position $p_d^n(t) = [p_{d,1}^n(t), p_{d,2}^n(t), p_{d,3}^n(t)]^T$ is such that $\ddot{p}_{d,1}^n = \ddot{p}_{d,2}^n = 0$ and $|\ddot{p}_{d,3}^n| \leq \epsilon < g$. Then there exists a bounded control which asymptotically tracks p_d^n and satisfies constraints $|\phi_d| \leq \phi_m$, $|\theta_d| \leq \theta_m$ and $|T| \leq T_m$, where $\phi_m, \theta_m < 90°$, $T_m > m(g + \epsilon)$.*

Proof. The trajectory of p_d^n in $\mathcal{B}$ is $p_d^b = R^T p_d^n$ and

$$\dot{p}_d^b = R^T \dot{p}_d^n + \dot{R}^T p_d^n = -\text{sk}(\omega^b)p_d^b + R^T \dot{p}_d^n$$

By defining

$$\tilde{\delta}_1 = p^b - p_d^b$$
$$\tilde{\delta}_2 = v^b - R^T \dot{p}_d^n$$

we obtain

$$\dot{\tilde{\delta}}_1 = -\text{sk}(\omega^b)\tilde{\delta}_1 + \tilde{\delta}_2 \tag{3.13a}$$

$$\dot{\tilde{\delta}}_2 = -\text{sk}(\omega^b)\tilde{\delta}_2 + \tilde{u} \tag{3.13b}$$

where

$$\tilde{u} = (g - \ddot{p}_{d,3}^n)R^T n_3 - \frac{T}{m}b_3$$

From Theorem 3.1 there exists a bounded controller

$$\tilde{u} = -\tilde{\Sigma}_2(\tilde{k}_2\tilde{\delta}_2 + \tilde{\Sigma}_1(\tilde{k}_1\tilde{k}_2\tilde{\delta}_1 + \tilde{k}_1\tilde{\delta}_2))$$

stabilizing dynamics (3.13). The parameters $\tilde{M}_{2,j}$ of $\tilde{\Sigma}_2$ can be chosen as

$$\tilde{M}_{2,1} \leq (g - \epsilon)s_{\theta_m}$$
$$\tilde{M}_{2,2} \leq (g - \epsilon)c_{\theta_m}s_{\phi_m}$$
$$\tilde{M}_{2,3} \leq \frac{T_m}{m} - (g + \epsilon)$$

The remaining parameters in $\tilde{\Sigma}_1, \tilde{\Sigma}_2$ can be determined following the same procedure in Remark 3.2. Next, the thrust and reference roll, pitch are

$$\theta_d = -\arcsin\frac{\tilde{u}_1}{g - \ddot{p}_{d,3}^n} \tag{3.14a}$$

$$\phi_d = \arcsin\frac{\tilde{u}_2}{(g - \ddot{p}_{d,3}^n)c_{\theta_d}} \tag{3.14b}$$

$$T = m\left((g - \ddot{p}_{d,3}^n)c_{\theta_d}c_{\phi_d} - \tilde{u}_3\right) \tag{3.14c}$$

The proof of boundedness is straightforward, e.g.

$$|\theta_d| \leq |\arcsin\frac{\tilde{M}_{2,1}}{g - \ddot{p}_{d,3}^n}| \leq |\arcsin\frac{(g - \epsilon)s_{\theta_m}}{g - \ddot{p}_{d,3}^n}| \leq |\arcsin s_{\theta_m}| = \theta_m$$

$$\square$$

Remark 3.6. When $\ddot{p}_{d,1}^n, \ddot{p}_{d,2}^n \neq 0$ and are bounded, $\tilde{u}$ becomes $\tilde{u} = R^T(gn_3 - \ddot{p}_d^n) - \frac{T}{m}b_3$, therefore, the reference angles θ_d and ϕ_d cannot be solved using (3.14a) and (3.14b). However, we can treat the term $R^T[\ddot{p}_{d,1}^n, \ddot{p}_{d,2}^n, 0]^T$ as a disturbance whose bound is determined by $\ddot{p}_{d,1}^n$ and $\ddot{p}_{d,2}^n$. As long as

$$\max\{|\ddot{p}_{d,1}^n|, |\ddot{p}_{d,2}^n|\} < \min\{M_{2,1}, M_{2,2}\}$$

a bounded tracking result can be guaranteed and the tracking performance is determined by the bounds of $\ddot{p}_{d,1}^n$ and $\ddot{p}_{d,2}^n$.

3.3.2 Inner-loop controller

The control design of the rotational dynamics subsystem is well-studied, e.g. [87, 88]. Our approach uses a simple PID controller to track given angles ϕ_d, θ_d, and ψ_d. The roll and pitch setpoints are from (3.10b), (3.10a) or (3.14a), (3.14b). The yaw reference is provided externally. We assume $\dot{\psi}_d, \ddot{\psi}_d$ are bounded and known. By defining $e_\eta = \eta - \eta_d$, where $\eta_d = [\phi_d, \theta_d, \psi_d]^T$, the inner loop can be written as

$$\dot{e}_\eta = e_\omega + d_1$$
$$\dot{e}_\omega = \bar{\tau}^b + d_2$$

where

$$e_\omega = W\omega^b - \bar{E}_3 \dot{\eta}_d$$

$$d_1 = -\bar{E}_{12} \dot{\eta}_d$$

$$\bar{\tau}^b = \dot{W}\omega + W(-J^{-1}\omega^b \times J\omega^b + J^{-1}\tau^b) - \bar{E}_3 \ddot{\eta}_d$$

$$d_2 = -\bar{E}_{12} \ddot{\eta}_d$$

$$\bar{E}_{12} = \text{diag}([1,1,0])$$

$$\bar{E}_3 = \text{diag}([0,0,1])$$

We treat d_1 and d_2 as disturbances. One reason for introducing d_1, d_2 as disturbances is to avoid the control having dependence on the first and second derivatives of θ_d and ϕ_d. Computing these derivatives would introduce noise to the closed-loop which decreases its performance. The computation of $\dot{\phi}_d, \ddot{\phi}_d, \dot{\theta}_d, \ddot{\theta}_d$ is commonly avoided in practice for that reason [4, 25].

The inner-loop PID controller is given by

$$\bar{\tau}^b = -k_p^a e_\eta - k_i^a \int_0^t e_\eta(\tau)d\tau - k_d^a e_\omega \tag{3.15}$$

Then, we can calculate the actual control torque τ^b using (3.15).

With the Lyapunov

$$V_4 = \alpha \int_0^t e_\eta^T(\tau)d\tau k_i^a \int_0^t e_\eta(\tau)d\tau + 2e_\eta^T k_i^a \int_0^t e_\eta(\tau)d\tau$$
$$+ e_\eta^T(k_p^a + \alpha k_d^a)e_\eta + \alpha e_\eta^T e_\omega + e_\omega^T e_\omega$$

we have

$$\dot{V}_4 = -e_\eta^T(\alpha k_p^a - k_i^a)e_\eta - e_\omega^T(k_d^a - \alpha \bar{E})e_\omega$$

where $\bar{E}$ is an identity matrix of order 3, the inner loop with $d_1 = d_2 = 0$ can be exponentially stabilized with (3.15) if

$$\alpha k_p^a > k_i^a$$

$$k_d^a > \alpha \bar{E}$$

Other parameterizations of the rotation matrix R have been used to design the inner loop. For example, rotation matrices [87] or quaternions [88] avoid Euler angle singularities and provide almost global stabilization results. We choose Euler angles since they lead to a simple PID control structure for the inner loop. This simplicity provides practical benefits such as ease of tuning, reduced computational complexity

44

for on-board implementation, and robustness to disturbances [69]. Euler angles have been widely used in the recent literature, e.g. [6, 8, 75, 93] and are standard on most field tested autopilots, e.g. [2, 19]. As mentioned in Section 2.1.2, the "ZYX" Euler angles have singularities at $\theta = (2k+1)\frac{\pi}{2}, k \in \mathbb{Z}$, but they can be avoided using the saturated control proposed in this chapter.

3.3.3 Closed-loop stability analysis

In this subsection we analyze the effect of the inner loop tracking error on closed-loop stability. The closed-loop system is given by

$$\dot{y}_1 = -\operatorname{sk}(\omega^b)y_1 + k_2 y_2 + u + \delta_\eta \tag{3.16a}$$

$$\dot{y}_2 = -\operatorname{sk}(\omega^b)y_2 + u + \delta_\eta \tag{3.16b}$$

$$\dot{e}_\eta = e_\omega + d_1 \tag{3.16c}$$

$$\dot{e}_\omega = \bar{\tau}^b + d_2 \tag{3.16d}$$

where u and $\bar{\tau}^b$ are given in (3.6) and (3.15), and

$$\delta_\eta = g[s_{\theta_d} - s_\theta, c_\theta s_\phi - c_{\theta_d} s_{\phi_d}, c_\theta c_\phi - c_{\theta_d} c_{\phi_d}]^T$$

Hence, $\|\delta_\eta\| < c_1 \|\bar{E}_{12} e_\eta\|$. We consider a region where $\|e_\eta\| < \zeta_\eta, \|e_\omega\| < \zeta_\omega$ and use the linear approximation of d_1, d_2, i.e.,

$$d_1 \approx \frac{1}{g} \dot{u} \bar{E}_{21}$$

$$d_2 \approx \frac{1}{g} \ddot{u} \bar{E}_{21}$$

where

$$\bar{E}_{21} = \begin{bmatrix} 0 & 1 & 0 \\ 1 & 0 & 0 \\ 0 & 0 & 0 \end{bmatrix}$$

Moreover, we assume $\dot{\sigma}_{i,j}(x), \ddot{\sigma}_{i,j}(x) = 0$, for $|x| > \zeta_{i,j} + L_{i,j}$.

First, we consider the case when the control is saturated with $\dot{\Sigma}_2, \ddot{\Sigma}_2 = 0$, i.e.,

$$|y_{2,j}| > \zeta_{2,j} + L_{2,j} + M_{1,j}$$

Hence, $d_1, d_2 = 0$. From Section 3.3.2, we know that the inner loop is exponentially stable, thus there exists a time T^* such that

$$\|\delta_\eta(t)\| < c_1 \|\bar{E}_{12} e_\eta(t)\| < \min \zeta_{2,j}$$

for all $t > T^*$. With Lyapunov function V_2, we have

$$\dot{V}_2 < -\sum_{j=1}^{3} |y_{2,j}|(\zeta_{2,j} + L_{2,j} - \|\delta_\eta\|) < 0$$

Next, we consider the case when some components of Σ_2 become linear, for example $\sigma_{2,1}, \sigma_{2,2}$. Then,

$$d_1 = \frac{1}{g}(k_2^2 y_2 + f_1(e_\omega)y_2)\bar{E}_{21}$$

$$d_2 = \frac{1}{g}(-k_2^3 y_2 + f_2(e_\eta, e_\omega)y_2)\bar{E}_{21}$$

Since $\|e_\eta\| < \zeta_\eta, \|e_\omega\| < \zeta_\omega$, we have $\|f_1\| < \bar{f}_1$ and $\|f_2\| < \bar{f}_2$. Thus, based on the Lyapunov function $V_5 = V_2 + V_4$, we have

$$\begin{aligned}
\dot{V}_5 < &- k_2 y_{2,1}^2 - k_2 y_{2,2}^2 + \sum_{j=1}^{2} |y_{2,j}|(M_{1,j} + \|\delta_\eta\|) \\
&- |y_{2,3}|(L_{2,3} + \zeta_{2,3} - \|\delta_\eta\|) - e_\eta^T(\alpha k_p^a - k_i^a)e_\eta \\
&- e_\omega^T(k_d^a - \alpha\bar{E})e_\omega + \frac{1}{g}\sum_{j=1}^{2}(k_2^2 + \bar{f}_1)|y_{2,j}|\|e_\eta\| \\
&+ \frac{1}{g}\sum_{j=1}^{2}(-k_2^3 + \bar{f}_2)|y_{2,j}|\|e_\omega\|
\end{aligned}$$

If $2(\max_j M_{1,j} + c_1\zeta_\eta) < \min_j L_{2,j}$ and $\min_j \zeta_{2,j} > c_1\zeta_\eta$, we can find $\alpha, k_p^a, k_i^a, k_d^a, \zeta_\eta, \zeta_\omega$ such that $\dot{V}_5 < 0$. Similarly, we can use the same method of proof for the other cases. Then, we can conclude that the saturation function Σ_2 will become linear. The same procedure can be used to prove that Σ_1 will become linear eventually.

After Σ_1, Σ_2 become linear, (3.16a), (3.16b) become

$$\dot{y}_1 = -\text{sk}(\omega^b)y_1 - k_1 y_1 + \delta_\eta$$

$$\dot{y}_2 = -\text{sk}(\omega^b)y_2 - k_1 y_1 - k_2 y_2 + \delta_\eta$$

In this case, d_1, d_2 can be written as

$$d_1 = \frac{1}{g}(k_2^2 y_2 + (k_1 k_2 + k_1^2)y_1 + g_1(e_\omega)y_1 + g_2(e_\omega)y_2))\bar{E}_{21}$$

$$d_2 = \frac{1}{g}(-k_2^3 y_2 - (k_1 k_2^2 + k_1^2 k_2 + k_1^3)y_1 + h_1(e_\eta, e_\omega)y_1 + h_2(e_\eta, e_\omega)y_2))\bar{E}_{21}$$

where g_1, g_2, h_1, h_2 are bounded. The asymptotic stability can be proven using the

46

Table 3.1: Nominal quadrotor model parameters

m	1.6 kg
J	$\text{diag}(0.03, 0.03, 0.05) \text{ kg} \cdot \text{m}^2$
J_r	$0.0002 \text{ kg} \cdot \text{m}^2$
l	0.25 m

Lyapunov function $V_6 = V_3 + V_4$, since

$$\dot{V}_6 \leq - k_1 y_1^T y_1 - k_1 y_1^T y_2 - k_2 y_2^T y_2 + c_1 \|e_\eta\| \|y_1\| + c_1 \|e_\eta\| \|y_2\|$$
$$- e_\eta^T (\alpha k_p^a - k_i^a) e_\eta - e_\omega^T (k_d^a - \alpha \bar{E}) e_\omega + e_\eta^T d_1 + e_\omega^T d_2$$

The last two terms are dot products of y_1, y_2 and e_η, e_ω. Therefore, there always exists $\alpha, k_p^a, k_i^a, k_d^a, \zeta_\eta, \zeta_\omega$ such that $\dot{V}_6 < 0$. We can conclude that the closed-loop system is locally asymptotic stable, i.e., for any $y_1, y_2 \in \mathbb{R}^3$ and $e_\eta(0), e_\omega(0)$ sufficiently close to 0, the state of the closed-loop (3.16) converges to 0.

3.4   Simulation

In this section the proposed control is simulated. The simulation is intended to model the indoor ANCL quadrotor platform. The nominal model parameters of quadrotor are in Table 3.1. In order to test the robustness of the controller a number of unmodelled effects are introduced: gyroscopic torque due to rotor inertia, measurement noise, measurement delay, and wind gust disturbances.

Unmodelled dynamics   In (2.7), the external torque does not include terms due to nonzero rotor inertia J_r. This model error is included in the simulation by including τ_g^b and τ_r^b as introduced in Section 2.1.2.

Measurements error   The translational components of the system state are obtained from the position estimate provided by the Vicon system. Linear velocity is obtained by low-pass numerical differentiation of these position estimates. The rotational components of the system states come from an on-board Attitude and Heading Reference System (AHRS). This system consists of an Inertial Measurement Unit (IMU) and magnetometer feeding a Kalman filter. Both the Vicon system and AHRS introduce measurement noise to the state estimate which is modeled in the simulation.

Time delay   Non-negligible delays are introduced by wireless modem latency, on-board processing delay, or ground station filtering for the velocity. In our simulation,

we model this delay by adding one sample time delay to the position and angular velocity loops, and two samples time delay to the linear velocity.

Wind gust disturbance Atmospheric turbulence is significant, especially for outdoor missions. To simulate these effects we use the von Karman model whose spectra for longitudinal, lateral and vertical velocity are represented as [94]

$$H_u = \frac{\sigma_u \sqrt{\frac{2L_u}{\pi V}} + 0.25\frac{L_u}{V}s}{1 + 1.357\frac{L_u}{V}s + 0.1987\frac{L_u^2}{V^2}s^2}$$

$$H_v = \frac{\sigma_v \sqrt{\frac{L_v}{\pi V}} + 2.7478\frac{L_v}{V}s + 0.3398\frac{L_v^2}{V^2}s^2}{1 + 2.9958\frac{L_v}{V}s + 1.9754\frac{L_v^2}{V^2}s^2 + 0.1539\frac{L_v^3}{V^3}s^3}$$

$$H_w = \frac{\sigma_w \sqrt{\frac{L_w}{\pi V}} + 2.7478\frac{L_w}{V}s + 0.3398\frac{L_w^2}{V^2}s^2}{1 + 2.9958\frac{L_w}{V}s + 1.9754\frac{L_w^2}{V^2}s^2 + 0.1539\frac{L_w^3}{V^3}s^3}$$

where L_u, L_v and L_w are the scales of turbulence which depend on the UAV's height for lower altitudes, i.e.,

$$L_w = p_3^n$$

$$L_u = L_v = \frac{p_3^n}{(0.177 + 0.000823p_3^n)^{1.2}}$$

Here we use the desired height for p_3^n.

The turbulence intensities σ_u, σ_v, and σ_w can be calculated as

$$\sigma_w = 0.1W_{20}$$

$$\sigma_u = \sigma_v = \frac{\sigma_w}{(0.177 + 0.000823p_3^n)^{0.4}}$$

where W_{20} is the given wind speed in knots at 20 ft altitude. V is the relative speed of the UAV to the air stream. For simplicity we set V to a constant. The parameters of the wind turbulence model used in the simulation are in Table 3.2. The wind gust is generated by filtering white noise with the above filters. We add the wind turbulence as a disturbance to the rotational rates in the simulation [94].

Table 3.2: Wind turbulence parameters

W_{20}	3 m/s
L_ω	1.2 m
V	0.05 m/s

We assume the UAV is initially hovering at $p^n(0) = [-1, -1, -0.8]^T$ m and the desired position is $p_d^n = [0, 0, -1.2]^T$ m. All the other initial states are set to zero.

The desired yaw is 17°. The bound for pitch $\theta_{max} = 22.9°$. We take $M_{2,1} = gs_{\theta_{max}} \approx$ 3.8163 and for simplicity take $M_{2,1} = M_{2,2} = M_{2,3}$ which means the bound of roll and thrust are $\phi_{max} = \arcsin(t_{\theta_{max}}) \approx 25.0°$ and $T_{max} = m(g + M_{2,1}) \approx 21.7861$ N. We use a PD controller in the inner loop, i.e., $\tau^b = -k_\eta(\eta - \eta_d) - k_\omega(\dot{\eta} - \dot{\eta}_d) + \ddot{\eta}_d$. Parameters for the controller are listed in Table 3.3.

Table 3.3: Simulation control parameters

k_1	0.9
k_2	0.8
$M_{2,j}$	3.8163
b	0.1614
$L_{2,j}$	$0.99M_{2,j}$
$L_{1,j}$	$0.99M_{1,j}$
k_η	4
k_ω	1.2

A smooth nondecreasing saturation function $\sigma_{i,j}$ is chosen as

$$\sigma_{i,j}(x) = \begin{cases} x, & \text{if } |x| \le L_{i,j} \\ \text{sign}(x)\left(L_{i,j} + \frac{\beta_{i,j} - \beta_{i,j}e^{-2(|x|-L_{i,j})}}{1+(2\beta_{i,j}-1)e^{-2(|x|-L_{i,j})}}\right), \text{ow.} \end{cases} \quad (3.18)$$

where $\beta_{i,j} = M_{i,j} - L_{i,j}$.

The 3D trajectory shown in Figure 3.3 demonstrates the UAV reaches a small region about the desired position after about 7 seconds and stays in that region for $t \ge 7$ s. The boundedness of the trajectory, instead of asymptotic convergence, is due to the disturbances introduced. From Figure 3.4 we can see the radius of the region is about 20 cm. The trajectories of the Euler angles given in Figure 3.5 shows that roll and pitch are always within their prescribed bounds. Indeed, the angles are always smaller than 5°, which is significantly smaller than the prescribed bounds. The reason for this is that for the initial condition considered states mostly stay within the linear region of saturation functions. Figure 3.6 shows an example simulation of the case where angles reach their limits. We can conclude from the above simulation that the proposed controller provides satisfactory performance in face of unmodelled disturbances.

3.5   Experiments

In this section the proposed controller is tested on the indoor ANCL quadrotor platform. The experiments are implemented on ANCLQ 1.0.

We consider two different cases: hovering and tracking linear reference outputs. For both cases, we use the same inner loop parameters, i.e., $\hat{k}_p^a = \text{diag}\,(0.333, 0.345, 0.3)$,
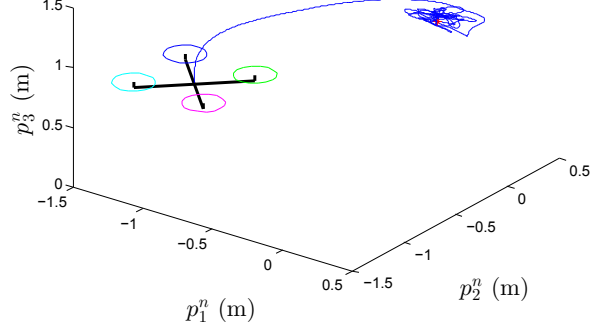
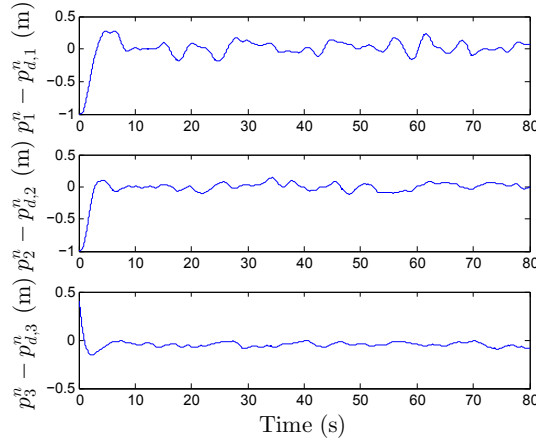Figure 3.3: Simulation: 3D trajectory of the quadrotor.

Figure 3.4: Simulation: Tracking error $p^n - p_d^n$.

$\hat{k}_i^a = \text{diag}\,(0.03, 0.03, 0.05)$, and $\hat{k}_d^a = \text{diag}\,(0.089, 0.095, 0.1)$, Note that the gains are different from the ones in (3.15), since in our platform we use the normalized control signal [95]. We remark that, in our experiment we neglect the nonlinear terms in τ^b, i.e., we use $\tau^b \approx J\bar{\tau}^b$. The saturation function $\sigma_{i,j}$ in the outer loop is chosen as (3.18).

3.5.1 Case 1: Hovering

The desired position is set to $p_d^n = [0, 0, -1.2]^T$ m. The desired yaw is $\psi_d = 0°$. Initially the quadrotor is manually controlled to fly near the origin of $\mathcal{N}$. The nested saturation controller is switched on at around $t = 31$ s and switched off around $t = 59$ s. To remove steady error the augmented controller with integral term (3.11) is used. We set the bound for pitch $\theta_m = 27.3°$. This leads to $M_{3,1} = gs_{\theta_m} \approx 4.5$. For simplicity we choose $M_{3,1} = M_{3,2} = M_{3,3}$, which means we obtain bounds $\phi_m = \arcsin(t_{\theta_m}) \approx 31.1°$ and $T_m = m(g + M_{3,1}) \approx 22.9$ N. Parameters for the controller are listed in Table 3.4. Figure 3.7 gives the position trajectories of the
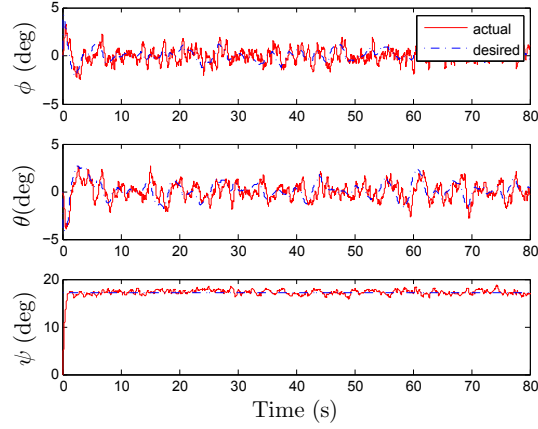
Figure 3.5: Simulation: Trajectories of Euler angles.
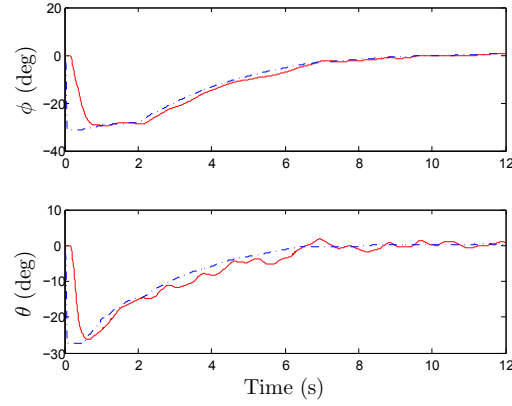
Figure 3.6: Simulation: Trajectories of Euler angles with initial velocity $[-9, 9, 0]$ m/s.

Table 3.4: Experimental control parameters

k_1	1.0
k_2	0.8
k_3	3.6
$M_{3,j}$	4.5
b	0.1614
$L_{i,j}$	$0.95M_{i,j}$

quadrotor and thrust input. The average magnitudes of the error in steady state in the p_1^n and p_2^n direction are 1.5 cm and 3.5 cm, respectively. The curves of ϕ, θ, and ψ are shown in Figure 3.8. In the figures we use dash-dot blue lines to denote the desired value and solid red line for the actual value.

Figure 3.7: Experiments: Trajectories of position p^n and thrust T for hovering.
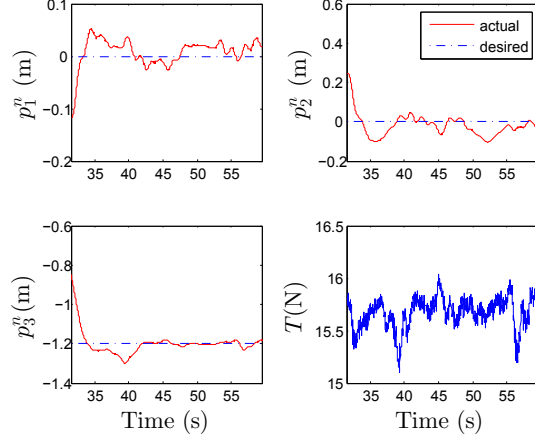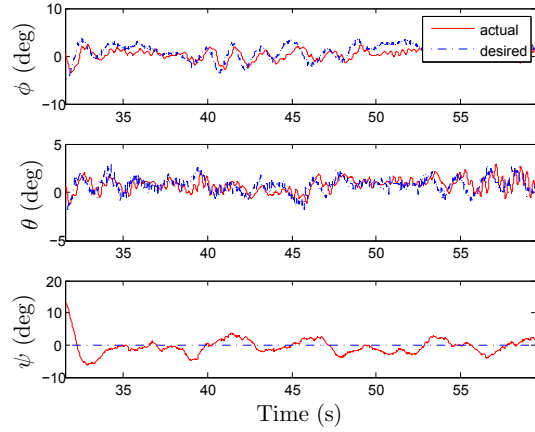

Figure 3.8: Experiment: Trajectories of ϕ, θ, and ψ for hovering.

3.5.2   Case 2: Tracking linear trajectories

The reference trajectory is chosen as a triangle which satisfies the conditions in Corollary 3.5 on each edge. The vertices of the triangle are set to $[0.5, 0.5, -1.2]^T$ m, $[-0.5, 0.5, -1.2]^T$ m and $[-0.5, -0.5, -1.2]^T$ m. The desired velocity is 0.08 m/s. The quadrotor is manually controlled to hover around $[0, 0, -1.2]^T$ m and switched to the proposed tracking controller at $t = 19$ s. After the travelling the triangular path twice, the controller is switched off at $t = 104$ seconds. We use the same controller parameters as in Case 1. The position trajectory of the vehicle in a horizontal plane is given in Figure 3.9. To show the tracking performance more precisely the trajectories of p_1^n and p_2^n versus time are given in Figure 3.10. The trajectory of p_3^n is shown in Figure 3.11, and Figure 3.12 gives the Euler angles and the inner-loop references.
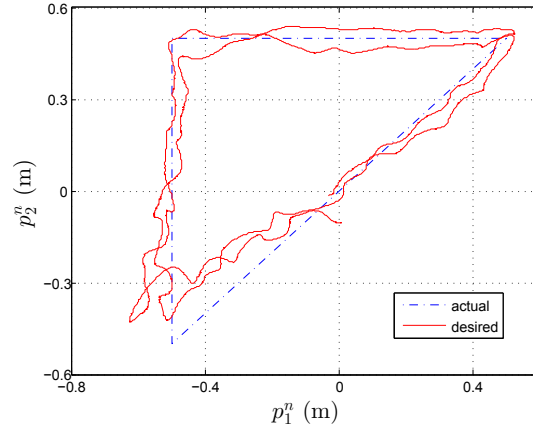
Figure 3.9: Experiment: Position trajectory in the $p_1^n - p_2^n$ plane for tracking.
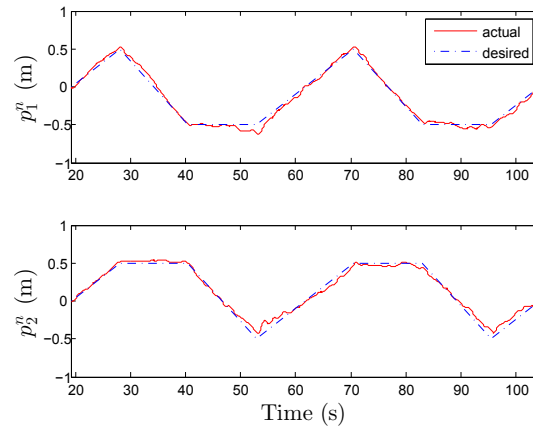
Figure 3.10: Experiment: Position trajectories p_1^n, p_2^n for tracking.
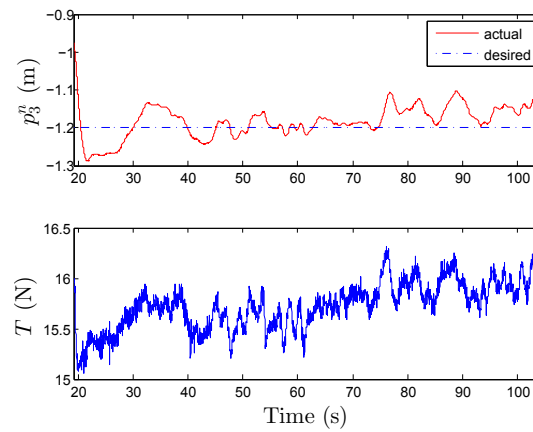
Figure 3.11: Experiment: Trajectories of the height p_3^n and thrust T for tracking.
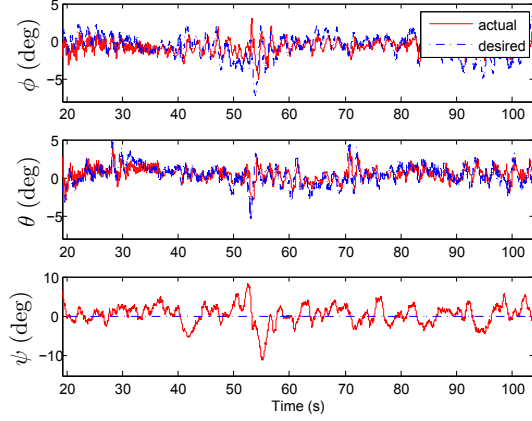
Figure 3.12: Experiment: Trajectories of ϕ, θ, and ψ.

3.6 Conclusion

This chapter develops a novel inner-outer-loop controller with saturated thrust input and bounded roll and pitch. The outer loop consists of a nested saturation controller which is proven to be globally asymptotically stable assuming no inner-loop tracking error. The inner loop is based on a commonly-used PID control. An analysis of the closed-loop stability accounting for inner loop tracking error is provided. The proposed inner-outer loop controller is simulated and implemented on the indoor ANCL quadrotor platform. The robustness of the proposed method is validated for hovering and tracking control objectives.

Chapter 4

Predictor-Based Controller for UAVs with Time Delay

4.1 Introduction

As mentioned in Chapter 2, the ANCL UAV platform consists of a Vicon motion capture systems, which will provide the vehicle's position and velocity information via radio communication. Unavoidable time delay will be introduced in the wireless transmission process. Therefore, it is necessary to consider the effect of time delays while designing a controller. Due to its robustness and ease of tuning, the ANCL UAV platform uses an inner-outer loop control structure with inner loop stabilizing the rotational dynamics and outer loop controlling the translational subsystem. It is straightforward to notice that the time delay from Vicon system only influences the outer loop. Therefore, we categorize this time delay problem as the control problem with input or measurement delay.

There are two main stream for the control of systems with input delays. The first one is called model reduction or prediction and the second is called emulation approach. In this chapter, we will apply the model reduction method by designing a prediction-based controller. This approach uses a dynamic system which estimates the value of the state at a future time. This predicted value can then be used in the control law, effectively compensating the input delay. Examples of this approach are the well-known Smith Predictor, Finite Spectrum Assignment, and the reduction approach [51].

Recently, input-delay control for UAVs have been studied. Work in [96] developed a delayed attitude and height controller using prediction for simplified UAV dynamics. However, the position of the vehicle is not controlled, and the result is local because the nonlinear terms are assumed to be bounded. Work in [97] considered a delayed force input to the outer-loop for a UAV visual servoing problem. The

yaw angle is necessarily to be known for image coordinates reprojection. However, in practice, yaw is not always available. Work in [98] considered time delay terms as disturbances and designed compensating inputs for disturbances.

In this chapter, we propose synchronization-based predictors for a class of systems based on the work in [58, 59]. We also consider inaccurate model parameter and unknown delay measurement, respectively. To improve the robustness of controllers to uncertainties, we modify the predictor proposed in [58, 59] by adding an extra term in the predictor dynamics. We assume the unknown parameter and time delay are both bounded with known bounds. Global asymptotic stability is achieved with the presence of uncertainties. The proposed controllers are applied to translational control of UAVs.

The structure of this chapter is as follows. Section 4.2 gives the review of time delay systems with input delay, including the general representation, three methods of stability analysis and the summary of existing control methods for this problem. In Section 4.3, we derive sufficient conditions for stability for a system in a general form, which includes two different cases by considering known and unknown parameters. In Section 4.4, we consider two input delayed control problems for UAVs, i.e., motion control and visual servoing. These problems can be written in the generalized form considered in Section 4.3. Section 4.5 and 4.6 provide the simulation and experimental results to show the effectiveness of the proposed controller.

4.2 Preliminaries

4.2.1 Introduction to time delay systems

Time delay systems can be described using functional differential equations (FDE) as

$$\dot{x} = f(t, x_t) \tag{4.1}$$

where $x(t) \in \mathbb{R}^n$ and $x_t(\rho) = x(t + \rho)$, $-D \leq \rho \leq 0$. D is the maximum time delay. $f : \mathbb{R} \times \mathcal{C} \to \mathbb{R}^n$, where $\mathcal{C} = \mathcal{C}([-D, 0], \mathbb{R}^n)$ is the set of continuous functions mapping the interval $[-D, 0]$ to $\mathbb{R}^n$. Without loss of generality, we assume $f(t, 0) = 0$, which guarantees that $x = 0$ is the solution of (4.1). The norm on $\varphi \in \mathcal{C}([a, b], \mathbb{R}^n)$ is defined as

$$\|\varphi\|_c = \max_{a \leq \rho \leq b} \|\varphi(\rho)\|$$

Here, the vector norm $\| \cdot \|$ represents the 2-norm. From (4.1), we know that the derivative of the state variable x at time t depends on its past $x(\rho), \rho \in [t - D, t]$.

Thus, to determine the future state, we need the initial state to be a function on the time interval $[-D, 0]$, i.e., $x_{t_0} = \varphi$, $\varphi \in \mathcal{C}$ or $x(t_0 + \rho) = \varphi(\rho)$, where $-D \leq \rho \leq 0$. We will use $x(t, \varphi)$ to represent the solution of (4.1) with initial state φ. Equation (4.1) is called retarded functional differential equations (RFDE). Note that a more general form of time delay systems is of neutral type (NFDE), which is out of scope of interests of this thesis.

First, we define the stability of time delay systems [45, 47, 48].

Definition 4.1 (Stability). For RFDE (4.1), $x(t) = 0$ is said to be stable if for any $t_0 \in \mathbb{R}$ and $\epsilon > 0$, there is a $\delta = \delta(t_0, \epsilon) > 0$ such that $\|x_{t_0}\|_c < \delta$ implies $\|x(t)\| < \epsilon$ for $t \geq t_0$. It is uniformly stable if δ can be chosen independently on t_0.

Definition 4.2 (Asymptotic Stability). For RFDE (4.1), $x(t) = 0$ is said to be asymptotically stable (AS) if it is stable and for any $t_0 \in \mathbb{R}$ and $\epsilon > 0$, there exists a $\delta_a = \delta_a(t_0, \epsilon) > 0$ such that $\|x_{t_0}\|_c < \delta_a$ implies $\lim_{t \to \infty} x(t) = 0$ and $\|x(t)\| < \epsilon$ for $t \geq t_0$. It is uniformly asymptotically stable (UAS) if it is uniformly stable and there exists a $\delta_a > 0$ such that for any $\eta > 0$, there exists a $T = T(\delta_a, \eta)$, then $\|x(t)\| < \eta$ for $\|x_{t_0}\|_c < \delta_a$, $t > t_0 + T$. It is globally (uniformly) asymptotically stable (GAS or GUAS) if it is (uniformly) asymptotically stable and δ_a can be an arbitrarily large, finite number.

Note that, the stability notations are same as systems without delays. For the time-invariant systems $\dot{x} = f(x_t)$, AS is equivalent to UAS.

We also give the definition of exponential stability of time delay systems [47, 99].

Definition 4.3 (Exponential Stability). For RFDE (4.1), $x(t) = 0$ is said to be exponentially stable (ES) if there exists positive real numbers a, b, c such that for any $\varphi \in \mathcal{C}$ and $\|\varphi\|_c < c$, the solution $x(t, \varphi)$ with $x_{t_0} = \varphi$ satisfies

$$\|x(t, \varphi)\| \leq a \exp(-b(t - t_0))\|\varphi\|_c$$

$x(t) = 0$ is said to be globally exponentially stable (GES) if it is exponentially stable and c can be arbitrarily large.

Note that for LTI systems without delays, asymptotic stability also implies exponential stability. However, for LTI systems with delays, it is not always true [47].

4.2.2 Stability analysis methods

There are three categories of stability criteria studied in literature [45–48, 100].

Frequency domain methods

For a LTI time delay system, it is often convenient to use frequency domain methods [45]. These methods will give the sufficient and necessary result. For a RFDE, there are infinite number of roots of its characteristic equation, however, there is a finite number of roots to the right of any vertical line [47]. We have the following theorem to get the sufficient and necessary condition for stability.

Theorem 4.4. *A RFDE is asymptotically stable if and only if all the roots of its characteristic equation have negative real parts.*

We take a RFDE with a single delay as an example. Suppose the characteristic equation has the following form

$$p(s) = P(s) + Q(s)e^{-Ds}$$

where $P(s) = \sum_{i=0}^{n} p_i s^i$, $Q(s) = \sum_{i=0}^{m} q_i s^i$, $n > m$ and $P(j\omega) \neq 0$. We can locate the roots of $P(s) + Q(s)$ first, and increase the value of D and check if there are roots crossing the imaginary axis using both magnitude and phase equations

$$\begin{cases} |P(j\omega)|^2 - |Q(j\omega)|^2 = 0 \\ \omega D = \arg\left(-\frac{Q(j\omega)}{P(j\omega)}\right) \end{cases} \rightarrow \omega_c, D_c$$

- If ω_c exists and if $\frac{d}{d\omega}\left(|P(j\omega)|^2 - |Q(j\omega)|^2\right)_{\omega=\omega_c} > 0$, it means a root crosses the imaginary axis form left to right, thus, in order to guarantee the stability, we need $D < D_c$, otherwise $D > D_c$.

- If ω_c does not exist and $P(s) + Q(s)$ is stable, we can conclude that no root will cross the imaginary axis with the increase of r, thus the system is stable $\forall D$.

We take the following system as one example

$$\dot{x} = -x(t) + bx(t - D) \tag{4.2}$$

to find the condition on b such that (4.2) is stable for any D.

The characteristic equation of (4.2) is

$$p(s) = s + 1 - be^{-Ds}$$

Firstly, we need (4.2) is stable when $D = 0$, i.e., $b - 1 < 0$. Secondly, we need to make sure there is no solution for the magnitude equation, i.e., $b^2 = 1 + \omega^2, \forall\omega$, which yields $|b| < 1$.

We now consider a special case of (4.2) when $b = -2$, i.e.,

$$\dot{x}(t) = -x(t) - 2x(t - D) \tag{4.3}$$

we have the characteristic equation as $p(s) = s + 1 + 2e^{-Ds}$, then

$$\begin{cases} |j\omega + 1|^2 - 4 = 0 \\ \omega D = arg\left(-\frac{2}{j\omega+1}\right) \end{cases} \rightarrow \begin{cases} \omega = \sqrt{3} \\ D = \frac{2\pi}{3\sqrt{3}} \end{cases}$$

Since $\frac{d}{d\omega}\left(|P(j\omega)|^2 - |Q(j\omega)|^2\right)_{\omega=\sqrt{3}} = 2\sqrt{3} > 0$, thus system (4.3) is stable if $D < \frac{2\pi}{3\sqrt{3}} \approx 1.2092$.

Lyapunov-Krasovskii functional-based methods

For systems without delays, we can apply the Lyapunov stability theory by constructing a Lyapunov function $V(t, x(t))$ to determine the stability. As explained in Section 4.2.1, time delay systems do not only depend on the current state $x(t)$, but also the passed state $x(\rho), \rho \in [t - D, t]$. Hence, it is natural to expect the corresponding Lyapunov function be a functional $V(t, x_t)$ for time delay systems. Therefore, We have the following theorem.

Theorem 4.5 (Lyapunov-Krasovskii Theorem). *Suppose* $f : \mathbb{R} \times \mathcal{C} \rightarrow \mathbb{R}^n$ *maps* $\mathbb{R} \times$ (*bounded sets in* $\mathcal{C}$) *into bounded sets of* $\mathbb{R}^n$ *and that* $\alpha, \beta, \gamma : \mathbb{R}^+ \rightarrow \mathbb{R}^+$ *are continuous nondecreasing functions,* $\alpha(0) = \beta(0) = 0$ *and* $\alpha(s), \beta(s)$ *for* $s > 0$*. The solution of RFDE* (4.1) *is uniformly stable if there exists a continuous functional* $V : \mathbb{R} \times \mathcal{C} \rightarrow \mathbb{R}^+$ *such that*

1) $\alpha(\|\varphi(0)\|) \leq V(t, \varphi) \leq \beta(\|\varphi\|_c)$*;*

2) $\dot{V}(t, \varphi) \leq -\gamma(\|\varphi(0)\|)$*;*

If $\gamma(s) > 0$ *for* $s > 0$*, then the solution is uniformly asymptotically stable. If additionally*

3) $\lim_{s\to\infty} \alpha(s) = \infty$*;*

then it is globally uniformly asymptotically stable.

Similarly, we can obtain the following theorem to show exponential stability.

Theorem 4.6. *If there exists a continuous functional* $V : \mathbb{R} \times \mathcal{C} \rightarrow \mathbb{R}^+$ *such that conditions 1) and 3) in Theorem 4.5 are satisfied, and*

$$\dot{V} + 2\sigma V \leq 0$$

then the solution of RFDE (4.1) *is globally exponentially stable with a decay rate* σ*.*

Razumikhin theorem-based methods

Instead of functionals, Razumikhin proposed to use only functions for stability analysis. The derivative of the function $V(t, x(t))$ is not required to be negative all the time, because when

$$V(t, x(t)) < \max_{\rho \in [-D, 0]} (t + \rho, x(t + \rho))$$

$V(t, x(t))$ is not increasing.

Theorem 4.7 (Razumikhin Theorem). *Suppose $f : \mathbb{R} \times \mathcal{C} \to \mathbb{R}^n$ maps $\mathbb{R} \times$ (bounded sets of $\mathcal{C}$) into a bounded set of $\mathbb{R}^n$, and $\alpha, \beta, \gamma : \mathbb{R}^+ \to \mathbb{R}^+$ are continuous nondecreasing functions. $\alpha(s), \beta(s) > 0, \forall s > 0$ and $\alpha(0) = \beta(0)$ and $\beta(s)$ is strictly increasing. If there exists a continuous function $V : \mathbb{R} \times \mathbb{R}^n \to \mathbb{R}$ such that*

1) $\alpha(\|x\|) \leq V(t, x) \leq \beta(\|x\|), \ \forall t \in \mathbb{R}, x \in \mathbb{R}^n$;

2) $\dot{V}(t, x(t)) \leq -\gamma(\|x(t)\|)$, whenever $V(t + \rho, x(t + \rho)) \leq V(t, x(t)), \ \forall \rho \in [-D, 0]$;

then, the solution $x = 0$ of RFDE (4.1) is uniformly stable. If $\gamma(s) > 0, \forall s > 0$, and there is a continuous nondecreasing function $p(s) > s, \forall s > 0$, such that

3) $\dot{V}(t, x(t)) \leq -\gamma(\|x(t)\|)$, whenever $V(t + \rho, x(t + \rho)) \leq p(V(t, x(t))), \ \forall \rho \in [-D, 0]$;

then it is uniformly asymptotically stable. If

4) $\lim_{s \to \infty} \alpha(s) = \infty$;

it is globally uniformly asymptotically stable.

Examples

For a LTI system with a constant time delay D

$$\dot{x}(t) = Ax(t) + Bx(t - D) \tag{4.4}$$

We consider a Lyapunov-Krasovskii functional (LKF)

$$V(x_t) = x^T(t)Px(t) + \int_{t-D}^{t} x^T(\xi)Sx(\xi)d\xi$$

where $P, S \in \mathbb{R}^n$ are positive definite. Apparently,

$$\lambda_{min}(P)\|x(t)\|^2 \leq V(x_t) \leq \lambda_{max}(P + DS)\|x_t\|_c^2$$

then

$$\dot{V} = \frac{dV(x_t)}{dt}$$
$$= 2x^T(t)P(Ax(t) + Bx(t-D)) + x^T(t)Sx(t) - x^T(t-D)Sx(t-D)$$
$$= \begin{bmatrix} x^T(t) & x^T(t-D) \end{bmatrix} \begin{bmatrix} PA + A^TP + S & PB \\ B^TP & -S \end{bmatrix} \begin{bmatrix} x(t) \\ x(t-D) \end{bmatrix}$$

Thus, based on Theorem 4.5 if

$$\begin{bmatrix} PA + A^TP + S & PB \\ B^TP & -S \end{bmatrix} < 0$$

system (4.4) is stable $\forall D \in \mathbb{R}^+$.

We now use Razumikhin theorem to solve the same problem. Consider a Lyapunov function $V(x) = x^TPx$, where $P > 0$, then we have

$$\dot{V} = 2x^T(t)P[Ax(t) + Bx(t-D)]$$

For any $p > 1$ and $V(x(t+\rho)) < pV(x(t)), \forall -D \leq \rho \leq 0$, we have

$$\dot{V} \leq 2x^T(t)P[Ax(t) + Bx(t-D)] + \alpha[px^T(t)Px(t) - x^T(t-D)Px(t-D)]$$
$$= \begin{bmatrix} x^T(t) & x^T(t-D) \end{bmatrix} \begin{bmatrix} PA + A^TP + \alpha pP & PB \\ B^TP & -\alpha P \end{bmatrix} \begin{bmatrix} x(t) \\ x(t-D) \end{bmatrix}$$

Based on Theorem 4.7, we know if

$$\begin{bmatrix} PA + A^TP + \alpha P & PB \\ B^TP & -\alpha P \end{bmatrix} < 0$$

the system is stable.

4.2.3 Control of time delay systems

This subsection discusses the control problems of systems with input delays [49, 50]. There are two main categories. The first one is called emulation approach, which designs a stabilizing controller without delays, and analyze the effect of delays on the closed-loop stability. The second one is called model reduction or prediction, which compensates delays by augmenting the system with a new state.

Emulation approach

This method deals with the stabilization first by assuming the delay to be 0, and then study the effects of time delay on the closed-loop stability. Constraints on the

size of the delay will be imposed to guarantee the stability. Generally, we will find an upper bound of the delay $\bar{D}$ such that for all $D < \bar{D}$, the time delay system is still stable.

The work in [60] studied the saturated control with time delay for a chain of integrators

$$\dot{x}_i(t) = x_{i+1}(t), \quad i = 1, \cdots, n-1$$
$$\dot{x}_n(t) = u(t - D)$$

Teel's nested saturation controller [33] will globally stabilize the system if

$$D \le \bar{D} = \min\left\{\frac{M_1}{8(nM_1 + \sum_{j=2}^n \frac{M_j}{2})}, \frac{1}{9}\right\}$$

where M_i is the upper bound of the ith saturation function σ_i, i.e., $\sigma_i(s) = s$ when $|s| < M_i$, and $\sigma_i(s) = M_i$ when $s > M_i$, $\sigma(s) = -M_i$ when $s < -M_i$.

Predictor based control

Control of delayed systems based on predictor is popular due to its application to large delays. For a LTI system with a single constant time delay

$$\dot{x}(t) = Ax(t) + Bu(t - D) \tag{4.5}$$

Assume there is a stabilizing gain vector for the system (4.5) without delay, i.e., $A + BK$ is Hurwitz. If we choose the control as

$$u(t - D) = Kx(t) \tag{4.6}$$

then, the closed-loop will be stable. The control can be rewritten as

$$u(t) = Kx(t + D)$$

On the other hand, we have

$$x(t + D) = e^{AD}x(t) + \int_{t-D}^t e^{A(t-\rho)}Bu(\rho)d\rho, \quad \forall t \ge 0$$

Thus, we have the following feedback controller

$$u(t) = K\left[e^{AD}x(t) + \int_{t-D}^t e^{A(t-\rho)}Bu(\rho)d\rho\right], \quad \forall t \ge 0 \tag{4.7}$$

Alternatively, we can introduce the predictor state z as $z(t) = x(t + D)$, then

we have $\dot{z}(t) = Az(t) + Bu(t)$. Therefore, (4.7) can be simply written as

$$u(t) = Kz(t)$$

Alternatively, (4.5) can be written using a first-order hyperbolic PDE or "transport PDE"

$$\dot{x}(t) = Ax(t) + BU(0,t)$$
$$U_t(\chi, t) = U_\chi(\chi, t)$$
$$U(D, t) = u(t)$$

The stability can be proven based on the PDE model [49].

The work in [58, 101] proposed a method of prediction based on synchronization. We consider the same LTI time delay system as in (4.5)

$$\dot{x}(t) = Ax(t) + Bu(t - D) \tag{4.8}$$

and design the predictor system as

$$\dot{z}(t) = Az(t) + Bu(t) + K_e(z(t - D) - x(t)) \tag{4.9}$$

where K_e will be determined. The controller is chosen as $u(t) = Kz(t)$ where K is a stabilizing control gain as in (4.6). By defining $e(t) = z(t - D) - x(t)$, we have

$$\dot{e}(t) = Ae(t) + K_e e(t - D) \tag{4.10}$$

Based on the Lyapunov-Krasovskii theorem (Theorem 4.5), we can obtain a sufficient condition of stability for the error dynamics (4.10) on K_e and D in terms of a LMI.

We consider the following Lyapunov functional

$$V = e^T e + \int_{-D}^{0} \int_{t+\rho}^{t} e^T(\delta) e(\delta) d\delta d\rho + \int_{-2D}^{-D} \int_{t+\rho}^{t} e^T(\delta) K_e^T K_e e(\delta) d\delta d\rho$$

then, $\dot{V} < 0$ if

$$\begin{bmatrix} (A + K_e)^T + (A + K_e) & K_e A & K_e & I & K_e^T \\ & D^{-1}I & 0 & 0 & 0 \\ & & -D^{-1}I & 0 & 0 \\ & & & D^{-1}I & 0 \\ & & & & -D^{-1}I \end{bmatrix} < 0$$

63

We rewrite (4.8) as

$$\dot{x}(t) = (A + BK)x(t) + BKe(t)$$

Apparently, x-subsystem can be seen as a stable LTI system disturbed by a stabilizing state e. The stability of x can be obtained based on the cascade theory (Theorem 4.7 in [102]) since the interconnection term satisfies the linear growth condition.

The synchronization-based predictor encourages the convergence of the delayed state of the system and the delayed predicted state by a correction term. This enables the predictor-controller combination to exhibit certain robustness [59]. For this reason, we will extend this synchronization-based predictor to a class of time delay systems and apply these predictors to UAV dynamics for both motion control and visual servoing problems.

4.3 Prediction-based controller design

Consider a class of systems of the following form

$$\dot{x} = \chi(t)A_0 x + \lambda A_1 x + Bu \tag{4.11}$$

where $x \in \mathbb{R}^n$ is the state, $u \in \mathbb{R}^m$ is the control input, $A_0, A_1 \in \mathbb{R}^{n \times n}$, $B \in \mathbb{R}^{n \times m}$ and $A_0^T = -A_0$. $\chi(t)$ is a bounded time-varying parameter, λ is a known positive constant. We also assume a stabilizing controller for (4.11) exists.

Assumption 4.8. Suppose there exists a state feedback controller $u = u(x)$ such that the closed loop of for (4.11) is GAS.

For example, we can find a linear controller, i.e.,

$$u(x) = Kx \tag{4.12}$$

where $K \in \mathbb{R}^{m \times n}$, if there exists a positive definite matrix $Q \in \mathbb{R}^{n \times n}$ such that $(\lambda A_1 + BK)^T + (\lambda A_1 + BK) = -Q$.

Now, we consider a constant delay in the input channel and assume the delay is caused by measurement, then the closed-loop of (4.11) becomes

$$\dot{x} = \chi(t)A_0 x + \lambda A_1 x + Bu(x(t - D)) \tag{4.13}$$

where D is the constant known delay. Because of the presence of the delay, the stability of (4.13) is not guaranteed. Based on the work in [58], we propose a synchronization-based predictor as described in Section 4.2.3

$$\dot{z} = \chi(t)A_0 z + \lambda A_1 z + Bu(z) + K_e(z_D - x_D) \tag{4.14a}$$

where $z \in \mathbb{R}^n$ is the prediction state, $z_D = z(t-D)$, $x_D = x(t-D)$ and $K_e \in \mathbb{R}^{n \times n}$ is to be determined. Note that even though the subscripts of states are often labelled as t for the delayed states as in Section 4.2.1, here we use D instead to explicitly show the value of time delay without causing any confusion.

Instead of the delayed measurement $x(t-D)$, the prediction state z will be used in the controller. Then, (4.13) becomes

$$\dot{x} = \chi(t)A_0 x + \lambda A_1 x + Bu(z) \tag{4.14b}$$

We will design a K_e, such that (4.14a) and (4.14b) are stable for a range of D. Sufficient conditions on K_e and D will be derived. First, we define $e = z - x$ and then we have

$$\dot{e} = \chi(t)A_0 e + \lambda A_1 e + K_e e_D \tag{4.15}$$

where $e_D = e(t-D)$. Then, we obtain

$$
\begin{aligned}
e(t-D) &= e(t) - \int_{t-D}^{t} \dot{e}(\rho)d\rho \\
&= e(t) - \int_{t-D}^{t} \left[\chi(\rho)A_0 e(\rho) + \lambda A_1 e(\rho) + K_e e(\rho-D) \right] d\rho \tag{4.16}
\end{aligned}
$$

Substituting (4.16) into (4.15) yields

$$\dot{e} = \Xi_e \tag{4.17}$$

where

$$\Xi_e = \chi(t)A_0 e + (\lambda A_1 + K_e)e - K_e \int_{t-D}^{t} \left[\chi(\rho)A_0 e(\rho) + \lambda A_1 e(\rho) + K_e e(\rho-D) \right] d\rho$$

Consider a Lyapunov-Krasovskii functional

$$V_e = e^T e + \int_{-D}^{0} \int_{t+\rho}^{t} e^T(\delta)S_1 e(\delta)d\delta d\rho + \int_{-2D}^{-D} \int_{t+\rho}^{t} e^T(\delta)S_2 e(\delta)d\delta d\rho \tag{4.18}$$

where $0 < S_1, S_2 \in \mathbb{R}^n$ are to be determined. Then the derivative of V_e along (4.17) is

$$
\begin{aligned}
\dot{V}_e =& e^T \dot{e} + \dot{e}^T e + \int_{-D}^{0} \left[e^T(t)S_1 e(t) - e^T(t+\rho)S_1 e(t+\rho) \right] d\rho \\
&+ \int_{-2D}^{-D} \left[e^T(t)S_2 e(t) - e^T(t+\rho)S_2 e(t+\rho) \right] d\rho
\end{aligned}
$$

$$=e^T \left[(\lambda A_1 + K_e)^T + (\lambda A_1 + K_e) \right] e$$

$$- 2e^T K_e \int_{t-D}^t \left[\chi(\rho) A_0 e(\rho) + \lambda A_1 e(\rho) + K_e e(\rho - D) \right] d\rho$$

$$+ \int_{-D}^0 \left[e^T(t) S_1 e(t) - e^T(t+\rho) S_1 e(t+\rho) \right] d\rho$$

$$+ \int_{-2D}^{-D} \left[e^T(t) S_2 e(t) - e^T(t+\rho) S_2 e(t+\rho) \right] d\rho$$

Note that $e^T \chi(t) A_0 e = 0$ because $A_0^T = -A_0$. Since

$$-2e^T K_e \int_{t-D}^t \chi(\rho) A_0 e(\rho) d\rho \le \int_{t-D}^t |\chi(\rho)| \left[e^T K_e A_0 \Gamma_1^{-1} A_0^T K_e^T e + e^T(\rho) \Gamma_1 e(\rho) \right] d\rho$$

$$\le \epsilon D e^T K_e A_0 \Gamma_1^{-1} A_0^T K_e^T e + \int_{t-D}^t |\chi(\rho)| e^T(\rho) \Gamma_1 e(\rho) d\rho$$

$$-2e^T K_e \int_{t-D}^t \lambda A_1 e(\rho) d\rho \le \lambda D e^T K_e A_1 \Gamma_2^{-1} A_1^T K_e^T e + \int_{t-D}^t \lambda e^T(\rho) \Gamma_2 e(\rho) d\rho$$

$$-2e^T K_e \int_{t-D}^t K_e e(\rho - D) d\rho \le D e^T K_e \Gamma_3^{-1} K_e^T e$$

$$+ \int_{t-D}^t e^T(\rho - D) K_e^T \Gamma_3 K_e e(\rho - D) d\rho$$

where $\epsilon = \sup_t |\chi(t)|$ and $0 < \Gamma_1, \Gamma_2, \Gamma_3 \in \mathbb{R}^n$, if we choose S_1, S_2 as

$$S_1 = \epsilon \Gamma_1 + \lambda \Gamma_2$$
$$S_2 = K_e^T \Gamma_3 K_e$$

then we obtain $\dot{V}_e \le \Xi_{V_e}$, where

$$\Xi_{V_e} = e^T \left[(\lambda A_1 + K_e)^T + (\lambda A_1 + K_e) \right] e + \epsilon D e^T K_e A_0 \Gamma_1^{-1} A_0^T K_e^T e$$

$$+ \lambda D e^T K_e A_1 \Gamma_2^{-1} A_1^T K_e^T e + D e^T K_e \Gamma_3^{-1} K_e^T e + D e^T (S_1 + S_2) e$$

We choose $\Gamma_i = I_n, i = 1, 2, 3$, where I_n is the identity matrix with rank n, then the sufficient condition for $\dot{V}_e < 0$ can be expressed using the following LMI

$$\begin{bmatrix} F_{11} & \epsilon^{\frac{1}{2}} K_e A_0 & K_e A_1 & K_e & I_n & K_e^T \\ & -D' I_n & 0 & 0 & 0 & 0 \\ & & -\frac{D'}{\lambda} I_n & 0 & 0 & 0 \\ & & & -D' I_n & 0 & 0 \\ & & & & -\frac{D'}{(\epsilon + \lambda)} I_n & 0 \\ & & & & & -D' I_n \end{bmatrix} < 0 \qquad (4.19)$$

where $F_{11} = (\lambda A_1 + K_e)^T + (\lambda A_1 + K_e)$ and $D' = D^{-1}$. We can find the minimum

of D', i.e., the maximum tolerable delay D_{max} such that LMI (4.19) holds using Matlab LMI functions for given parameters. The resulting K_e is used in the predictor dynamics (4.14a).

Based on the above analysis, we can conclude the following theorem.

Theorem 4.9. *The error dynamics (4.15) is GAS and GES if LMI (4.19) is satisfied.*

Proof. From (4.18), we know that

$$\|e\|^2 \leq V_e \leq (1 + \frac{D^2}{2}\|S_1\| + \frac{3D^2}{2}\|S_2\|)\|e_t\|_c^2$$

and if LMI (4.19) is satisfied, $\dot{V}_e < 0$. According to Theorem 4.5, we know the error dynamics (4.15) is GAS.

Now, we start to prove GES by choosing a slightly different LKF compared to (4.18)

$$\bar{V}_e = e^T e + \int_{-D}^{0} \int_{t+\rho}^{t} \exp(-2\sigma(t-\delta))e^T(\delta)\bar{S}_1 e(\delta)d\delta d\rho$$
$$+ \int_{-2D}^{-D} \int_{t+\rho}^{t} \exp(-2\sigma(t-\delta))e^T(\delta)\bar{S}_2 e(\delta)d\delta d\rho$$

where $\sigma > 0$ and $\bar{S}_1 = S_1 \exp(2\sigma D)$, $\bar{S}_2 = S_2 \exp(4\sigma D)$. We have

$$\dot{\bar{V}}_e + 2\sigma\bar{V}_e$$
$$= 2e^T\dot{e} + \int_{-D}^{0} e^T(t)\bar{S}_1 e(t)d\rho - \int_{-D}^{0} \exp(2\sigma(D+\rho))e^T(t+\rho)S_1 e(t+\rho)d\rho$$
$$+ \int_{-2D}^{-D} e^T(t)\bar{S}_2 e(t)d\rho - \int_{-2D}^{-D} \exp(2\sigma(2D+\rho))e^T(t+\rho)S_2 e(t+\rho)d\rho$$
$$- 2\sigma \int_{-D}^{0} \int_{t+\rho}^{t} \exp(-2\sigma(t-\delta))e^T(\delta)\bar{S}_1 e(\delta)d\delta d\rho$$
$$- 2\sigma \int_{-2D}^{-D} \int_{t+\rho}^{t} \exp(-2\sigma(t-\delta))e^T(\delta)\bar{S}_2 e(\delta)d\delta d\rho$$
$$+ 2\sigma e^T e + 2\sigma \int_{-D}^{0} \int_{t+\rho}^{t} \exp(-2\sigma(t-\delta))e^T(\delta)\bar{S}_1 e(\delta)d\delta d\rho$$
$$+ 2\sigma \int_{-2D}^{-D} \int_{t+\rho}^{t} \exp(-2\sigma(t-\delta))e^T(\delta)\bar{S}_2 e(\delta)d\delta d\rho$$
$$\leq 2e^T\dot{e} + 2\sigma e^T e + De^T\bar{S}_1 e - \int_{-D}^{0} e^T(t+\rho)S_1 e(t+\rho)d\rho$$
$$+ De^T\bar{S}_2 e - \int_{-2D}^{-D} e^T(t+\rho)S_2 e(t+\rho)d\rho$$
$$\leq \Xi_{V_e}(e, K_e) + 2\sigma e^T e + D(\exp(2\sigma D)-1)e^T S_1 e + D(\exp(4\sigma D)-1)e^T S_2 e$$

67

if (4.19) is satisfied, we know that $\Xi_{V_e}(e, K_e) < 0$. Therefore, there exists a $\sigma > 0$ such that $\dot{\bar{V}}_e + 2\sigma \bar{V}_e \le 0$. Therefore, based on Theorem 4.6 we can conclude that (4.15) is GES. $\qquad\square$

The following theorem [103] will be used for the stability analysis of delayed cascade system.

Theorem 4.10. *Consider the mappings* $f_1, f_2 : \mathbb{R} \times \mathcal{C} \to \mathbb{R}^n$, $g : \mathbb{R} \times \mathcal{C} \times \mathcal{C} \to \mathbb{R}^n$ *and* $f_1(t, 0) = f_2(t, 0) = g(t, \varphi, 0) = 0, \forall \varphi \in \mathcal{C}$. *The solution* $(x, y) = 0$ *of the cascade system with time delay*

$$\dot{x} = f_1(t, x_t) + g(t, x_t, y_t) \tag{4.20a}$$

$$\dot{y} = f_2(t, y_t) \tag{4.20b}$$

is GAS if

1) *systems (4.20b) and* $\dot{x} = f_1(t, x_t)$ *are GAS;*

2) *solutions of system (4.20a) are bounded.*

Theorem 4.11. *System (4.11) with predictor (4.14a) is GAS if LMI (4.19) is satisfied.*

Proof. Since the error dynamics (4.15) is GES from Theorem 4.9, we have

$$\|e_D\| \le a \exp(-bt)\|\varphi\|_c, \quad a, b > 0, \varphi \in \mathcal{C}$$

For a Lyapunov function $V_z = z^T z$, we have

$$\dot{V}_z = -z^T Q z + 2z^T K_e e_D$$

For any $\|z\| > 2a \exp(bD)\|K_e\|\|\varphi\|_c/\lambda_{\min}(Q)$, $\dot{V}_z < 0$. Therefore, z is bounded and we can conclude that the predictor (4.14a) is GAS from Theorem 4.10. Since $e = z - x$, x of (4.11) is also GAS. $\qquad\square$

Remark 4.12. Comparing the predictor dynamics in [58] and (4.14a), we notice the correction terms are different. This is because work in [58] considered input delay, while we consider measurement delay. Figure 4.1 illustrates the difference between the two types of delay. For input delay the current state $x(t)$ is available and fed back to the controller. The prediction state z_D is designed to estimate the state $x(t)$, thus the correction term in the predictor dynamics is taken as $z_D - x(t)$. However, in (4.14a), since the delay appears in the measurement, only the delayed state x_D is available at time t. Therefore, we use z_D to estimate x_D. Hence, the correction term in the proposed predictor is therefore $z_D - x_D$.
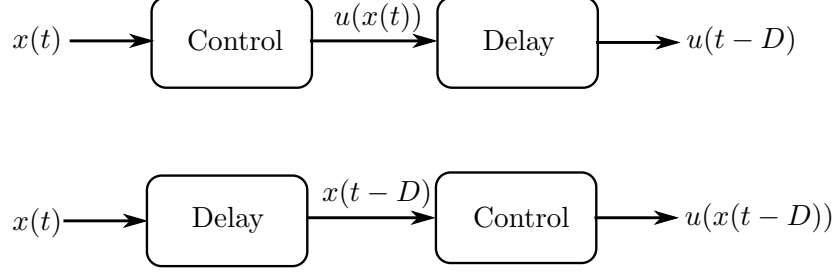
Figure 4.1: Difference between input delay and measurement delay.

Remark 4.13. The bound ϵ is not necessarily to be small. From Assumption 4.8, we know that $\exists K_e$ such that $F_{11} < -\epsilon I$. Thus, there exists a D such that $\epsilon D K_e A_0 \Gamma_1^{-1} A_0^T K_e^T + D\lambda K_e A_1 \Gamma_2^{-1} A_1^T K_e^T + D K_e \Gamma_3^{-1} K_e^T + D(\epsilon I + \lambda I + K_e^T K_e) < \epsilon I$. A large ϵ will result in a small D.

Alternatively, we can modify the controller u in (4.14a) and (4.14b) as

$$\tilde{u}(z) = u(z) - \tilde{K}_e e_D$$

where $\tilde{K}_e \in \mathbb{R}^{m \times n}$, then we design the predictor as

$$\dot{z} = \chi(t) A_0 z + \lambda A_1 z + B\tilde{u}(z) + K_e(z_D - x_D)$$

which is equivalent to

$$\dot{z} = \chi(t) A_0 z + \lambda A_1 z + Bu(z) \tag{4.21}$$

where $K_e = B\tilde{K}_e$. From Assumption 4.8, we know that the predictor dynamics (4.21) is GAS. Then, the error dynamics will be

$$\dot{e} = \chi(t) A_0 e + \lambda A_1 e + \tilde{K}_e e_D \tag{4.22}$$

Therefore, the error dynamics (4.22) has the same form as (4.15) and the conditions for GAS are given in Theorem 4.9. Hence, the proof of closed-loop stability with the predictor (4.21) can be simplified, because Theorem 4.9 and 4.10 are not required. Moreover, the stability of the predictor dynamics can be used to improve the robustness with respect to uncertainties, which will be shown in Subsection 4.3.1 and 4.3.2.

4.3.1 When λ is unknown

In this subsection, we consider the case when the model parameter λ in (4.11) is unknown. We assume the upper and lower bound of λ are given.

Assumption 4.14. Assume the bounds on λ are known, i.e.,

$$\underline{\lambda} \leq \lambda \leq \bar{\lambda}$$

where $\underline{\lambda}, \bar{\lambda} > 0$.

Since λ is unknown, we need to make a small change to Assumption 4.8.

Assumption 4.15. Suppose there exists a stabilizing controller of (4.11) $u = u_1(x)$ such that for Lyapunov function $V_u(x) = x^T x$,

$$\dot{V}_u(x) \leq -x^T Q_1 x, \quad \forall \lambda \in [\underline{\lambda}, \bar{\lambda}]$$

where $Q_1 > 0$.

In this case, we can choose $u_1(x) = K_1 x$ such that

$$(\lambda^* A_1 + K_1) + (\lambda^* A_1 + K_1)^T = -Q_1^*$$
$$Q_1^* - \Delta\lambda(A_1 + A_1^T) > 0$$

and choose $Q_1 = Q_1^* - \Delta\lambda(A_1 + A_1^T)$, where $\lambda^* = \frac{1}{2}(\underline{\lambda} + \bar{\lambda})$, $\Delta\lambda = \bar{\lambda} - \lambda^*$.

We design a predictor as

$$\dot{z}_1 = \chi(t)A_0 z_1 + \hat{\lambda}A_1 z_1 + B\tilde{u}_1(z_1) + B\tilde{K}_e(z_{1D} - x_D) \tag{4.23}$$

where $z_{1D} = z_1(t - D)$, $\hat{\lambda}$ is a constant estimate of λ and $\tilde{K}_e \in \mathbb{R}^{m \times n}$ is to be determined. Hence, (4.11) becomes

$$\dot{x} = \chi(t)A_0 x + \lambda A_1 x + B\tilde{u}_1(z_1) \tag{4.24}$$

where

$$\tilde{u}_1(z_1) = u_1(z_1) - \tilde{K}_e(z_{1D} - x_D) \tag{4.25}$$

By defining $e_1 = z_1 - x$, we have

$$\dot{e}_1 = \chi(t)A_0 e_1 + \lambda A_1 e_1 + B\tilde{K}_e e_{1D} + \tilde{\lambda}A_1 z_1 \tag{4.26}$$

where $e_{1D} = e_1(t - D)$, $\tilde{\lambda} = \hat{\lambda} - \lambda \leq 2\Delta\lambda$. If we choose $\hat{\lambda} = \lambda^*$, we can guarantee $|\tilde{\lambda}| \leq \Delta\lambda$. Furthermore, we obtain

$$e_1(t - D) = e_1 - \int_{t-D}^{t} \dot{e}_1(\rho)d\rho$$

70

$$= e_1(t) - \int_{t-D}^{t} \left[\chi(\rho)A_0 e_1(\rho) + \lambda A_1 e_1(\rho) + B\tilde{K}_e e_{1D}(\rho) + \tilde{\lambda} A_1 z_1(\rho) \right] d\rho \quad (4.27)$$

Substituting (4.27) into (4.26), we have

$$
\begin{aligned}
\dot{e}_1 =& \chi(t)A_0 e_1 + (\lambda A_1 + B\tilde{K}_e)e_1 + \tilde{\lambda} A_1 z_1 \\
& - B\tilde{K}_e \int_{t-D}^{t} \left[\lambda A_1 e_1(\rho) + \chi(\rho)A_0 e_1(\rho) + B\tilde{K}_e e_{1D}(\rho) + \tilde{\lambda} A_1 z_1(\rho) \right] d\rho \\
=& \Xi_{e_1} + \tilde{\lambda} A_1 z_1 - B\tilde{K}_e \int_{t-D}^{t} \tilde{\lambda} A_1 z_1(\rho) d\rho \quad (4.28)
\end{aligned}
$$

where Ξ_{e_1} is obtained by replacing e and K_e in Ξ_e by e_1 and $B\tilde{K}_e$. We define a LKF V_{e_1} by replacing e and K_E in V_e (4.18) by e_1 and $B\tilde{K}_e$, and then we have

$$\dot{V}_{e_1} \leq \Xi_{V_e} + 2\tilde{\lambda} e_1^T A_1 z_1 - 2e_1^T B\tilde{K}_e \int_{t-D}^{t} \tilde{\lambda} A_1 z_1(\rho) d\rho$$

Since

$$
\begin{aligned}
-2e_1^T B\tilde{K}_e \int_{t-D}^{t} \tilde{\lambda} A_1 z_1(\rho) d\rho \leq & \Delta\lambda D e_1^T B\tilde{K}_e \Lambda_1^{-1} \tilde{K}_e^{\ T} B^T e_1 \\
& + \Delta\lambda \int_{t-D}^{t} z_1^T(\rho) A_1^T \Lambda_1 A_1 z_1(\rho) d\rho
\end{aligned}
$$

we can derive that

$$
\begin{aligned}
\dot{V}_{e_1} \leq & \Xi_{V_{e_1}} + 2\tilde{\lambda} e_1^T A_1 z_1 + \Delta\lambda D e_1^T B\tilde{K}_e \Lambda_1^{-1} \tilde{K}_e^{\ T} B^T e_1 \\
& + \Delta\lambda \int_{t-D}^{t} z_1^T(\rho) A_1^T \Lambda_1 A_1 z_1(\rho) d\rho
\end{aligned}
$$

where $\Xi_{V_{e_1}}$ is is obtained by replacing e and K_e in Ξ_{V_e} by e_1 and $B\tilde{K}_e$. We consider the following Lyapunov-Krasovskii functional

$$V_1 = V_{e_1} + \int_{-D}^{0} \int_{t+\rho}^{t} \Delta\lambda z_1^T(\delta) A_1^T \Lambda_1 A_1 z_1(\delta) d\delta d\rho + V_u(z_1)$$

then its derivative becomes

$$
\begin{aligned}
\dot{V}_1 \leq & \Xi_{V_{e_1}} + 2\tilde{\lambda} e_1^T A_1 z_1 + \Delta\lambda D e_1^T B\tilde{K}_e \Lambda_1^{-1} \tilde{K}_e^{\ T} B^T e_1 \\
& + \Delta\lambda \int_{t-D}^{t} z_1^T(\rho) A_1^T \Lambda_1 A_1 z_1(\rho) d\rho + \int_{-D}^{0} \Delta\lambda z_1^T(t) A_1^T \Lambda_1 A_1 z_1(t) d\rho \\
& - \int_{-D}^{0} \Delta\lambda z_1^T(t+\rho) A_1^T \Lambda_1 A_1 z_1(t+\rho) d\rho - z_1^T Q_1 z_1
\end{aligned}
$$

$$\leq e_1^T \left[(\lambda A_1 + B\tilde{K}_e)^T + (\lambda A_1 + B\tilde{K}_e) \right] e_1 + \epsilon De_1^T B\tilde{K}_e A_0 \Gamma_1^{-1} A_0^T \tilde{K}_e^T B^T e_1$$

$$+ \lambda De_1^T B\tilde{K}_e A_1 \Gamma_2^{-1} A_1^T \tilde{K}_e^T B^T e + De^T B\tilde{K}_e \Gamma_3^{-1} \tilde{K}_e^T B^T e_1$$

$$+ De_1^T(\epsilon\Gamma_1 + \lambda\Gamma_2 + \tilde{K}_e^T B^T \Gamma_3 B\tilde{K}_e)e_1 + \Delta\lambda De_1^T B\tilde{K}_e \Lambda_1^{-1} \tilde{K}_e^T B^T e_1 + \Delta\lambda e_1^T e_1$$

$$+ \Delta\lambda z_1^T A_1^T A_1 z_1 + \Delta\lambda Dz_1^T A_1^T \Lambda_1 A_1 z_1 - z_1^T Q_1 z_1$$

$$\leq e_1^T \left[(\underline{\lambda} A_1 + B\tilde{K}_e)^T + (\underline{\lambda} A_1 + B\tilde{K}_e) \right] e_1 + \epsilon De_1^T B\tilde{K}_e A_0 \Gamma_1^{-1} A_0^T \tilde{K}_e^T B^T e_1$$

$$+ \bar{\lambda} De_1^T B\tilde{K}_e A_1 \Gamma_2^{-1} A_1^T \tilde{K}_e^T B^T e_1 + De_1^T B\tilde{K}_e \Gamma_3^{-1} \tilde{K}_e^T B^T e_1$$

$$+ De_1^T(\epsilon\Gamma_1 + \bar{\lambda}\Gamma_2 + \tilde{K}_e^T B^T \Gamma_3 B\tilde{K}_e)e_1 + \Delta\lambda De_1^T B\tilde{K}_e \Lambda_1^{-1} \tilde{K}_e^T B^T e_1 + \Delta\lambda e_1^T e_1$$

$$+ \Delta\lambda z_1^T A_1^T A_1 z_1 + \Delta\lambda Dz_1^T A_1^T \Lambda_1 A_1 z_1 - z_1^T Q_1 z_1$$

$$+ 4\max\{\lambda_{\max}(A_1), 0\}\Delta\lambda e_1^T e_1$$

where $\lambda_{\max}(A_1)$ is the maximum eigenvalue of A_1.

We choose Λ_1 and Γ_i as the identity matrix, then the sufficient condition for $\dot{V}_1 < 0$ can be expressed using the following LMIs

$$G < 0 \tag{4.29a}$$

$$H < 0 \tag{4.29b}$$

where

$$G = \begin{bmatrix} G_{11} & \epsilon^{\frac{1}{2}}B\tilde{K}_e A_0 & B\tilde{K}_e & K_e^T B^T & B\tilde{K}_e A_1 & I_n \\ & -D'I_n & 0 & 0 & 0 & 0 \\ & & -D'/(1+\Delta\lambda)I_n & 0 & 0 & 0 \\ & & & -D'I_n & 0 & 0 \\ & & & & -D'/\bar{\lambda}I_n & 0 \\ & & & & & -D'/(\epsilon+\bar{\lambda})I_n \end{bmatrix}$$

$$H = \begin{bmatrix} -Q_1 & A_1^T & A_1^T \\ & -1/\Delta\lambda I_n & 0 \\ & & -D'/\Delta\lambda I_n \end{bmatrix}$$

and $G_{11} = (\underline{\lambda} A_1 + B\tilde{K}_e)^T + (\underline{\lambda} A_1 + B\tilde{K}_e) + 4\max\{\lambda_{\max}(A_1), 0\}\Delta\lambda I_n + \Delta\lambda I_n$.

The stability analysis of system (4.11) with predictor (4.23) and controller (4.25) is more straightforward, since (4.23) with controller $\tilde{u}_1$ becomes

$$\dot{z}_1 = \chi(t)A_0 z_1 + \hat{\lambda} A_1 z_1 + Bu_1(z_1)$$

which is already GAS. Thus, we have the following theorem.

Theorem 4.16. *System* (4.11) *with predictor* (4.23) *and controller* (4.25) *is GAS if LMIs* (4.29) *are satisfied.*

4.3.2 Input delay is unknown

In this subsection, we consider the case when there is uncertainty in the delay. We assume the delay is an unknown constant such that $D \in [\underline{D}, \bar{D}]$, where $\underline{D}, \bar{D}$ are both known and define $D_0 = \frac{1}{2}(\underline{D} + \bar{D})$ and $\Delta D = \frac{1}{2}(\bar{D} - \underline{D})$.

Since D is unknown, we cannot get the access to the prediction state at the time $t = D$ in (4.14a). We use D_0 as an estimate of D, thus, we rewrite (4.14a) as

$$\dot{z}_2 = \chi(t)A_0 z_2 + \lambda A_1 z_2 + B\tilde{u}_2(z_2) + B\tilde{K}_e(z_{2D_0} - x_D) \tag{4.30}$$

We consider a linear control, i.e.,

$$\tilde{u}_2(z_2) = K z_2 - \tilde{K}_e(z_{2D_0} - x_D) \tag{4.31}$$

where K is chosen from (4.12). Then, (4.30) becomes

$$\dot{z}_2 = \chi(t)A_0 z_2 + \lambda A_1 z_2 + BK z_2 \tag{4.32}$$

According to Assumption 4.8, for the Lyapunov function $V_u(z)$, we have $\dot{V}_u(z) = -z^T Q z$.

By defining $e_2 = z_2 - x$, we have the error dynamics as

$$\dot{e}_2 = \chi(t)A_0 e_2 + \lambda A_1 e_2 + B\tilde{K}_e e_{2D} + B\tilde{K}_e(z_{2D_0} - z_{2D}) \tag{4.33}$$

Because

$$
e_{2D} = e_2(t) - \int_{t-D}^{t} \left[\chi(\rho)A_0 e_2(\rho) + \lambda A_1 e_2(\rho) + B\tilde{K}_e e_2(\rho - D) \right] d\rho
$$
$$
- \int_{t-D}^{t} \left[B\tilde{K}_e(z_2(\rho - D_0) - z_2(\rho - D_0)) \right] d\rho
$$

and

$$z_{2D_0} - z_{2D} = \int_{t-D}^{t-D_0} \dot{z}_2(\rho) d\rho$$

then (4.33) can be written as

$$
\dot{e}_2 = \Xi_{e_2} + B\tilde{K}_e \int_{t-D}^{t-D_0} \dot{z}_2(\rho) d\rho - B\tilde{K}_e \int_{t-D}^{t} B\tilde{K}_e \int_{\rho-D}^{\rho-D_0} \dot{z}_2(\delta) d\delta d\rho
$$
$$
= \Xi_{e_2} + B\tilde{K}_e \int_{t-D}^{t-D_0} [\chi(\rho)A_0 z_2(\rho) + \lambda A_1 z_2(\rho) + BK z_2(\rho)] d\rho
$$
$$
- B\tilde{K}_e \int_{t-D}^{t} B\tilde{K}_e \int_{\rho-D}^{\rho-D_0} [\chi(\delta)A_0 z_2(\delta) + \lambda A_1 z_2(\delta) + BK z_2(\delta)] d\delta d\rho \tag{4.34}
$$

where Ξ_{e_1} is obtained by replacing e and K_e in Ξ_e by e_2 and $B\tilde{K}_e$. We will analyze the stability in the following two cases.

Case 1: $D \geq D_0$

For the Lyapunov-Krasovskii functional V_{e_2} obtained by substituting e and K_e in V_e (4.18) by e_2 and $B\tilde{K}_e$, we have

$$\dot{V}_{e_2} \leq \Xi_{V_{e_2}} + 2e_2^T B\tilde{K}_e \int_{t-D}^{t-D_0} [\chi(\rho)A_0 z_2(\rho) + \lambda A_1 z_2(\rho) + BK z_2(\rho)]d\rho \qquad (4.35)$$
$$- 2e_2^T B\tilde{K}_e \int_{t-D}^{t} B\tilde{K}_e \int_{\rho-D}^{\rho-D_0} [\chi(\delta)A_0 z_2(\delta) + \lambda A_1 z_2(\delta) + BK z_2(\delta)]d\delta d\rho$$

where $\Xi_{V_{e_2}}$ is obtained by replacing e by e_2, K_e by $B\tilde{K}_e$ and D by $\bar{D}$ in Ξ_{V_e}. We know that

$$- 2e_2^T B\tilde{K}_e \int_{t-D}^{t} B\tilde{K}_e \int_{\rho-D}^{\rho-D_0} \chi(\delta)A_0 z_2(\delta)d\delta d\rho$$
$$\leq \int_{t-D}^{t} \int_{\rho-D}^{\rho-D_0} |\chi(\delta)| e_2^T B\tilde{K}_e \Upsilon_1^{-1} (B\tilde{K}_e)^T e_2 d\delta d\rho$$
$$+ \int_{t-D}^{t} \int_{\rho-D}^{\rho-D_0} |\chi(\delta)| z_2^T(\delta)(B\tilde{K}_e A_0)^T \Upsilon_1 B\tilde{K}_e A_0 z_2(\delta)d\delta d\rho$$
$$\leq \epsilon \bar{D}\Delta D e_2^T B\tilde{K}_e \Upsilon_1^{-1} \tilde{K}_e^T B^T e_2 + \epsilon \int_{t-D}^{t} \int_{\rho-D}^{\rho-D_0} z_2^T(\delta)(B\tilde{K}_e A_0)^T \Upsilon_1 B\tilde{K}_e A_0 z_2(\delta)d\delta d\rho$$

$$- 2e_2^T B\tilde{K}_e \int_{t-D}^{t} B\tilde{K}_e \int_{\rho-D}^{\rho-D_0} \lambda A_1 z_2(\delta)d\delta d\rho$$
$$\leq \lambda \bar{D}\Delta D e_2^T B\tilde{K}_e \Upsilon_2^{-1} \tilde{K}_e^T B^T e_2 + \lambda \int_{t-D}^{t} \int_{\rho-D}^{\rho-D_0} z_2^T(\delta)(B\tilde{K}_e A_1)^T \Upsilon_2 B\tilde{K}_e A_1 z_2(\delta)d\delta d\rho$$

$$- 2e_2^T B\tilde{K}_e \int_{t-D}^{t} B\tilde{K}_e \int_{\rho-D}^{\rho-D_0} BK z_2(\delta)d\delta d\rho$$
$$\leq \bar{D}\Delta D e_2^T B\tilde{K}_e \Upsilon_3^{-1} \tilde{K}_e^T B^T e_2 + \int_{t-D}^{t} \int_{\rho-D}^{\rho-D_0} z_2^T(\delta)(B\tilde{K}_e BK)^T \Upsilon_3 B\tilde{K}_e BK z_2(\delta)d\delta d\rho$$

and

$$2e_2^T B\tilde{K}_e \int_{t-D}^{t-D_0} \chi(\rho)A_0 z_2(\rho)d\rho$$
$$\leq \epsilon \Delta D e_2^T \Upsilon_4^{-1} e_2 + \epsilon \int_{t-D}^{t-D_0} z_2(\rho)(B\tilde{K}_e A_0)^T \Upsilon_4 B\tilde{K}_e A_0 z_2(\rho)d\rho$$
$$2e_2^T B\tilde{K}_e \int_{t-D}^{t-D_0} \lambda A_1 z_2(\rho)d\rho$$
$$\leq \lambda \Delta D e_2^T \Upsilon_5^{-1} e_2 + \lambda \int_{t-D}^{t-D_0} z_2(\rho)(B\tilde{K}_e A_1)^T \Upsilon_5 B\tilde{K}_e A_1 z_2(\rho)d\rho$$

74

$$2e_2^T B \tilde{K}_e \int_{t-D}^{t-D_0} BK z_2(\rho) d\rho$$

$$\leq \Delta D e_2^T \Upsilon_6^{-1} e_2 + \int_{t-D}^{t-D_0} z_2(\rho)(B\tilde{K}_e BK)^T \Upsilon_6 B\tilde{K}_e BK z_2(\rho) d\rho$$

where $\Upsilon_i > 0$, $i = 1, \ldots, 6$. Then, we obtain

$$\dot{V}_{e_2} \leq \Xi_{V_{e_2}} + e_2^T S_3 e_2 + \int_{t-D}^{t} \int_{\rho-D}^{\rho-D_0} z_2^T(\delta) S_4 z_2(\delta) d\delta d\rho + \int_{t-D}^{t-D_0} z_2^T(\rho) S_5 z_2(\rho) d\rho$$

$$(4.36)$$

where

$$S_3 = \bar{D}\Delta DB\tilde{K}_e(\epsilon\Upsilon_1^{-1} + \lambda\Upsilon_2^{-1} + \Upsilon_3^{-1})\tilde{K}_e^T B^T + \Delta D(\epsilon\Upsilon_4^{-1} + \lambda\Upsilon_5^{-1} + \Upsilon_6^{-1})$$
$$S_4 = \epsilon(B\tilde{K}_e A_0)^T\Upsilon_1 B\tilde{K}_e A_0 + \lambda(B\tilde{K}_e A_1)^T\Upsilon_2 B\tilde{K}_e A_1 + (B\tilde{K}_e BK)^T\Upsilon_3 B\tilde{K}_e BK$$
$$S_5 = \epsilon(B\tilde{K}_e A_0)^T\Upsilon_4 B\tilde{K}_e A_0 + \lambda(B\tilde{K}_e A_1)^T\Upsilon_5 B\tilde{K}_e A_1 + (B\tilde{K}_e BK)^T\Upsilon_6 B\tilde{K}_e BK$$

We consider the following LFK

$$V_2 = V_{e_2} + V_u(z_2) + \int_{t-D}^{t} \int_{\rho}^{t} \int_{\delta-D}^{\delta-D_0} z_2^T(\zeta) S_4 z_2(\zeta) d\zeta d\delta d\rho$$

$$+ D \int_{t-D}^{t-D_0} \int_{\rho}^{t-D_0} z_2^T(\delta) S_4 z_2(\delta) d\delta d\rho + \Delta D \int_{t-D_0}^{t} z_2^T(\rho) S_5 z_2(\rho) d\rho$$

$$+ D\Delta D \int_{t-D_0}^{t} z_2^T(\rho) S_4 z_2(\rho) d\rho + \int_{t-D}^{t-D_0} \int_{\rho}^{t-D_0} z^T(\delta) S_5 z(\delta) d\delta d\rho$$

Thus, we have

$$\dot{V}_2 \leq \Xi_{V_{e_2}} + e_2^T S_3 e_2 - z_2^T Q z_2 + z_2^T(\bar{D}\Delta D S_4 + D_0\Delta D S_5)z_2 \qquad (4.37)$$

Therefore, we know $\dot{V}_2 < 0$ as long as LMIs (4.38) are true. In (4.38), $L_{11} = (\lambda A_1 + B\tilde{K}_e)^T + \lambda A_1 + B\tilde{K}_e$, $\bar{D}' = \bar{D}^{-1}$, $\Delta\bar{D}' = \Delta\bar{D}^{-1}$ and $D_0' = D_0^{-1}$.

Based on the known D and $\bar{D}$, we can find a feasible $\tilde{K}_e$ satisfying LMIs (4.38).

$$\begin{bmatrix} L_{11} & \epsilon^{\frac{1}{2}}B\tilde{K}_e A_0 & B\tilde{K}_e A_1 & I_n & \tilde{K}_e^T B^T & B\tilde{K}_e & I_n \\ & -\bar{D}'I_n & 0 & 0 & 0 & 0 & 0 \\ & & -\frac{\bar{D}'}{\lambda}I_n & 0 & 0 & 0 & 0 \\ & & & -\frac{\bar{D}'}{(\epsilon+\lambda)}I_n & 0 & 0 & 0 \\ & & & & -\bar{D}'I_n & 0 & 0 \\ & & & & & -\frac{\bar{D}'\Delta D'}{(\epsilon+\lambda+1)}I_n & 0 \\ & & & & & & -\frac{\Delta D'}{(\epsilon+\lambda+1)}I_n \end{bmatrix} < 0$$

$$(4.38a)$$

$$
\begin{bmatrix}
-Q & \epsilon^{\frac{1}{2}} B\tilde{K}_e A_0 & \epsilon^{\frac{1}{2}} B\tilde{K}_e A_0 & B\tilde{K}_e A_1 & B\tilde{K}_e A_1 & B\tilde{K}_e BK & B\tilde{K}_e BK \\
 & \Delta D' \bar{D}' I_n & 0 & 0 & 0 & 0 & 0 \\
 & & \Delta D' D_0' I_n & 0 & 0 & 0 & 0 \\
 & & & \Delta D' \bar{D}' I_n & 0 & 0 & 0 \\
 & & & & \Delta D' D_0' I_n & 0 & 0 \\
 & & & & & \Delta D' \bar{D}' I_n & 0 \\
 & & & & & & \Delta D' D_0' I_n
\end{bmatrix} < 0
$$

$$(4.38\text{b})$$

Case 2: $D < D_0$

For the same LKF V_{e_2}, we have

$$
\dot{V}_{e_2} \leq \Xi_{V_{e_2}} + e_2^T S_3 e_2 + \int_{t-D}^{t} \int_{\rho-D_0}^{\rho-D} z_2^T(\delta) S_4 z_2(\delta) d\delta d\rho + \int_{t-D_0}^{t-D} z_2^T(\rho) S_5 z_2(\rho) d\rho
$$

$$(4.39)$$

We consider the following LKF

$$
V_3 = V_{e_2} + V_u(z_2) + \int_{t-D}^{t} \int_{\rho}^{t} \int_{\delta-D_0}^{\delta-D} z_2^T(\zeta) S_4 z_2(\zeta) d\zeta d\delta d\rho
$$

$$
+ D \int_{t-D_0}^{t-D} \int_{\rho}^{t-D} z_2^T(\delta) S_4 z_2(\delta) d\delta d\rho + D\Delta D \int_{t-D}^{t} z_2^T(\rho) S_4 z_2(\rho) d\rho
$$

$$
+ \int_{t-D_0}^{t-D} \int_{\rho}^{t-D} z^T(\delta) S_5 z(\delta) d\delta d\rho + \Delta D \int_{t-D}^{t} z_2^T(\rho) S_5 z_2(\rho) d\rho
$$

and we can obtain the same result as in (4.38).

Based the above analysis, we can conclude the following theorem.

Theorem 4.17. *System* (4.11) *with predictor* (4.30) *and controller* (4.31) *is GAS if LMIs* (4.38) *are satisfied.*

4.4   Applications to UAVs

In this section, we apply the above controllers to UAV applications. First, we rewrite the dynamics of a UAV here

$$\dot{p}^n = v^n \tag{4.40a}$$

$$m\dot{v}^n = mgn_3 - TRb_3 \tag{4.40b}$$

$$\dot{\eta} = W\omega^b \tag{4.40c}$$

$$J\dot{\omega}^b = -\omega^b \times J\omega^b + \tau^b \tag{4.40d}$$

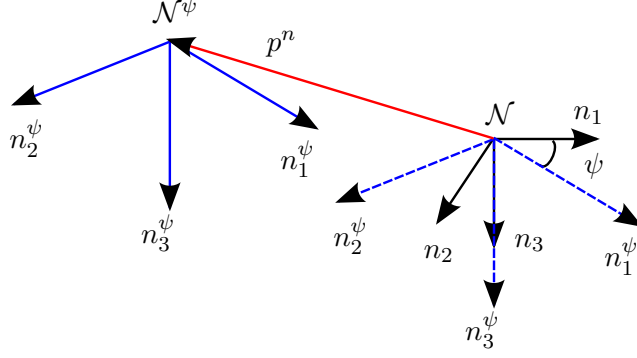with the same notations as in Chapter 2.

Figure 4.2: Comparison between $\mathcal{N}$ and $\mathcal{N}^\psi$.

As in Chapter 3, we apply the cascade control structure with the outer loop stabilizes translational variables and generates a reference signal fed to the inner loop. For the inner loop, we rewrite (4.40c) - (4.40d) as

$$\ddot{\eta} = \tilde{\tau}^b$$

where $\tilde{\tau}^b = [\tilde{\tau}_\phi^b, \tilde{\tau}_\theta^b, \tilde{\tau}_\psi^b]^T = \dot{W}\omega^b - WJ^{-1}\omega^b \times J\omega^b + \tau^b$. Measurements of rotational variables are available onboard, thus there values are un-delayed in the inner loop. Hence, we can design a PID controller for the yaw channel as

$$\tilde{\tau}_\psi^b = -k_\psi^p e_\psi - k_\psi^i \int_0^t e_\psi dt - k_\psi^d \dot{e}_\psi + \ddot{\psi}_d \tag{4.41a}$$

where $e_\psi = \psi - \psi_d$, ψ_d is the reference yaw and $k_\psi^p, k_\psi^i, k_\psi^d \in \mathbb{R}$ are the control gains. The yaw will be stabilized if $ak_\psi^p > k_\psi^i$, $k_\psi^d > a$, $\forall a > 0$. Thus, $\sup_t |\dot{\psi}(t)|$ will be bounded given that $\psi_d, \dot{\psi}_d, \ddot{\psi}_d$ are bounded.

Similarly, we design

$$\tilde{\tau}_\phi = -k_\phi^p e_\phi - k_\phi^i \int_0^t e_\phi dt - k_\phi^d \dot{e}_\phi + \ddot{\phi}_d \tag{4.41b}$$

$$\tilde{\tau}_\theta = -k_\theta^p e_\theta - k_\theta^i \int_0^t e_\theta dt - k_\theta^d \dot{e}_\theta + \ddot{\theta}_d \tag{4.41c}$$

where ϕ_d, θ_d are the reference roll and pitch, which will be determined in the outer loop.

4.4.1 Outer loop: Motion control

We introduce a new frame $\mathcal{N}^\psi = \{n_1^\psi, n_2^\psi, n_3^\psi\}$, whose origin is located at the center of the UAV. As shown in Figure 4.2, $\mathcal{N}^\psi$ can be obtained by translating from $\mathcal{N}$ by p^n and rotating around n_3 by angle ψ. Then, the outer-loop dynamics expressed in $\mathcal{N}^\psi$ is

$$\dot{p}^{\psi} = -\dot{\psi}\bar{A}_0 p^{\psi} + v^{\psi} \tag{4.42a}$$

$$\dot{v}^{\psi} = -\dot{\psi}\bar{A}_0 v^{\psi} + u^{\psi} \tag{4.42b}$$

where $p^{\psi} = R_{\psi}^T p^n$, $v^{\psi} = R_{\psi}^T v^n$, and

$$\bar{A}_0 = \begin{bmatrix} 0 & -1 & 0 \\ 1 & 0 & 0 \\ 0 & 0 & 0 \end{bmatrix}, R_{\psi} = \begin{bmatrix} \cos(\psi) & -\sin(\psi) & 0 \\ \sin(\psi) & \cos(\psi) & 0 \\ 0 & 0 & 1 \end{bmatrix}$$

$$u^{\psi} = gR_{\psi}^T n_3 - \frac{T}{m} \begin{bmatrix} \cos(\phi)\sin(\theta) \\ -\sin(\phi) \\ \cos(\phi)\cos(\theta) \end{bmatrix}$$

Define

$$x = \begin{bmatrix} p^{\psi} \\ v^{\psi} \end{bmatrix}, \chi(t) = \dot{\psi}(t), A_0 = -\begin{bmatrix} \bar{A}_0 & 0 \\ 0 & \bar{A}_0 \end{bmatrix}, \lambda = 1, A_1 = \begin{bmatrix} 0 & I \\ 0 & 0 \end{bmatrix}, B = \begin{bmatrix} 0 \\ I \end{bmatrix}, u = u^{\psi}$$

$$\tag{4.43}$$

Then, (4.42) can be rewritten in the form of (4.11). We can design the undelayed controller as $u(x) = Kx$, where $K \in \mathbb{R}^{3\times3}$ are proper control gains. When the delay D is known, it is straightforward to solve LMI (4.19) to find a $K_e \in \mathbb{R}^{6\times6}$ such that the value of D is maximized.

When D is unknown, we will design the predictor as (4.23). Therefore, we redefine

$$x = \begin{bmatrix} p^{\psi} + v^{\psi} \\ v^{\psi} \end{bmatrix}, \chi(t) = \dot{\psi}(t), A_0 = -\begin{bmatrix} \bar{A}_0 & 0 \\ 0 & \bar{A}_0 \end{bmatrix}$$

$$\lambda = 1, A_1 = \begin{bmatrix} 0 & I \\ 0 & 0 \end{bmatrix}, B = \begin{bmatrix} I \\ I \end{bmatrix}, u = u^{\psi} \tag{4.44}$$

and apply the result in Section 4.3.2.

Based on the outer loop controller $u = [u_1, u_2, u_3]^T$, we can obtain the thrust input and roll, pitch references for the inner loop

$$T = m\|u - gn_3^{\psi}\| \tag{4.45a}$$

$$\phi_d = \arcsin\left(\frac{m}{T}u_2\right) \tag{4.45b}$$

$$\theta_d = \arcsin\left(\frac{m}{T}u_1\cos(\phi_d)\right) \tag{4.45c}$$

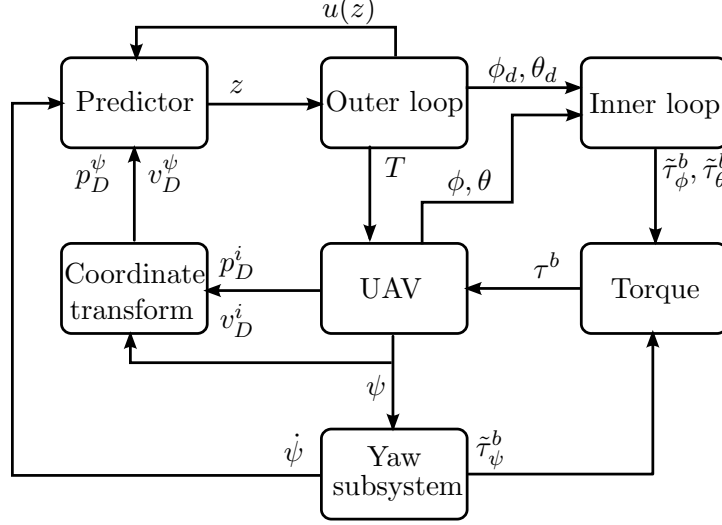The closed-loop diagram of tracking problems is shown in Figure 4.3.

Figure 4.3: Closed-loop structure for UAV tracking problem with predictor.

4.4.2 Outer loop: Visual servoing

In this section, we consider an image-based visual servoing problem with input delay. We will consider the image moments feature using the virtual camera model, as described in Section 2.1.3. We rewrite the image kinematics (2.19) and UAV dynamics here

$$\dot{q} = -\dot{\psi}\bar{A}_0 q - \frac{1}{z^*}v^v \tag{4.46}$$

$$\dot{v}^v = -\dot{\psi}\bar{A}_0 v^\psi + u^v \tag{4.47}$$

where $u^v = u^\psi$ and redefine

$$x = \begin{bmatrix} q - v^v \\ v^v \end{bmatrix}, \chi(t) = \dot{\psi}(t), A_0 = -\begin{bmatrix} \bar{A}_0 & 0 \\ 0 & \bar{A}_0 \end{bmatrix}, \lambda = \frac{1}{z^*}, A_1 = -\begin{bmatrix} 0 & I \\ 0 & 0 \end{bmatrix}, B = \begin{bmatrix} -I \\ I \end{bmatrix}$$

and $u = u^v$. Then, (4.46) can be written in the form of (4.11). Because λ is unknown in this case, we need to find a $\tilde{K}_e$ such that LMIs (4.29) are satisfied.

4.5 Simulation

To verify the results, we simulated the proposed predictor-based controller. The quadrotor is controlled by an inner-outer loop structure as shown in Figure 4.3. The inner loop follows the reference angles calculated from the outer loop. We consider both motion control and visual servoing problems.

4.5.1 Motion control

For the motion control problem (4.11), from Section 4.3, we know that the outer loop is stable for any K_e and D satisfying the LMI (4.19). We solve the following optimization problem to find K_e such that D is maximized:

$$\min_{K_e} D' \quad \text{s.t LMI (4.19)}$$

By choosing $\epsilon_1 = 0.1$, we get a maximum tolerable delay

$$D_{max} = 0.3 \text{ s}$$

and corresponding gain

$$K_e = \begin{bmatrix} -1.11 & 0 & 0 & -0.25 & 0 & 0 \\ 0 & -1.11 & 0 & 0 & -0.25 & 0 \\ 0 & 0 & -1.13 & 0 & 0 & -0.26 \\ 0.18 & 0 & 0 & -1.53 & 0 & 0 \\ 0 & 0.18 & 0 & 0 & -1.53 & 0 \\ 0 & 0 & 0.18 & 0 & 0 & -1.62 \end{bmatrix}$$

With K_e, we construct a predictor according to (4.14a). The quadrotor is controlled by an inner-outer loop structure as shown in Figure 4.3. We assume the state measurement delay $D = 0.2$ s. For the outer loop, for a given the controller

$$u(x) = Kx$$

will stabilize the non-delayed outer-loop dynamics, where $K = -[2I_3, 3I_3]$. The desired height is set to 1 m.

The trajectories of p^n with the proposed predictor-based controller are shown in Figure 4.4 in red. The trajectories p^n using controller $u(x)$ when no delay is present are shown with black dots. This controller is not able to stabilize the system in the presence of delay. The unstable trajectories are shown in dashed blue.

We assume the delay is not accurately known. The actual delay in the outer loop is set to be $D = 0.2$ s, while the estimate D_0 is set as 0.18 s. We choose $\Delta D = 0.02$ s. The UAV initially locates at $[0, 0, -0.8]$ m. We set the reference trajectory of p_{1d}^n, p_{2d}^n as a unit circle centred at the origin. The reference velocity is 0.2828 m/s. The reference of height and yaw are chosen as

$$p_{3d}^n = -1.2 + 0.2 \sin(0.4t)$$
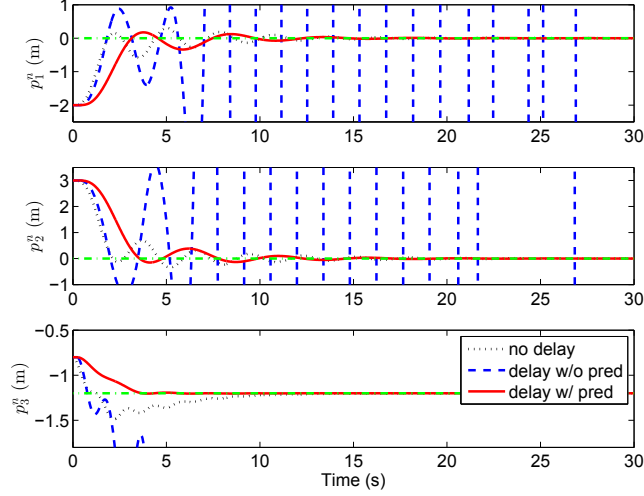$$\psi_d = 0.2 + 0.2 \sin(0.3t)$$

Figure 4.4: Simulation: trajectories of p^n when the delay is known.
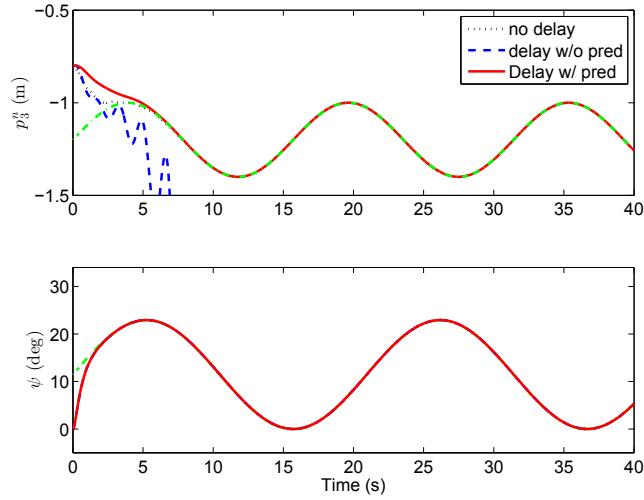

Figure 4.5: Simulation: trajectories of p_3^n and ψ when the delay is unknown.

We solve the LMIs (4.38) and obtain

$$\tilde{K}_e = \begin{bmatrix} -0.6275 & 0 & 0 & -0.7797 & 0 & 0 \\ 0 & -0.6275 & 0 & 0 & -0.7797 & 0 \\ 0 & 0 & -0.6416 & 0 & 0 & -0.8009 \end{bmatrix}$$

The position and yaw trajectories are shown in Figure 4.5 and 4.6. We can see p^n follows the desired trajectory with the proposed controller (4.31), as shown in red solid line.
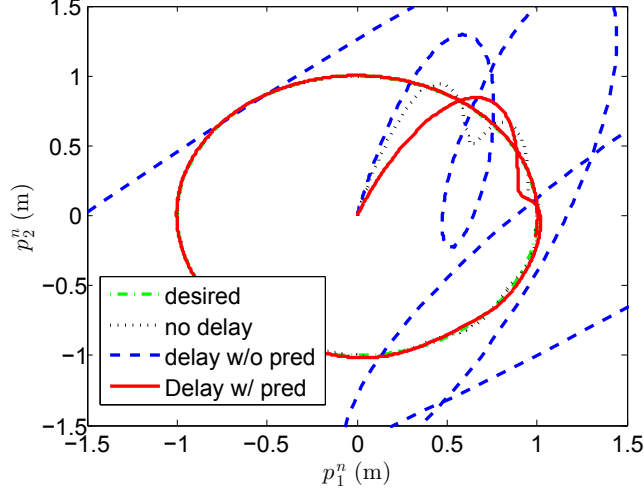
Figure 4.6: Simulation: UAV's trajectory on the $p_1^n - p_2^n$ plane when the delay is unknown.

4.5.2 Visual servoing

We assume four objects are located at $[0.1, -0.1, 0]^T$, $[0.2, 0.2, 0]^T$, $[-0.3, 0.3, 0]^T$, $[-0.4, -0.4, 0]^T$ m. The desired locations of objects in the image plane is set as $[0.1, -0.1]^T$, $[0.2, 0.2]^T$, $[-0.3, 0.3]^T$, $[-0.4, -0.4]^T$. Therefore, for visual servoing problem (4.46), we have $\lambda^* = 1$, which is assumed to be unknown. We set the bounds of λ as $\lambda \in [0.95, 1.05]$ and then $\Delta \lambda = 0.05$. The controller is chosen as

$$u(z_1) = Kz_1 - \tilde{K}_e(z_{1D} - x_D)$$

where $K = [2I_3, -I_3]$, $\tilde{K}_e$ is obtained by solving the LMIs (4.29) as

$$\tilde{K}_e = \begin{bmatrix} 0.5876 & 0 & 0 & -0.8201 & 0 & 0 \\ 0 & 0.5876 & 0 & 0 & -0.8201 & 0 \\ 0 & 0 & 0.6026 & 0 & 0 & -0.8468 \end{bmatrix}$$

and the maximum tolerable delay is

$$D_{max} = 0.204 \text{ s}$$

We use the upper bound of λ as the estimate, i.e., $\tilde{\lambda} = \bar{\lambda} = 1.05$. The trajectories of UAV's position in $\mathcal{N}$ p^n are given in Figure 4.7. Figure 4.8 gives the projected trajectories of objects on the image plane, where the circle marker shows the starting position and the square one is the desired position.
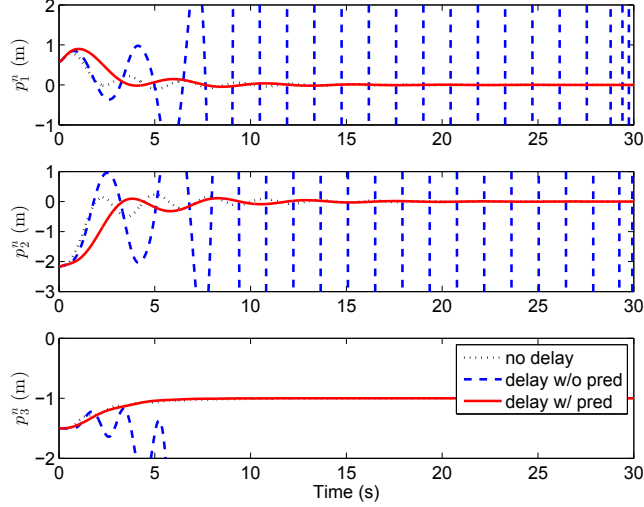
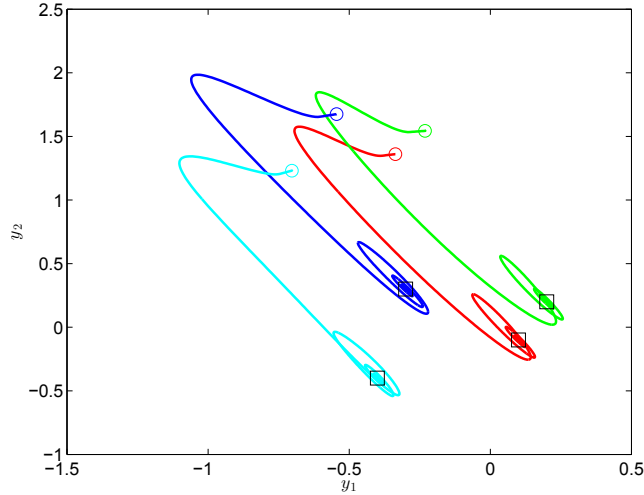Figure 4.7: Simulation: UAV's trajectory of visual servoing problem.

Figure 4.8: Simulation: trajectories of objects on the image plane.

4.6 Experiments

In this section, we will experimentally validate the proposed nested saturation controller on our UAV platform. The experiments are implemented on ANCLQ 2.0. As shown in [104], the transmission delay from Vicon to PX4 is 0.025 s. To show the controller's robustness to delay, we add more delay on purpose. We will only consider motion control problem in experiments.

The controller used when delay is not added is

$$u = -4v^\psi - 2p^\psi \tag{4.48}$$

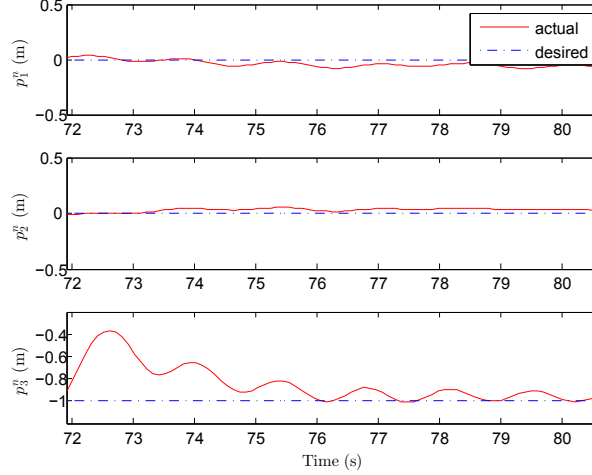First, we consider the hovering problem, where the desired position as $[0, 0, -1]$ m.

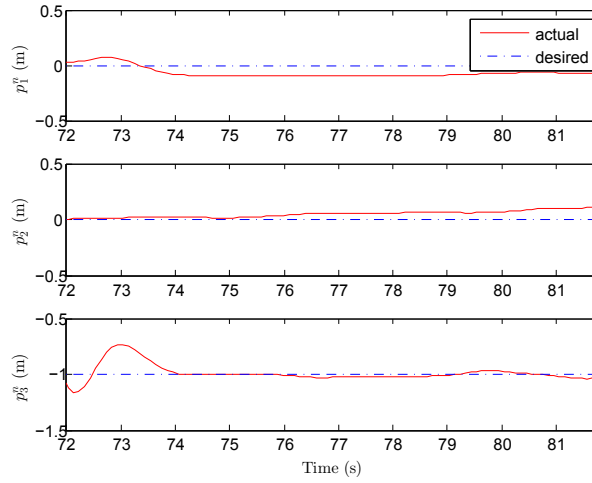Figure 4.9: Experiment: UAV's trajectories of hovering.

Figure 4.10: Experiment: UAV's trajectories of hovering with proposed controller.

We add 0.1 s delay while the Mavlink package is sent from Vicon system, which means the total delay is $D = 0.125$ s. The trajectory of the UAV with controller (4.48) is shown in Figure 4.9. Then, we follow Section 4.3.2 to design the predictor. We set $D = 0.12$ and $\Delta D = 0.05$, by solving (4.38), we get

$$
\tilde{K}_e = \begin{bmatrix} -0.9996 & 0 & 0 & -1.2529 & 0 & 0 \\ 0 & -0.9996 & 0 & 0 & -1.2529 & 0 \\ 0 & 0 & -1.0225 & 0 & 0 & -1.2883 \end{bmatrix}
$$

The UAV's trajectory is shown in Figure 4.10. It is noticeable that the performance is improved significantly with the predictor-based controller.

We also consider a tracking problem, where the desired trajectory is set as a circle with the centre located at $[0, 0]$ m and the radius as 0.3 m. The desired speed is 0.04π m/s and the desired height is -1 m. The $\tilde{K}_e$ is the same as above. The
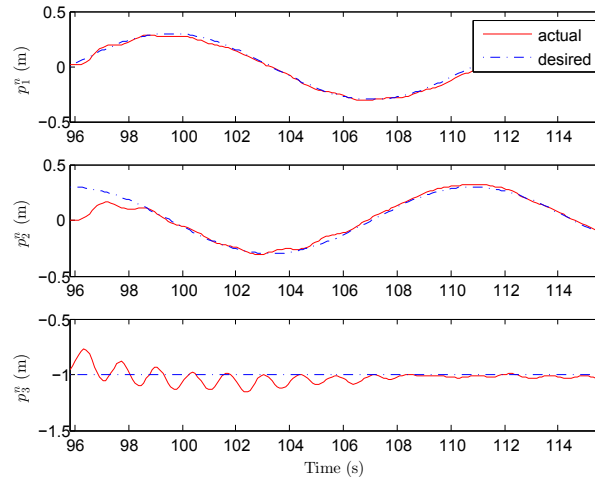
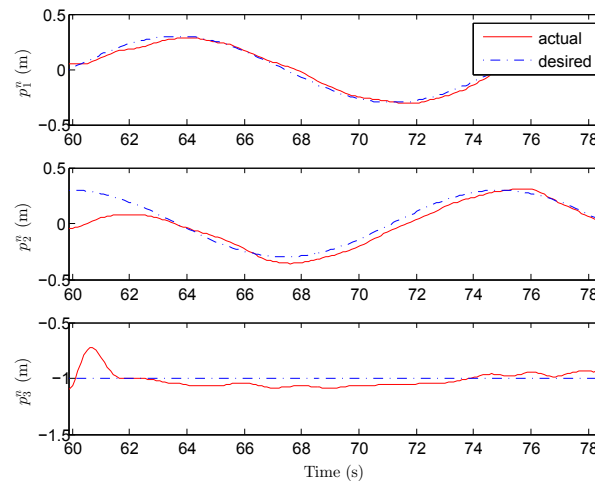Figure 4.11: Experiment: UAV's trajectories of tracking.

Figure 4.12: Experiment: UAV's trajectories of tracking with proposed controller.
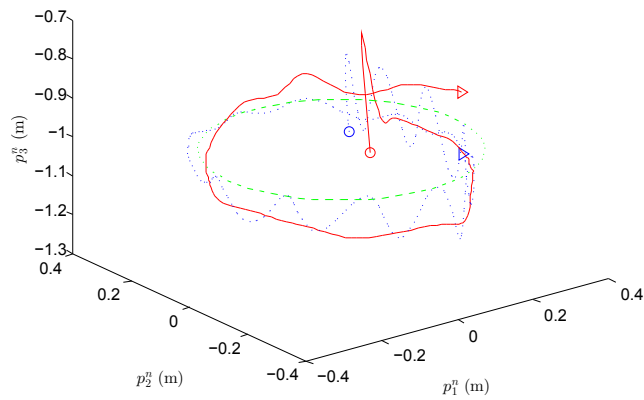

Figure 4.13: Experiment: 3D trajectories comparison.

85

results without and with the predictor is shown in Figure 4.11 and 4.12. For better comparison, we also plot the 3D trajectories together, as shown in Figure 4.13, where the red solid line is the trajectory with predictor.

4.7 Conclusion

In this chapter predictor-based controllers for a class of systems with input delay are proposed. These control problems relate to UAV motion control and visual servoing problems. A rigorous stability proof using LKFs is provided to obtain sufficient conditions for global asymptotic stability of the outer loop. We also validate the proposed controllers experimentally.

Chapter 5

Robustness Analysis of a Saturated Controller to Time Delay

5.1 Introduction

In Chapter 3, we proposed a nested saturation controller based on the inner-outer-loop structure for UAVs. The cascade structure allowed us to put constraints on thrust, roll and pitch at the same time. However, the time delay in the measurement was not considered. The experimental indoor UAV platform developed at ANCL includes a Vicon motion capture system, which estimates vehicle's position and velocity and sends these values to the quadrotor via radio communication. The delay will be introduced in the wireless transmission. Therefore, it is necessary to analyze the impact of time delay on the system stability.

In Chapter 4, we proposed a predictor-based framework for UAV control with delay. Unfortunately, this approach cannot be applied to UAVs with saturated controller, because the stability analysis of nested saturation controllers was based on induction. Different Lyapunov function was designed for each step to guarantee its convergence to an invariant set, thus there was no unified Lyapunov function. Therefore, in this chapter we apply the emulation approach, as described in Section 4.2.3, to analyze the robustness of the nested saturated controller for UAVs introduced in Chapter 3 with respect to time delay. This work is inspired by [60], which analyzed the robustness of the nested saturation controller for chains of integrators.

This method is suitable for small delay cases and is easy to implement because no extra design is needed. Compared to the nested saturation controller designed in Chapter 3, we make a slight change to simplify the analysis. In Chapter 3, the saturated controller is design based on the UAV translational dynamics in the body
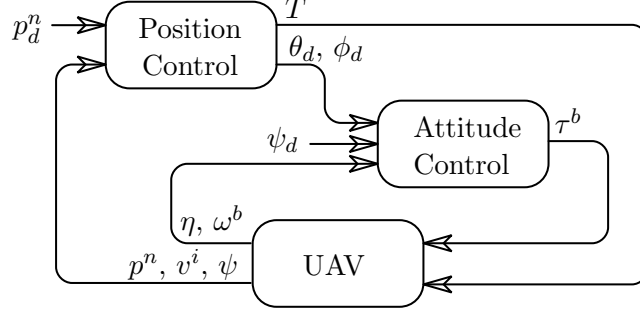
Figure 5.1: The closed-loop structure diagram.

frame. In this chapter, we propose a new frame. The coupling term of dynamics in this frame is still skew symmetric, but only the yaw rate from the inner loop is involved. In Chapter 3, we treat each component of a vector separately. However, in this chapter we analyze the stability based on its norm. This will simplify the proof as will be shown in the following analysis.

The structure of this chapter is as follows. In Section 5.2, we describe the dynamics considered in this chapter and the nested saturation controller. In Section 5.3, we analyze the robustness of the saturated controller with respect to time delay. An upper bound on time delay is derived as a sufficient condition for stability. Experimental results in Section 5.4 validates the analysis.

5.2 Controller design

As before, we apply the inner-outer loop control structure. The inner loop tracks the reference roll and pitch calculated from the outer loop based on a PID controller. On our experimental platform, the Vicon system provides the vehicle's position and translational velocity, hence, the transmission delay during this process only affect the outer loop. Therefore, we only consider the outer loop with time delay. The structure diagram of the closed-loop system is shown in Figure 5.1.

Instead of working in the body frame as in Chapter 3, we will work on the new frame $\mathcal{N}^\psi$ as introduced in Section 4.4.1. We rewrite the outer-loop dynamics of UAVs in $\mathcal{N}^\psi$ as

$$\dot{p}^\psi = -\dot{\psi}\bar{A}_0 p^\psi + v^\psi \tag{5.1a}$$
$$\dot{v}^\psi = -\dot{\psi}\bar{A}_0 v^\psi + u^\psi \tag{5.1b}$$

where p^ψ, v^ψ are the position and velocity vector expressed in $\mathcal{N}^\psi$, and $p^\psi = R_\psi^T p^n$,

$$v^\psi = R_\psi^T v^n,$$

$$R_\psi = \begin{bmatrix} \cos(\psi) & -\sin(\psi) & 0 \\ \sin(\psi) & \cos(\psi) & 0 \\ 0 & 0 & 1 \end{bmatrix}, u^\psi = gR_\psi^T n_3^\psi - \frac{T}{m} \begin{bmatrix} \cos(\phi)\sin(\theta) \\ -\sin(\phi) \\ \cos(\phi)\cos(\theta) \end{bmatrix}$$

and $\bar{A}_0 = \text{sk}(n_3^\psi)$.

We define

$$y_1 = p^\psi + v^\psi$$
$$y_2 = v^\psi$$
$$u = u^\psi$$

and then (5.1) can be rewritten as

$$\dot{y}_1 = -\dot{\psi}\bar{A}_0 y_1 + y_2 + u \tag{5.2a}$$
$$\dot{y}_2 = -\dot{\psi}\bar{A}_0 y_2 + u \tag{5.2b}$$

based on the work in Chapter 3, we know the following nested saturation controller

$$u = -\Sigma_2\left(y_2 + \Sigma_1(y_1)\right) \tag{5.3}$$

will guarantee the stability of the outer loop (5.2), where $\Sigma_i : \mathbb{R}^3 \to \mathbb{R}^3$, $i = 1, 2$, are defined as $\Sigma_i(s) = [\sigma_i(s_1), \sigma_i(s_2), \sigma_i(s_3)]^T$ and $s = [s_1, s_2, s_3]^T, s_j \in \mathbb{R}, j = 1, 2, 3$. The saturation function $\sigma_i : \mathbb{R} \to \mathbb{R}$ satisfies

1) $\sigma_i(r)$ is continuous and nondecreasing;

2) $r\sigma_i(r) > 0$ for all $r \neq 0$;

3) $\sigma_i(r) = r$ for all $|r| \leq L_i$;

4) $|\sigma_i(r)| \leq M_i$.

Remark 5.1. Dynamics (5.2) is different from the dynamics considered in Chapter 3. However, the different terms are both skew-symmetric. This will make no difference for the stability analysis. Moreover, we assume each component of Σ_i is the same saturation function for simplicity, which implies we cannot set separate bounds for thrust, roll and pitch as stated in Chapter 3.

With the presence of a constant time delay in the measurement, the controller (5.3) will become

$$u = -\Sigma_2\left(y_2(t - D) + \Sigma_1(y_1(t - D))\right) \tag{5.4}$$

where $D > 0$ is known. In this chapter, we will analyze the impact of measurement delay D in the controller (5.4) on the stability of (5.2).

5.3   Robust analysis with respect to time delay

We will start the analysis with a lemma.

Lemma 5.2. *For $a_1, a_2 \in \mathbb{R}^3$, if $\|a_1\| > \|a_2\|$ and $\|a_2\| \leq L_i/2$, then $a_1 \Sigma_i (a_1 + a_2) > 0$.*

Proof. We use the spherical coordinates to express a_j, $j = 1, 2$, i.e.,

$$
a_j = r_j \begin{bmatrix} \sin(\alpha_j)\cos(\beta_j) \\ \sin(\alpha_j)\sin(\beta_j) \\ \cos(\alpha_j) \end{bmatrix}
$$

where $r_j = \|a_j\|$, $0 \leq \alpha_j \leq \pi$ and $0 \leq \beta_j \leq 2\pi$.

When $0 < \alpha_1, \beta_1 \leq \frac{\pi}{2}$, since $\|a_1\| > \|a_2\|$ we have

$$
\begin{aligned}
a_1^T \Sigma_i (a_1 + a_2) =& r_1 \begin{bmatrix} s_{\alpha_1} c_{\beta_1} \\ s_{\alpha_1} s_{\beta_1} \\ c_{\alpha_1} \end{bmatrix}^T \Sigma_i \left(\begin{bmatrix} r_1 s_{\alpha_1} c_{\beta_1} + r_2 s_{\alpha_2} c_{\beta_2} \\ r_1 s_{\alpha_1} s_{\beta_1} + r_2 s_{\alpha_2} s_{\beta_2} \\ r_1 c_{\alpha_1} + r_2 c_{\alpha_2} \end{bmatrix} \right) \\
>& r_1 \begin{bmatrix} s_{\alpha_1} c_{\beta_1} \\ s_{\alpha_1} s_{\beta_1} \\ c_{\alpha_1} \end{bmatrix}^T \Sigma_i \left(\begin{bmatrix} r_2 s_{\alpha_1} c_{\beta_1} + r_2 s_{\alpha_2} c_{\beta_2} \\ r_2 s_{\alpha_1} s_{\beta_1} + r_2 s_{\alpha_2} s_{\beta_2} \\ r_2 c_{\alpha_1} + r_2 c_{\alpha_2} \end{bmatrix} \right)
\end{aligned}
$$

Because

$$
\begin{aligned}
|r_2 s_{\alpha_1} c_{\beta_1} + r_2 s_{\alpha_2} c_{\beta_2}| &< 2r_2 \leq L_i \\
|r_2 s_{\alpha_1} s_{\beta_1} + r_2 s_{\alpha_2} s_{\beta_2}| &< 2r_2 \leq L_i \\
|r_2 c_{\alpha_1} + r_2 c_{\alpha_2}| &< 2r_2 \leq L_i
\end{aligned}
$$

saturation functions σ_i will become linear, thus

$$
\begin{aligned}
a_1^T \Sigma_i (a_1 + a_2) >& r_1 \begin{bmatrix} s_{\alpha_1} c_{\beta_1} \\ s_{\alpha_1} s_{\beta_1} \\ c_{\alpha_1} \end{bmatrix}^T \begin{bmatrix} r_2 s_{\alpha_1} c_{\beta_1} + r_2 s_{\alpha_2} c_{\beta_2} \\ r_2 s_{\alpha_1} s_{\beta_1} + r_2 s_{\alpha_2} s_{\beta_2} \\ r_2 c_{\alpha_1} + r_2 c_{\alpha_2} \end{bmatrix} \\
=& r_1 r_2 (1 + \Gamma)
\end{aligned}
$$

where $\Gamma = s_{\alpha_1}c_{\beta_1}s_{\alpha_2}c_{\beta_2} + s_{\alpha_1}s_{\beta_1}s_{\alpha_2}s_{\beta_2} + c_{\alpha_1}c_{\alpha_2}$.

$$
\begin{aligned}
|\Gamma| &= |s_{\alpha_1}s_{\alpha_2}\left[c_{\beta_1}c_{\beta_2} + s_{\beta_1}s_{\beta_2}\right] + c_{\alpha_1}c_{\alpha_2}| \\
&= |s_{\alpha_1}s_{\alpha_2}c_{\beta_1-\beta_2} + c_{\alpha_1}c_{\alpha_2}| \\
&\leq \max(|s_{\alpha_1}s_{\alpha_2} + c_{\alpha_1}c_{\alpha_2}|, |-s_{\alpha_1}s_{\alpha_2} + c_{\alpha_1}c_{\alpha_2}|) \\
&= \max(|c_{\alpha_1-\alpha_2}|, |c_{\alpha_1+\alpha_2}|) \leq 1
\end{aligned}
$$

Therefore, $a_1^T \Sigma_i (a_1 + a_2) > 0$.

Similarly, we can prove $a_1^T \Sigma_i (a_1 + a_2) > 0$ when $\frac{\pi}{2} < \alpha_1, \beta_1 < 2\pi$. $\qquad \square$

With this lemma, we can prove the stability of system (5.2) with the delayed controller (5.4). Since the yaw angle ψ is controlled by the inner loop, we can make the following assumption.

Assumption 5.3. The rate of yaw angle $\dot{\psi}$ is bounded.

First, we consider a Lyapunov function $V_2 = \frac{1}{2}y_2^T y_2$, then we have

$$
\begin{aligned}
\dot{V}_2 &= -y_2^T(t)\Sigma_2\left(y_2(t-D) + \Sigma_1(y_1(t-D))\right) \\
&= -y_2^T(t)\Sigma_2\left(y_2(t) + y_2(t-D) - y_2(t) + \Sigma_1(y_1(t-D))\right)
\end{aligned}
$$

Since

$$
y_2(t-D) - y_2(t) = -\int_{t-D}^{t} \dot{y}_2(\rho)d\rho
$$

based on mean value theorem, there exists a $\varrho \in [t-D, t]$ such that

$$
\begin{aligned}
&\|y_2(t-D) - y_2(t)\| \\
=&\| -\int_{t-D}^{t}\left[-\dot{\psi}(\rho)\bar{A}_0 y_2(\rho) - \Sigma_2\left(y_2(\rho-D) + \Sigma_1(y_1(\rho-D))\right)\right]d\rho\| \\
\leq& \epsilon D\|y_2(\varrho)\| + \sqrt{3}DM_2
\end{aligned}
$$

where $\epsilon = \sup_t |\dot{\psi}(t)|$. Therefore,

$$
\begin{aligned}
&\|y_2(t) + y_2(t-D) - y_2(t) + \Sigma_1(y_1(t-D))\| \\
\geq& \|y_2(t)\| - \|y_2(t-D) - y_2(t)\| - \|\Sigma_1(y_1(t-D))\| \\
\geq& \|y_2(t)\| - \epsilon D\|y_2(\varrho)\| - \sqrt{3}DM_2 - \sqrt{3}M_1 \\
=&(1 - \epsilon D)\|y_2(t)\| + \epsilon D(\|y_2(t)\| - \|y_2(\varrho)\|) - \sqrt{3}DM_2 - \sqrt{3}M_1
\end{aligned}
$$

Because

$$
\|y_2(t)\| - \|y_2(\varrho)\| = \sqrt{2}V_2^{\frac{1}{2}}(t) - \sqrt{2}V_2^{\frac{1}{2}}(\varrho)
$$

$$= \sqrt{2} \int_{\varrho}^{t} \frac{1}{2} V_2^{-\frac{1}{2}}(\rho) \dot{V}_2(\rho) d\rho = - \int_{\varrho}^{t} \frac{y_2^T(\rho)}{\|y_2(\rho)\|} \Sigma_2(\cdot) d\rho$$

and $\varrho \in [t - D, t]$, we have $|\|y_2(t)\| - \|y_2(\varrho)\|| \leq DM_2$. Hence,

$$\|y_2(t) + y_2(t - D) - y_2(t) + \Sigma_1(y_1(t - D))\|$$
$$\geq (1 - \epsilon D)\|y_2(t)\| - \epsilon D^2 M_2 - \sqrt{3}DM_2 - \sqrt{3}M_1$$

If

$$\epsilon D < 1 \tag{5.5}$$

$$\epsilon D^2 M_2 + \sqrt{3}DM_2 + \sqrt{3}M_1 \leq \frac{1 - \epsilon D}{2} L_2 \tag{5.6}$$

then based on Lemma 5.2, when $(1 - \epsilon D)\|y_2(t)\| > \frac{1 - \epsilon D}{2} L_2$, i.e., $\|y_2(t)\| > \frac{L_2}{2}$

$$\dot{V}_2 = - y_2^T(t) \Sigma_2 (y_2(t) + y_2(t - D) - y_2(t) + \Sigma_1(y_1(t - D))) < 0$$

i.e., y_2 will converge to the set $Q_2 = \{y_2|\|y_2\| < \frac{L_2}{2}\}$ and stay within. If we choose

$$\sqrt{3}M_1 \leq \frac{L_2}{2} \tag{5.7}$$

then, because $\|y_2\| + \|\Sigma_1(\cdot)\| \leq L_2$, all three components of Σ_2 will become linear. Therefore, the dynamics of y_1 becomes

$$\dot{y}_1(t) = - \dot{\psi} \bar{A}_0 y_1(t) + y_2(t) - y_2(t - D) - \Sigma_1(y_1(t - D))$$

Considering the Lyapunov function $V_1 = \frac{1}{2} y_1^T y_1$, we have

$$\dot{V}_1 = y_1^T(t)(y_2(t) - y_2(t - D)) - y_1^T(t)\Sigma_1(y_1(t) + y_1(t - D) - y_1(t))$$

because y_2 already entered the set Q_2, we have $\|y_2(t) - y_2(t - D)\| \leq \epsilon D \frac{L_2}{2} + \sqrt{3}DM_2$. Thus,

$$\|y_1(t - D) - y_1(t)\| = \| - \int_{t-D}^{t} \dot{y}_1(\rho) d\rho \|$$
$$= \| - \int_{t-D}^{t} \left[-\dot{\psi}(\rho)\bar{A}_0 y_1(\rho) + y_2(\rho) - y_2(\rho - D) - \Sigma_1(y_1(\rho - D)) \right] d\rho \|$$
$$\leq \epsilon D \|y_1(\varrho)\| + \int_{t-D}^{t} \|y_2(\rho) - y_2(\rho - D)\| d\rho + \sqrt{3}DM_1$$
$$= \epsilon D \|y_1(\varrho)\| + \epsilon D^2 \frac{L_2}{2} + \sqrt{3}D^2 M_2 + \sqrt{3}DM_1$$

where $\varrho \in [t - D, t]$. Then,

$$\|y_1(t) + y_1(t - D) - y_1(t)\| \geq \|y_1(t)\| - \|y_1(t - D) - y_1(t)\|$$

$$\geq (1 - \epsilon D)\|y_1(t)\| + \epsilon D(\|y_1(t)\| - \|y_1(\varrho)\|) - (\epsilon D^2 \frac{L_2}{2} + \sqrt{3}D^2 M_2 + \sqrt{3}DM_1)$$

On the other hand,

$$\|y_1(t)\| - \|y_1(\varrho)\| = \sqrt{2}V_1^{\frac{1}{2}}(t) - \sqrt{2}V_1^{\frac{1}{2}}(\varrho) = \sqrt{2}\int_\varrho^t \frac{1}{2}V_1^{-\frac{1}{2}}(\rho)\dot{V}_1(\rho)d\rho$$

$$= \int_\varrho^t \frac{y_1^T(\rho)}{\|y_1(\rho)\|}(y_2(\rho) - y_2(\rho - D) - \Sigma_1(\cdot))d\rho$$

$$\leq \int_{t-D}^t \|y_2(\rho) - y_2(\rho - D)\|d\rho + DM_1$$

$$\leq \epsilon D^2 \frac{L_2}{2} + \sqrt{3}D^2 M_2 + DM_1$$

Thus,

$$\|y_1(t) + y_1(t - D) - y_1(t)\| \geq (1 - D\epsilon)\|y_1(t)\| - \epsilon D(\epsilon D^2 \frac{L_2}{2} + \sqrt{3}D^2 M_2 + DM_1)$$

$$- (\epsilon D^2 \frac{L_2}{2} + \sqrt{3}D^2 M_2 + \sqrt{3}DM_1)$$

similarly, if

$$\epsilon D(\epsilon D^2 \frac{L_2}{2} + \sqrt{3}D^2 M_2 + DM_1) + (\epsilon D^2 \frac{L_2}{2} + \sqrt{3}D^2 M_2 + \sqrt{3}DM_1) \leq (1 - D\epsilon)\frac{L_1}{2}$$

$$(5.8)$$

then y_1 will eventually enter the set $Q_1 = \{y_1\|\|y_1\| < \frac{L_1}{2}\}$. Therefore, Σ_2, Σ_1 will both be in their linear regions. Then, (5.2) becomes

$$\dot{y}_1 = -\dot{\psi}\bar{A}_0 y_1 + y_2 - y_2(t - D) - y_1(t - D)$$
$$\dot{y}_2 = -\dot{\psi}\bar{A}_0 y_2 - y_2(t - D) - y_1(t - D)$$

Define $y = [y_1, y_2]^T$, then we can rewrite the system (5.2) as

$$\dot{y}(t) = \dot{\psi}(t)A_0 y(t) + A_1 y(t) + A_2 y(t - D)$$

where

$$A_0 = - \begin{bmatrix} \bar{A}_0 & 0 \\ 0 & \bar{A}_0 \end{bmatrix}, A_1 = \begin{bmatrix} 0 & I_3 \\ 0 & 0 \end{bmatrix}, A_2 = - \begin{bmatrix} I_3 & I_3 \\ I_3 & I_3 \end{bmatrix}$$

and I_3 is the 3×3 identity matrix.

We know that

$$y(t - D) = y(t) - \int_{t-D}^{t} \dot{y}(\rho)d\rho$$

$$= y(t) - \int_{t-D}^{t} \left[\dot{\psi}(\rho)A_0 y(\rho) + A_1 y(\rho) + A_2 y(\rho - D) \right] d\rho$$

then

$$\dot{y}(t) = \dot{\psi}(t)A_0 y(t) + (A_1 + A_2)y(t)$$

$$- A_2 \int_{t-D}^{t} \left[\dot{\psi}(\rho)A_0 y(\rho) + A_1 y(\rho) + A_2 y(\rho - D) \right] d\rho$$

Consider a Lyapunov-Krasovskii functional

$$V_0 = y^T y + \int_{-D}^{0} \int_{t+\rho}^{t} y^T(\delta)S_1 y(\delta)d\delta d\rho + \int_{-2D}^{-D} \int_{t+\rho}^{t} y^T(\delta)S_2 y(\delta)d\delta d\rho$$

where $S_1, S_2 > 0$ are to be determined. Then its derivative is

$$\dot{V}_0 = y^T \dot{y} + \dot{y}^T y + \int_{-D}^{0} \left[y^T(t)S_1 y(t) - y^T(t+\rho)S_1 y(t+\rho) \right] d\rho$$

$$+ \int_{-2D}^{-D} \left[y^T(t)S_2 y(t) - y^T(t+\rho)S_2 y(t+\rho) \right] d\rho$$

$$= y^T(A_1^T + A_2^T + A_1 + A_2)y$$

$$- 2y^T(t)A_2 \int_{t-D}^{t} \left[\dot{\psi}(\rho)A_0 y(\rho) + A_1 y(\rho) + A_2 y(\rho - D) \right] d\rho$$

$$+ \int_{-D}^{0} \left[y^T(t)S_1 y(t) - y^T(t+\rho)S_1 y(t+\rho) \right] d\rho$$

$$+ \int_{-2D}^{-D} \left[y^T(t)S_2 y(t) - y^T(t+\rho)S_2 y(t+\rho) \right] d\rho$$

Since

$$- 2y^T A_2 \int_{t-D}^{t} \dot{\psi}(\rho)A_0 y(\rho)d\rho$$

$$\leq \int_{t-D}^{t} |\dot{\psi}(\rho)| \left[y^T A_2 A_0 \Gamma_1^{-1} A_0^T A_2^T y + y^T(\rho)\Gamma_1 y(\rho) \right] d\rho$$

$$\leq \epsilon D y^T A_2 A_0 \Gamma_1^{-1} A_0^T A_2^T y + \int_{t-D}^{t} |\dot{\psi}(\rho)| y^T(\rho)\Gamma_1 y(\rho)d\rho$$

and

$$-2y^T A_2 \int_{t-D}^{t} A_1 y(\rho)d\rho \leq D y^T A_2 A_1 \Gamma_2^{-1} A_1^T A_2^T y + \int_{t-D}^{t} y^T(\rho)\Gamma_2 y(\rho)d\rho$$

94

and

$$- 2y^T A_2 \int_{t-D}^{t} A_2 y(\rho - D) d\rho$$

$$\leq D y^T A_2 \Gamma_3^{-1} A_2^T y + \int_{t-D}^{t} y^T (\rho - D) K_e^T \Gamma_3 A_2 y(\rho - D) d\rho$$

where $\Gamma_1, \Gamma_2, \Gamma_3 > 0$, if we choose S_1, S_2 as

$$S_1 = \epsilon \Gamma_1 + \Gamma_2$$
$$S_2 = A_2^T \Gamma_3 A_2$$

then we obtain

$$\dot{V}_0 \leq y^T (A_1^T + A_2^T + A_1 + A_2) y + \epsilon D y^T A_2 A_0 \Gamma_1^{-1} A_0^T A_2^T y$$
$$+ D y^T A_2 A_1 \Gamma_2^{-1} A_1^T A_2^T y + D y^T A_2 \Gamma_3^{-1} A_2^T y + D e^T (S_1 + S_2) e$$

We choose $\Gamma_i = I_6, i = 1, 2, 3$, then the sufficient condition for $\dot{V}_0 < 0$ can be expressed using the following LMI

$$G < 0 \tag{5.9}$$

where

$$G = \begin{bmatrix} G_{11} & \epsilon^{\frac{1}{2}} A_2 A_0 & A_2 A_1 & A_2 & I & A_2^T \\ & -D' I_6 & 0 & 0 & 0 & 0 \\ & & -D' I_6 & 0 & 0 & 0 \\ & & & -D' I_6 & 0 & 0 \\ & & & & G_{55} & 0 \\ & & & & & -D' I_6 \end{bmatrix}$$

where $D' = D^{-1}$, $G_{11} = A_1^T + A_2^T + A_1 + A_2$ and $G_{55} = -\frac{D'}{(\epsilon+1)} I_6$.

Based on the above analysis, we conclude the following theorem.

Theorem 5.4. *For the controller* (5.4) *with* M_1, L_2 *satisfying* (5.7), *if there exists a constant* D *such that* (5.5),(5.6),(5.8),(5.9) *are satisfied, then system* (5.1) *is globally asymptotically stable.*

Remark 5.5. In [15, 61], we extend the Teel's nested saturation method [33] to the vector form based on UAV's dynamics in body frame. This work can be seen as an extension of [15, 61] to the case with input delay. However, in this chapter we work in $\mathcal{N}^\psi$. The difference between the two dynamics is the coupling terms, which involve $\text{sk}(\omega^b)$ and $\text{sk}(\dot{\psi} b_3)$, respectively. However, there is an important property

Table 5.1: Experimental control parameters.

M_2	5.0
M_1	0.72

in common, i.e., $x^T \operatorname{sk}(\omega^b)x = x^T \operatorname{sk}(\dot{\psi}b_3)x = 0, \forall x \in \mathbb{R}^3$. In [15, 61], we treated each components of a vector separately when applying Teel's method, while in this chapter, we treated it as a vector instead, which makes the proof less complicated.

Remark 5.6. To obtain the upper bound on the time delay D under the above conditions (5.5), (5.6), (5.8), (5.9), we can solve the LMI (5.9) for a given ϵ using Matlab LMI toolbox. For example, when $\epsilon = 0.1$, we get $D_{\max} = 0.2608$ s; when $\epsilon = 0$, we can get $D_{\max} = 0.2725$ s. For simplicity, we can assume $M_2 = L_2$ and $M_1 = L_1$. Then, (5.6) and (5.8) become

$$\epsilon D^2 M_2 + \sqrt{3}DM_2 + \sqrt{3}M_1 < \frac{1 - \epsilon D}{2}M_2$$

$$\epsilon D(\epsilon D^2 \frac{M_2}{2} + \sqrt{3}D^2 M_2 + DM_1) + (\epsilon D^2 \frac{M_2}{2} + \sqrt{3}D^2 M_2 + \sqrt{3}DM_1) \le (1 - D\epsilon)\frac{M_1}{2}$$

For the given ϵ, M_2, we could apply binary search algorithm in the range $[0, D_{\max}]$. The termination condition is the existence of $M_1 > 0$.

5.4 Experiments

In this section, we validate the proposed nested saturation controller on our UAV platform. The experiments are implemented on ANCLQ 2.0.

As shown in [104], the transmission delay from Vicon to PX4 is 0.025 s. To show the controller's robustness to time delay, we add more delay on purpose. The parameters chosen are listed in Table 5.1. With these parameters, we can calculate the most tolerant delay is 0.14 s. We also add an integral term to remove the steady error.

We first consider the hovering problem. The desired location of the UAV is set at $[0, 0, -1]^T$ m. The position and angle trajectories without extra delay are shown in Figure 5.2 and 5.3, where the solid red lines represent the actual trajectories, and the blue dash dot lines are the desired trajectories. Then, we set the delay to be 0.125 and 0.225 s in the Vicon system, respectively. The position trajectories are shown in 5.4 and 5.5. To make the comparison clearer, we also plot the UAV's trajectories in $p_1^n - p_2^n$ plane. In Figure 5.6, we draw a circle for each case using the maximum magnitude of the trajectory as the radius the trajectories. Trajectories when $D = 0.025$, 0.125 and 0.225 s are shown using the red solid, black dash and blue dash dot lines, respectively. The circle and triangle markers are the starting
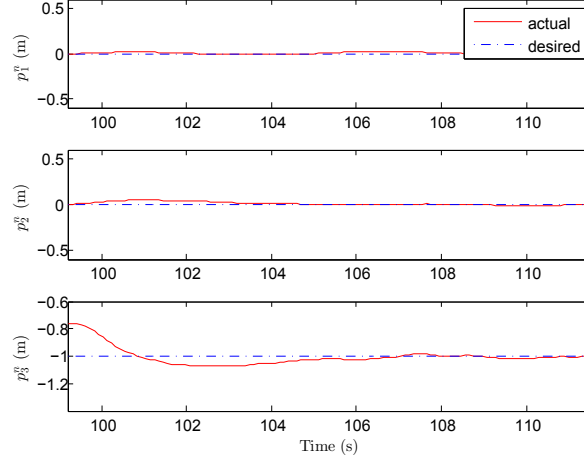
Figure 5.2: UAV position trajectories of hovering with $D = 0.025$ s.

and ending points. We can observe that as the delay goes larger, the circle goes bigger too.

We also consider the tracking problem. The reference trajectory is chosen as a line between $[0.5, 0.5, -1]^T$ and $[-0.5, -0.5, -1]^T$. The desired velocity is 0.1 m/s. Position and angle trajectories when the delay is 0.025 s are shown in Figure 5.7 and 5.8. Figure 5.9 and 5.10 show the results when the delay is 0.125 s and 0.225 s, respectively.

The quadrotor is manually control to take off and to hover at $[0, 0, -1]$ m using the ANCL Vicon position control. However, the quadrotor with this control started to oscillate when $D = 0.1$ s, as shown in Figure 5.11. The ANCL Vicon position control is switched on at $t = 72.4$ s. This means the initial state is not predictable when the delay is large. For the safety reason, we decided not to increase the value of delay in experiments.

5.5 Conclusion

This chapter investigates the robustness of the nested saturation controller of UAVs to time delay. An upper bound on time delay is obtained to guarantee the system's stability. For small delay cases, the nested saturation controller can still be applied saving the extra steps of compensating time delay. Experiments on ANCL quadrotor platform validate our theoretical results.
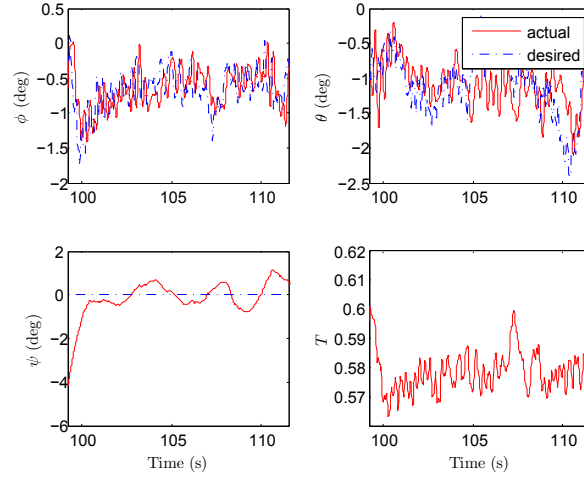
97

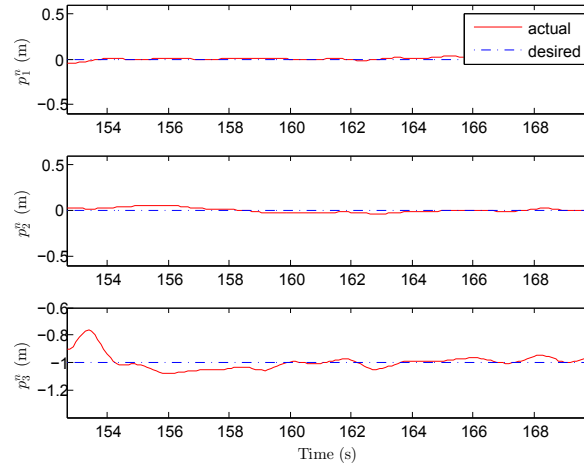Figure 5.3: UAV Euler angle trajectories of hovering with $D = 0.025$ s.

Figure 5.4: UAV position trajectories of hovering with $D = 0.125$ s.
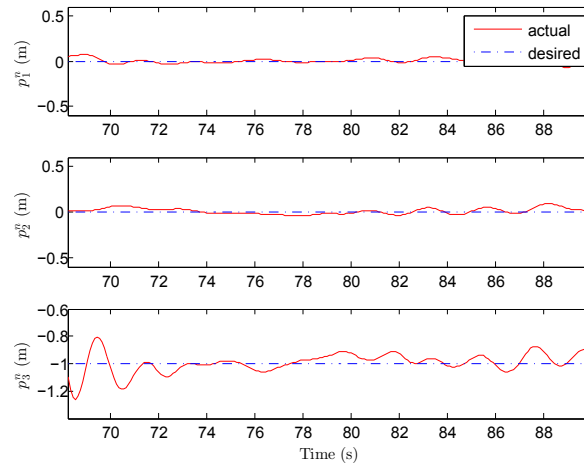

Figure 5.5: UAV position trajectories of hovering with $D = 0.225$ s.
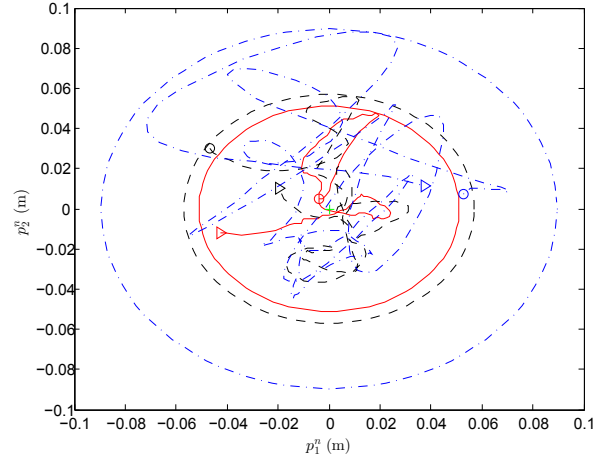
Figure 5.6: UAV position trajectories in $p_1^n - p_2^n$ plane.
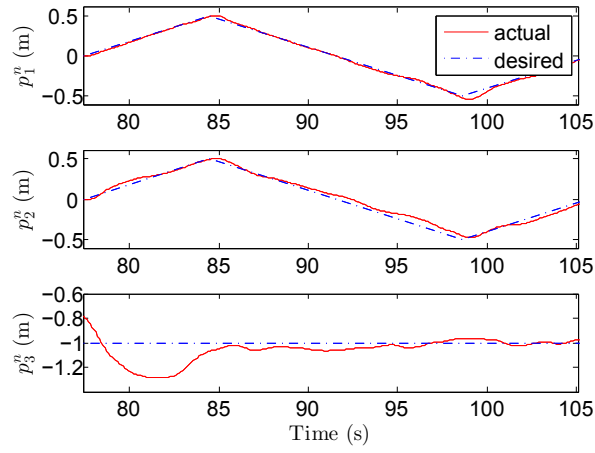

Figure 5.7: UAV position trajectories of tracking with $D = 0.025$ s.
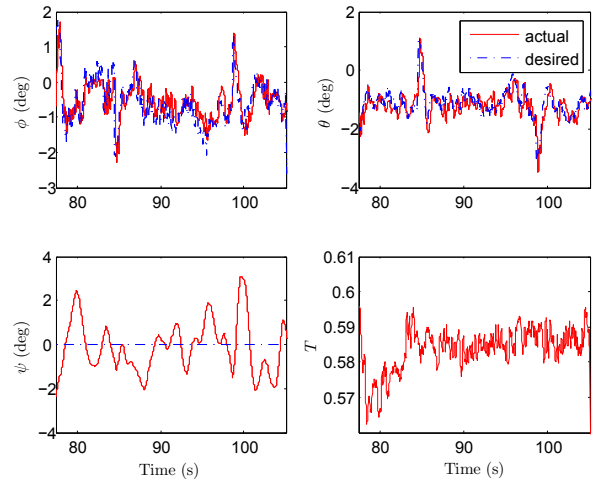

Figure 5.8: UAV Euler angle trajectories of tracking with $D = 0.025$ s.
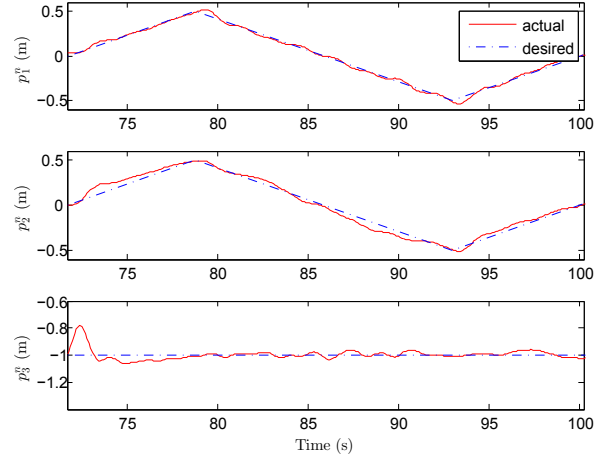
99

Figure 5.9: UAV position trajectories of tracking with $D = 0.125$ s.
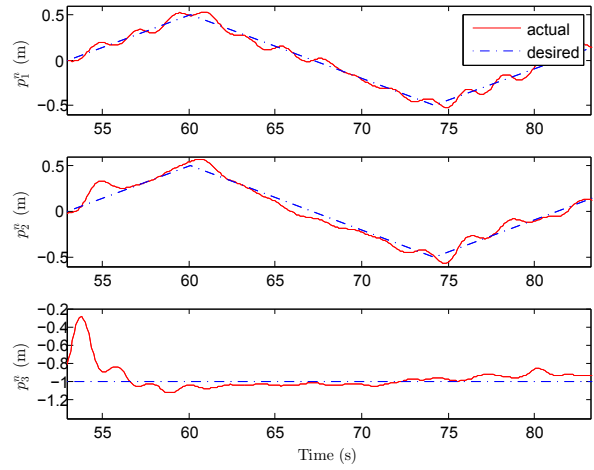

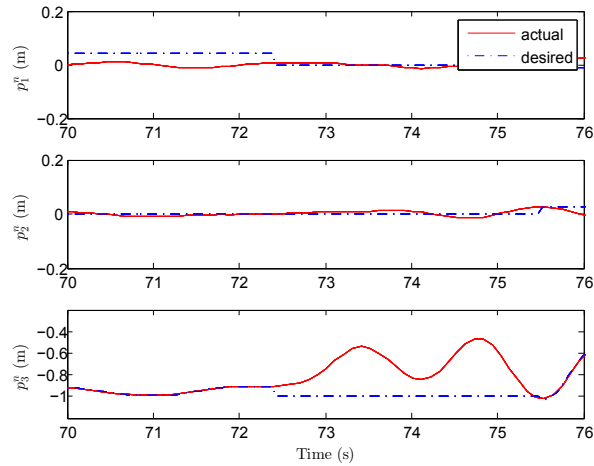Figure 5.10: UAV position trajectories of tracking with $D = 0.225$ s.

Figure 5.11: UAV position trajectories in ANCL Vicon position control mode.

Chapter 6

Conclusions and Future Work

This thesis considered the nonlinear control of quadrotor unmanned aerial vehicles (UAVs) with constraints and time delay. Chapter 2 presented the UAV dynamics and image kinematics for image-based visual servoing (IBVS). Experimental indoor quadrotor platform was also described. The onboard software is open-source, which allows for customized configuration. The platform has proven itself to be a reliable testbed for nonlinear control as it has been used in many publications.

In Chapter 3, we designed an inner-outer loop controller with state and input constraints for the motion control problem. We proposed a nested saturation control for the translational dynamics in body frame. Based on this controller, the outer loop generated a saturated thrust, and the reference roll and pitch angles, while the inner loop was designed to follow these reference angles using a traditional PID controller. We proved the global asymptotic stability of the outer loop by assuming perfect inner loop tracking, and then analyzed the effect of nonideal inner loop tracking on the closed-loop stability.

We also considered control problems with time delay, which was caused by communication latency. In Chapter 4 we proposed synchronization-based predictors for a class of systems with inaccurate model parameter and unknown delay. We modified the predictor dynamics in [58] to improve the robustness of controllers to uncertainties. A rigorous stability proof using LKFs was provided to obtain sufficient conditions for global asymptotic stability. These controllers were applied to two UAV control problems, i.e., motion control and visual servoing problems.

In Chapter 5, we analyzed the robustness of the nested saturation controller of UAVs to time delay. Based on the analysis, sufficient conditions for stability on time delay and control parameters were given. For small delay cases, the nested saturation controller can still be applied with the advantage of saving extra steps of compensating time delay.

Future work includes:

- Saturation control of visual servoing problems. In Chapter 3, we proposed a nested saturation controller for UAV motion control problem. It was stated that the controller can be extended to visual servoing problem, since their dynamics have the same structure, but the extension still needs to be investigated. Work in [105] proposes nested saturation controllers for lateral, height and yaw motion separately for UAV IBVS using a virtual camera. However, the separation is based on an approximate model. Even though uncertainties, e.g. the unknown thrust constant, are considered, there is space for performance improvements for virtual camera based IBVS. On the other hand, constrained control for visual servoing with spherical projection [31, 81] will also be considered. This can be seen as an extension of the work in Chapter 3 to the case with unknown parameters.

- State constraints. In Chapter 3, we proposed a nested saturation controller for the outer loop to generate bounded roll and pitch references. We concluded that the actual roll and pitch will stay within the given bounds by assuming the inner loop can track the reference angles perfectly. However, in practice, the inner-loop tracking error is unavoidable and might cause the actual angles to go beyond the bounds. To solve the problem, we need to design an inner-loop controller with state constraints. One example of control with state constraints can be found in [106].

- Unmodelled dynamics. Throughout this thesis, while designing controllers, we considered the simplified model for external force and torque. Blade flapping, drag force, gyroscopic and reaction torque, as described in Section 2.1, were neglected. Therefore, the robust analysis of the proposed nested saturation controller and predictor based controller with respect to the modelling uncertainties will be considered as future work. We will also take into account of these terms in the controller design process for better performance.

- Time-varying delay. In Chapter 4 and 5, we assumed the time delay was a constant. We will remove the assumption by modelling the delay as a bounded continuous time-varying function, which is more realistic and challenging. Work in [47] solves linear systems with time-varying delay using LMI method. This is categorized as emulation approach. Predictor-based control for time-varying delay is considered in [49]. Work in [107] extended the synchronization-based prediction to time-varying delay case. Based on these reference, we will develop prediction-based controller with time-varying delay for UAV control problems.

- Experimental validation. Experiments of visual servoing problems with the

predictor-based controller will be tested in the future. Moreover, the work proposed above will also be implemented.

Bibliography

[1] J. Borenstein, "The HoverBot: An electrically powered flying robot," *Unpublished White Paper*, 1992.

[2] H. Lim, J. Park, D. Lee, and H. Kim, "Build your own quadrotor: Open-source projects on unmanned aerial vehicles," *Robotics Automation Magazine, IEEE*, vol. 19, no. 3, pp. 33–45, September 2012.

[3] N. Guenard, T. Hamel, and V. Moreau, "Dynamic modeling and intuitive control strategy for an "X4-flyer"," in *proceedings of 2005 International Conference on Control and Automation*, vol. 1, Budapest, Hungary, June 2005, pp. 141–146.

[4] S. Bouabdallah, P. Murrieri, and R. Siegwart, "Design and control of an indoor micro quadrotor," in *Proceedings of IEEE International Conference on Robotics and Automation*, vol. 5, New Orleans, USA, April 2004, pp. 4393–4398.

[5] G. Hoffmann, D. Rajnarayan, S. Waslander, D. Dostal, J. Jang, and C. Tomlin, "The Stanford testbed of autonomous rotorcraft for multi agent control (STARMAC)," in *The 23rd Digital Avionics Systems Conference*, vol. 2. Salt Lake City, USA: IEEE, October 2004, pp. 12.E.4–1–10.

[6] L. Meier, P. Tanskanen, L. Heng, G. Lee, F. Fraundorfer, and M. Pollefeys, "Pixhawk: A micro aerial vehicle design for autonomous flight using onboard computer vision," *Autonomous Robots*, vol. 33, no. 1-2, pp. 21–39, 2012.

[7] J. How, B. Bethihke, A. Frank, D. Dale, and J. Vian, "Real-time indoor autonomous vehicle test environment," *IEEE Control Systems Magazine*, vol. 28, no. 2, pp. 51–64, April 2008.

[8] N. Michael, D. Mellinger, Q. Lindsey, and V. Kumar, "The GRASP multiple micro-UAV testbed," *IEEE Robotics and Automation Magazine*, vol. 17, no. 3, pp. 56–65, September 2010.

[9] S. Lupashin, M. Hehn, M. W. Mueller, A. P. Schoellig, M. Sherback, and R. D'Andrea, "A platform for aerial robotics research and demonstration: The flying machine arena," *Mechatronics*, vol. 24, no. 1, pp. 41–54, 2014.

[10] B. Godbolt, "Experimental nonlinear control of a helicopter unmanned aerial vehicle (UAV)," Ph.D. dissertation, University of Alberta, Edmonton, AB, 2013.

[11] M. Barczyk, "Nonlinear state estimation and modeling of a helicopter UAV," Ph.D. dissertation, University of Alberta, Edmonton, AB, 2012.

[12] D. R. Kastelan, "Design and implementation of a GPS-aided inertial navigation system for a helicopter UAV," Master's thesis, University of Alberta, Edmonton, AB, 2009.

[13] H. Xie and A. F. Lynch, "State transformation-based dynamic visual servoing for an unmanned aerial vehicle," *International Journal of Control*, vol. 89, no. 5, pp. 892–908, October 2016.

[14] G. Fink, H. Xie, A. F. Lynch, and M. Jagersand, "Dynamic visual servoing for a quadrotor using a virtual camera," *Unmanned Systems*, vol. 5, no. 1, pp. 1–17, 2017.

[15] N. Cao and A. F. Lynch, "Inner-Outer loop control for quadrotor UAVs with input and state constraints," *IEEE Transactions on Control System Technology*, vol. 24, no. 5, pp. 1797–1804, September 2016.

[16] T. J. Koo and S. Sastry, "Output tracking control design of a helicopter model based on approximate linearization," Tampa, FL, December 1998, pp. 3635–3640.

[17] P. Castillo, A. Dzul, and R. Lozano, "Real-time stabilization and tracking of a four-rotor mini rotorcraft," *IEEE Transactions on Control System Technology*, vol. 12, no. 4, pp. 510–516, July 2004.

[18] R. Mahony and T. Hamel, "Robust trajectory tracking for a scale model autonomous helicopter," *International Journal of Robust and Nonlinear Control*, vol. 14, no. 12, pp. 1035–1059, 2004.

[19] L. Meier, "PX4 autopilot," http://pixhawk.org/ [accessed 01 Jan 2018], Institute for Visual Computing, Swiss Federal Institute of Technology Zurich, 2018. [Online]. Available: http://pixhawk.org/

[20] N. Mohan, T. M. Undeland, and W. Robbins, *Power Electronics Converters, Applications and Design*, 3rd ed. Hoboken, New Jersey, USA: John Wiley and Sons, 2003.

[21] F. Kendoul, I. Fantoni, and R. Lozano, "Asymptotic stability of hierarchical inner-outer loop-based flight controllers," in *Procedings of the 17th IFAC World Congress*, Seoul, Korea, July 2008, pp. 1741–1746.

[22] A. Roberts and A. Tayebi, "Adaptive position tracking of VTOL UAVs," *IEEE Transactions on Robotics*, vol. 27, no. 1, pp. 129–142, February 2011.

[23] L. Wang and H. Jia, "The trajectory tracking problem of quadrotor UAV: Global stability analysis and control design based on the cascade theory," *Asian Journal Control*, vol. 16, no. 2, pp. 574–588, March 2014.

[24] A. Roza and M. Maggiore, "A class of position controllers for underactuated VTOL vehicles," *IEEE Transactions on Automatic Control*, vol. 59, no. 9, pp. 2580–2585, September 2014.

[25] B. Godbolt, N. I. Vitzilaios, and A. F. Lynch, "Experimental validation of a helicopter autopilot design using model-based PID control," *Journal of Intelligent Robotic Systems*, vol. 70, no. 1, pp. 385–399, April 2013.

[26] B. Godbolt and A. F. Lynch, "Model-based helicopter UAV control: Experimental results," *Journal of Intelligent Robotic Systems*, vol. 73, no. 1-4, pp. 19–31, January 2014.

[27] F. Chaumette and S. Hutchinson, "Visual servo control Part I: Basic approaches," *IEEE Robotics and Automation Magazine*, vol. 13, no. 4, pp. 82–90, December 2006.

[28] O. Shakernia, Y. Ma, T. J. Koo, and S. Sastry, "Landing an unmanned air vehicle: Vision based motion estimation and nonlinear control," *Asian Journal Control*, vol. 1, no. 3, pp. 128–145, September 1999.

[29] F. Mazenc, R. Mahony, and R. Lozano, "Forwarding control of scale model autonomous helicopter: a Lyapunov control design," in *Proceedings of the 42nd IEEE Conference on Decision and Control*, Maui, HI, December 2003, pp. 3960–3965.

[30] M. Burger and M. Guay, "A backstepping approach to multivariable robust constraint satisfaction with application to a VTOL helicopter," in *Proceedings of the 48h IEEE Conference on Decision and Control held jointly with 28th Chinese Control Conference*, Shanghai, China, December 2009, pp. 5239–5244.

[31] T. Hamel and R. Mahony, "Visual servoing of an under-actuated dynamic rigid-body system: an image-based approach," *IEEE Transactions on Robotics and Automation*, vol. 18, no. 2, pp. 187–198, August 2002.

[32] G. Fink, H. Xie, A. F. Lynch, and M. Jagersand, "Nonlinear dynamic visual servoing of a quadrotor," *Journal of Unmanned Vehicle Systems*, vol. 3, no. 1, pp. 1–21, 2015.

[33] A. R. Teel, "Global stabilization and restricted tracking for multiple integrators with bounded controls," *Systems and Control Letters*, vol. 18, no. 3, pp. 165–171, March 1992.

[34] N. Marchand, "Further results on global stabilization for multiple integrators with bounded controls," in *42nd IEEE International Conference on Decision and Control*, Maui, USA, December 2003, pp. 4440–4444.

[35] B. Zhou, G.-R. Duan, and Z.-Y. Li, "On improving transient performance in global control of multiple integrators system by bounded feedback," *Systems and Control Letters*, vol. 57, no. 10, pp. 867–875, October 2008.

[36] B. Zhou and G.-R. Duan, "Global stabilisation of multiple integrators via saturated controls," *IET Control Theory and Applications*, vol. 1, no. 6, pp. 1586–1593, November 2007.

[37] S. Gayaka, L. Lu, and B. Yao, "Global stabilization of a chain of integrators with input saturation and disturbances: A new approach," *Automatica*, vol. 48, no. 7, pp. 1389–1396, July 2012.

[38] H. J. Sussman, E. D. Sontag, and Y. Yang, "A general result on the stabilization of linear systems using bounded controls," *IEEE Transactions on Automatic Control*, vol. 39, pp. 2411–2425, December 1994.

[39] N. Marchand and A. Hably, "Global stabilization of multiple integrators with bounded controls," *Automatica*, vol. 41, no. 12, pp. 2147–2152, December 2005.

[40] L. Marconi and R. Naldi, "Robust nonlinear control of a miniature helicopter for aerobatic maneuvers," in *Proceedings of the 32th European Rotorcraft Forum*, Maasctricht, Netherlands, September 2006, pp. 1005–1020.

[41] J. Hu and H. Zhang, "Immersion and invariance based command-filtered adaptive backstepping control of VTOL vehicles," *Automatica*, vol. 49, no. 7, pp. 2160–2167, April 2013.

[42] N. Metni and T. Hamel, "A UAV for bridge inspection: Visual servoing control law with orientation limits," *Automation in Construction*, vol. 17, no. 1, pp. 3–10, November 2007.

[43] D. Q. Mayne, J. B. Rawlings, C. V. Rao, and P. O. M. Scokaert, "Constrained model predictive control: Stability and optimality," *Automatica*, vol. 36, no. 6, pp. 789–814, June 2000.

[44] H. Kim and D. H. Shim, "A flight control system for aerial robots: algorithms and experiments," *Control Engineering Practice*, vol. 11, no. 12, pp. 1389–1400, December 2003.

[45] K. Gu and S.-I. Niculescu, "Survey on Recent Results in the Stability and Control of Time-Delay Systems," *Journal of Dynamic Systems, Measurement, and Control*, vol. 125, no. 2, p. 158, June 2003.

[46] J.-P. Richard, "Time-delay systems: an overview of some recent advances and open problems," *Automatica*, vol. 39, no. 10, pp. 1667–1694, October 2003.

[47] E. Fridman, *Introduction to Time-Delay Systems*. Basel: Springer, 2014.

[48] K. Gu, J. Chen, and V. L. Kharitonov, *Stability of Time-Delay Systems*. Springer Science & Business Media, 2003.

[49] M. Krstic, *Delay Compensation for Nonlinear, Adaptive, and PDE Systems*. Boston: Birkhäuser, 2009.

[50] L. Karafyllis, M. Malisoff, F. Mazenc, and P. Pepe, *Recent Results on Nonlinear Delay Control Systems*. Springer, 2016.

[51] Z. Artstein, "Linear systems with delayed controls: A reduction," *IEEE Transactions on Automatic Control*, vol. 27, no. 4, pp. 869–879, August 1982.

[52] Q.-C. Zhong, *Robust Control of Time-delay Systems*. London: Springer-Verlag, 2006.

[53] D. Bresch-Pietri and M. Krstic, "Adaptive trajectory tracking despite unknown input delay and plant parameters," *Automatica*, vol. 45, no. 9, pp. 2074–2081, September 2009.

[54] D. Bresch-Pietri, J. Chauvin, and N. Petit, "Adaptive control scheme for uncertain time-delay systems," *Automatica*, vol. 48, no. 8, pp. 1536–1552, August 2012.

[55] V. Léchappé, E. Moulay, F. Plestan, A. Glumineau, and A. Chriette, "New predictive scheme for the control of LTI systems with input delay and unknown disturbances," *Automatica*, vol. 52, pp. 179–184, February 2015.

[56] N. Bekiaris-Liberis and M. Krstic, "Predictor-Feedback stabilization of multi-input nonlinear systems," *IEEE Transactions on Automatic Control*, vol. 62, no. 2, pp. 516–531, February 2017.

[57] F. Mazenc, S.-I. Niculescu, and M. Krstic, "Lyapunov-Krasovskii functionals and application to input delay compensation for linear time-invariant systems," *Automatica*, vol. 48, no. 7, pp. 1317–1323, July 2012.

[58] T. Oguchi and H. Nijmeijer, "Control of nonlinear systems with time-delay using state predictor based on synchronization," in *Proceedings of the Euromech Nonlinear Dynamics Conference (ENOC)*, Eindhoven, Netherlands, August 2005, pp. 1150–1156.

[59] A. Alvarez-aguirre, N. V. D. Wouw, T. Oguchi, and H. Nijmeijer, "Predictor-Based remote tracking control of a mobile robot," *IEEE Transactions on Control System Technology*, vol. 22, no. 6, pp. 2087–2102, April 2014.

[60] F. Mazenc, S. Mondie, and S.-I. Niculescu, "Global asymptotic stabilization for chains of integrators with a delay in the input," *IEEE Transactions on Automatic Control*, vol. 48, no. 1, pp. 57–63, January 2003.

[61] N. Cao and A. F. Lynch, "Inner-outer loop control with constraints for rotary-wing UAVs," in *Proceedings of the 2015 International Conference on Unmanned Aircraft Systems*, Denver, CO, June 2015, pp. 294–302.

[62] ——, "Predictor-based controllers for UAVs with input delay," in *2017 IEEE International Conference on Advanced Intelligent Mechatronics (AIM)*, Munich, Germany, July 2017, pp. 803–808.

[63] ——, "Predictor-based control design for UAVs: robust stability analysis and experiments," *submitted to International Journal of Control*, pp. 1–28, July 2018.

[64] ——, "Time-delay robustness analysis of a nested saturation control for UAVs," *submitted to IEEE Transactions on Aerospace and Electronic Systems*, July 2018.

[65] C. Powers, D. Mellinger, and V. Kumar, *Quadrotor Kinematics and Dynamics*. Dordrecht: Springer Netherlands, 2015, pp. 307–328.

[66] P. Castillo, R. Lozano, and A. Dzul, *Modelling and control of mini flying machines.* New York City, USA: Springer-Verlag, 2005.

[67] M. Bangura, "Aerodynamics and control of quadrotors," Ph.D. dissertation, Australian National University, Canberra, Australia, 2017.

[68] P. E. I. Pounds, "Design, construction and control of a large quadrotor micro air vehicle," Ph.D. dissertation, Australian National University, Canberra, Australia, 2007.

[69] P. Pounds, R. Mahony, and P. Corke, "Modelling and control of a large quadrotor robot," *Control Engineering Practice*, vol. 18, no. 7, pp. 691–699, July 2010.

[70] J. G. Leishman, *Principles of Helicopter Aerodynamics*, 2nd ed. Cambridge, UK: Cambridge University Press, 2016.

[71] R. Leishman, J. Macdonald, R. Beard, and T. McLain, "Quadrotors and accelerometers: State estimation with an improved dynamic model," *IEEE Control Systems Magazine*, vol. 34, no. 1, pp. 28–41, February 2014.

[72] R. M. Murray, Z. Li, and S. S. Sastry, *A Mathematical Introduction to Robotic Manipulation.* Boca Raton, FL: CRC Press, 1994.

[73] F. Kendoul, "Survey of advances in guidance, navigation, and control of unmanned rotorcraft systems," *Journal of Field Robotics*, vol. 29, no. 2, pp. 315–378, March 2012.

[74] G. Antonelli, E. Cataldi, F. Arrichiello, P. R. Giordano, S. Chiaverini, and A. Franchi, "Adaptive trajectory tracking for quadrotor MAVs in presence of parameter uncertainties and external disturbances," *IEEE Transactions on Control System Technology*, vol. 26, no. 1, pp. 248–254, January 2018.

[75] C. Nicol, C. Macnab, and A. Ramirez-Serrano, "Robust adaptive control of a quadrotor helicopter," *Mechatronics*, vol. 21, no. 6, pp. 927–938, September 2011.

[76] I. A. Raptis, K. P. Valavanis, and W. A. Moreno, "A novel nonlinear backstepping controller design for helicopters using the rotation matrix," *IEEE Transactions on Control System Technology*, vol. 19, no. 2, pp. 465–473, March 2011.

[77] J. H. Gillula, H. Huang, M. P. Vitus, and C. J. Tomlin, "Design and analysis of hybrid systems, with applications to robotic aerial vehicles," in *Robotics Research*, ser. Springer Tracts in Advanced Robotics, C. Pradalier, R. Siegwart, and G. Hirzinger, Eds. Berlin, Heidelberg: Springer Berlin Heidelberg, 2011, vol. 70, pp. 139–149.

[78] M. Ang and V. Tourassis, "Singularities of Euler and roll-pitch-yaw representations," *IEEE Transactions on Aerospace and Electronic Systems*, vol. AES-23, no. 3, pp. 317–324, May 1987.

[79] A. D. Roberts, "Attitude estimation and control of VTOL UAVs," Ph.D. dissertation, University of Western Ontario, London, ON, 2011.

[80] A. Isidori, L. Marconi, and A. Serrani, "Robust nonlinear motion control of a helicopter," *IEEE Transactions on Automatic Control*, vol. 48, no. 3, pp. 413–426, March 2003.

[81] T. Hamel and R. Mahony, "Image based visual servo control for a class of aerial robotic systems," *Automatica*, vol. 43, no. 11, pp. 1975–1983, November 2007.

[82] R. Ozawa and F. Chaumette, "Dynamic visual servoing with image moments for an unmanned aerial vehicle using a virtual spring approach," *Advanced Robotics*, vol. 27, no. 9, pp. 683–696, 2013.

[83] D. Lee, T. Ryan, and H. Kim, "Autonomous landing of a VTOL UAV on a moving platform using image-based visual servoing," in *Proceedings of the 2012 IEEE International Conference on Robotics and Automation*, Saint Paul, MN, 2012, pp. 971–976.

[84] D. Lee, H. Lim, H. Kim, Y. Kim, and K. Seong, "Adaptive image-based visual servoing for an underactuated quadrotor system," *Journal of Guidance, Control, and Dynamics*, vol. 35, no. 4, pp. 1335–1353, July 2012.

[85] H. Jabbari Asl and J. Yoon, "Robust image-based control of the quadrotor unmanned aerial vehicle," *Nonlinear Dynamics*, vol. 85, no. 3, pp. 2035–2048, August 2016.

[86] H. Xie, G. Fink, A. F. Lynch, and M. Jagersand, "Adaptive dynamic visual servoing of a UAV," *IEEE Transactions on Aerospace and Electronic Systems*, vol. 52, no. 5, pp. 2529–2538, October 2016.

[87] F. Bullo and R. M. Murray, "Tracking for fully actuated mechanical systems: a geometric framework," *Automatica*, vol. 35, pp. 17–34, 1999.

[88] A. Tayebi and S. McGilvray, "Attitude stabilization of a VTOL quadrotor aircraft," *IEEE Transactions on Control System Technology*, vol. 14, no. 3, pp. 562–571, May 2006.

[89] H. Jabbari Asl, G. Oriolo, and H. Bolandi, "An adaptive scheme for image-based visual servoing of an underactuated UAV," *International Journal of Robotics and Automation*, vol. 29, no. 1, pp. 92–104, 2014.

[90] H. J. Sussmann and Y. Yang, "On the stabilizability of multiple integrators by means of bounded feedback controls," in *Proceedings of the 30th IEEE Conference on Decision and Control*, vol. 1, Brighton, UK, December 1991, pp. 70–72.

[91] F. Mazenc, S. Mondie, and R. Francisco, "Global asymptotic stabilization of feedforward systems with delay in the input," *IEEE Transactions on Automatic Control*, vol. 49, no. 5, pp. 844–850, May 2004.

[92] J. Azinheira and A. Moutinho, "Hover control of an UAV with backstepping design including input saturations," *IEEE Transactions on Control System Technology*, vol. 16, no. 3, pp. 517–526, May 2008.

[93] D. Mellinger, N. Michael, and V. Kumar, "Trajectory generation and control for precise aggressive maneuvers with quadrotors," in *Experimental Robotics*, ser. Springer Tracts in Advanced Robotics, O. Khatib, V. Kumar, and G. Sukhatme, Eds. Berlin, Heidelberg: Springer Berlin Heidelberg, 2014, vol. 79, pp. 361–373.

[94] K. Alexis, G. Nikolakopoulos, and A. Tzes, "Constrained-control of a quadrotor helicopter for trajectory tracking under wind-gust disturbances," in *15th IEEE Mediterranean Electrotechnical Conference*, Valletta, Malta, April 2010, pp. 1411–1416.

[95] G. Fink, "Computer Vision-Based Motion Control and State Estimation for Unmanned Aerial Vehicles (UAVs)," Ph.D. dissertation, University of Alberta, Edmonton, AB, 2018.

[96] R. Sanz, P. Garcia, Q.-C. Zhong, and P. Albertos, "Predictor-based control of a class of time-delay systems and its application to quadrotors," *IEEE Transactions on Industrial Electronics*, vol. 64, no. 1, pp. 459–469, January 2017.

[97] H. Jabbari Asl, S. H. Mahdioun, and J. Yoon, "Vision-based control of an underactuated flying robot with input delay," *Transactions of the Institute of Measurement and Control*, vol. 1, pp. 1–10, October 2016.

[98] H. Liu, W. Zhao, Z. Zuo, and Y. Zhong, "Robust control for quadrotors with multiple time-varying uncertainties and delays," *IEEE Transactions on Industrial Electronics*, vol. 64, no. 2, pp. 1303–1312, February 2017.

[99] N. Yeganefar, P. Pepe, and M. Dambrine, "Input-to-State Stability and exponential stability for time-delay systems: further results," in *2007 46th IEEE Conference on Decision and Control*, New Orleans, USA, December 2007, pp. 2059–2064.

[100] J. K. Hale and S. Verduyn Lunel, *Introduction to Functional Differential Equations*. New York: Springer-Verlag, 1993.

[101] T. Oguchi and H. Nijmeijer, "Prediction of chaotic behavior," *IEEE Transactions on Circuits and Systems I: Regular Papers*, vol. 52, no. 11, pp. 2464–2472, November 2005.

[102] R. Sepulchre, M. Janković, and P. V. Kokotović, *Constructive Nonlinear Control*. London; New York: Springer, 1997.

[103] N. O. Sedova, "The global asymptotic stability and stabilization in nonlinear cascade systems with delay," *Russian Mathematics*, vol. 52, no. 11, pp. 60–69, 2008.

[104] A. Othmane, "Online compensation of time delayed measurements in mobile robotics," B.Sc. thesis, Saarland University, Sarbruecken, 2015.

[105] H. Xie and A. F. Lynch, "Input saturated visual servoing for unmanned aerial vehicles," *IEEE/ASME Transactions on Mechatronics*, vol. 22, no. 2, pp. 952–960, April 2017.

[106] K. P. Tee, S. S. Ge, and E. H. Tay, "Barrier Lyapunov functions for the control of output-constrained nonlinear systems," *Automatica*, vol. 45, pp. 918–927, April 2009.

[107] T. Oguchi, T. Yamamoto, and H. Nijmeijer, *Synchronization of bidirectionally coupled nonlinear systems with time-varying delay.* Berlin, Heidelberg: Springer Berlin Heidelberg, 2009, pp. 391–401.